University of Kansas
College of Liberal Arts and Sciences
Department of Physics and Astronomy

Diffractive Dijet Photoproduction in pPb collisions at $\sqrt{S_{NN}}$ = 8.16 TeV

Filling in the gaps

Doctoral Dissertation

COLE LINDSEY

in fulfillment of the requirements for the degree of Doctor of Philosophy

Doctoral advisor: Christophe Royon
Foundation Distinguished Professor

Approved by the committee composed of the members

(Signature)	*(Signature)*	*(Signature)*
.....	.....	.....
Christophe Royon Foundation Distinguished Professor	Kyoungchul Kong Professor	Stephen Sanders Professor
(Signature)	*(Signature)*	
.....	.....	
Christopher Fischer Professor	Mathew Johnson Professor	

Date Defended: January 7th, 2022

University of Kansas
College of Liberal Arts and Sciences
Department of Physics and Astronomy

The Dissertation Committee for Cole Leon Lindsey certifies that this is the approved version of the following dissertation :

Diffractive Dijet Photoproduction in pPb collisions at $\sqrt{S_{NN}}$ = 8.16 TeV

Dr. Christophe Royon, Chairperson

January 27th, 2022

Date Approved

Abstract

With the advent of the Large Hadron Collider(LHC), experimental high energy physics gained access to brand new kinematical regions. Experiments performed here allow us to explore the realms heretofore unknown and unseen by our forebears through the use of the higher energies and the collisions of different types of particles. Collisions between protons and lead ions were conducted at center of mass energies of 8.16 TeV representing an extremely large increase in center of mass energy from previous experiments. In this dissertation, a gap shall be filled in the understanding related to the photoproduction of diffractive dijets by utilizing data collected at the LHC in 2016. Through the use of this enormous energy, we will see for the first time such events at these energies and a measurement of Z_{IP} and x_γ shall be conducted. Such events allow us to have a remarkable probe into the very nature of one of Quantum Chromodyanamic's most mysterious objects, the pomeron.

Acknowledgements

The first person I would like to thank is Christophe Royon, without whom it would have been impossible to even do this thesis in so many different ways. His support and always encouraging words throughout my years at KU has helped me develop the skills and confidence to know that it would all work out in the end.

Another person I wish to thank with all my heart is Jennifer Delgado and all the people I taught with throughout the years. Teaching was a solace during the times in grad school when things got tough, so her guidance in showing me the joys of teaching and also being there to help me when things got crazy were most appreciated.

Next, I would like to thank my fellow graduate students – Cristian, Justin, Tommaso, Zach, Federico, and Florian. As the years went by, our office became more and more cramped, but only with love, and I wouldn't trade a single person. I count myself beyond lucky to have done my thesis alongside you all.

I would also like to thank all my CMS colleagues who time and time again offered their expertise when I was stuck beating my head against a wall and making it all seem so simple.

Additionally, I would like to thank my committee members. I was so happy to be able to maintain the same committee for the same reason I asked you all to be on it in the first place. My academic career hasn't always been a smooth one, and each and every one of you represented a high point for me. After all of this is done, the classes I had with you all and the kind words you had for me along the way will be the memories I cherish most.

Finally, I would like to thank my friends. Our group chats were instrumental in keeping me sane during work and most importantly during the writing of this. I owe you all for entertaining me when I thought it was all going to fall apart. I love you guys and thank you so much for being there when I needed you all most.

Kansas, January 2022

Cole Lindsey

Contents

List of Figures

List of Tables

Chapter 1: Introduction

Contents

Before going too in depth with the subject matter of this dissertation, it is important to have a common understanding and basis of physics upon which to build. Therefore, the goal of this chapter is to provide an introduction into several elements which will be useful in understanding the later chapters of this dissertation. We begin with the foundations of the Standard Model and how it came to be in Section 1.1. Afterwards, a brief discussion presenting Quantum Electrodynamics (QED) in Section 1.2. Then, paralleling the previous section, we shall discuss Quantum Chromodynamics (QCD) in Section 1.3.

1.1 The Standard Model

The Standard Model (SM) of particle physics is one of the most successful theories ever created. Built upon the backs of thousands of physicists since the 1930s, the SM outlines the most basic levels of matter around us and helps us explain what is happening at these smallest of scales. Similarly to the periodic table of elements, the SM describes how once thought fundamental particles such as protons and neutrons actually have a unifying substructure between them. Additionally, it describes 3 of the 4 fundamental forces that govern all interactions in our universe [1]. These forces are the strong force, electromagnetism, and the weak force; gravity is not contained within the SM. Despite its

flaws, however, it remains the most successful theory crafted and in this section we will discuss the journey taken by thousands of scientists to reach this level of understanding.

1.1.1 Introduction to Particle Physics

To talk of particle physics and its foundations is to talk about scattering experiments. A scattering experiment, at its roots, is fundamentally one of the most basic experiments that humans do. Each and every one of us conducted a scattering experiment (of sorts) when we were children while playing outside. A child, presented with a rock, postulates that if they take that rock and smash it into a rock, then *something* will happen. Now that same child, perhaps given a budget on the order of $9 Billion, might come up with an experiment not too dissimilar to the very ones talked about in this dissertation. The stage might seem different and the players foreign, but at the core of these experiments lies the simple fact that we're simply smashing things together just to see what happens and expand our understanding of the world a little further. In order to talk of particle physics in the modern era, it's important to understand the steps along the way that got us there. Therefore, we will begin with a brief historical journey through particle physics.

The path through particle physics, as one might expect, lies almost solely through the discovery of different particles. As can be seen beautifully represented in Figure 1.1, each milestone on the path to our current understanding lies deeply entwined with the particles themselves. While we won't be discussing the discovery of each, every individual particle discovered comprises a thread weaving together to our current grand tapestry of knowledge.

For the beginning of our particle journey, we will start with the very first fundamental particle discovered, the electron. The knowledge of its fundamental nature is only in retrospect, but even at the time, it marked a boundary in our understanding of the world around us. For nearly 2000 years, from the origins of the word atom itself meaning indivisible, the thinking was that atoms were some homogeneous particle. It was not that long ago that Mendeleev created the first periodic table, as seen in Figure 1.2, by noticing certain patterns in the different types of matter around him. The simple answer

Figure 1.1: An art piece titled "Nuts and Bolts" by Lindsay Olson representing the particles as they were discovered on the path to completing the SM [2].

isn't always right, but when such patterns were emerging it was understandable to think that the world around us was composed of different types of atoms, but that they existed independently of each other. The discovery of the electron was the first step and peeking behind the curtain of atomic makeup and seeing that there was yet another secret to be discovered.

The path to discovering the electron lies adjacent to the creation and refinement of the cathode ray tube. In 1858, Julius Plücker discovered how to create a cathode ray tube, as seen in Figure 1.3, which then led to a rush to understand what exactly these cathode rays were. Various experiments were performed in the following years demonstrating that these rays were charged, composed of many individual particles, and that these

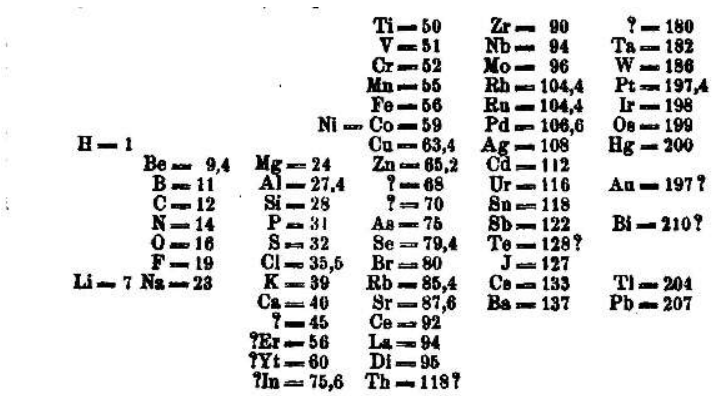

Figure 1.2: The precursor to the periodic table which was created by Mendeleev in 1869. It was the first when the periodic nature of atomic structure was formalized in such groupings.

particles had mass. The culmination of these discoveries lies with J.J. Thomson and his observation of the effect of both magnetic and electric fields on the cathode rays thus firmly measuring them as individual negative particles and thus giving them the name electron. One of the most surprising aspects of the discovery of the electron was how small that mass actually was. Electrons were found to be less than $\frac{1}{1000}$ the size of the next largest known particle at the time, which was the hydrogen atom. Thus, from the smallest of beginnings, began the shakeup in our understanding of the nature of the world around us.

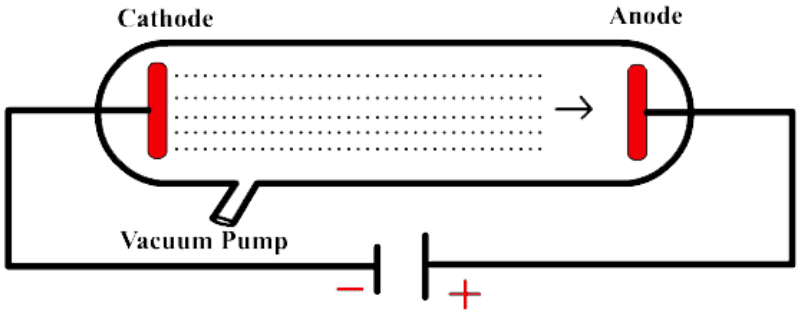

Figure 1.3: Simple diagram of a cathode ray tube. By having opposite charged plates separated by a vacuum, a cathode ray can be created, which we know now is as a stream of electrons.

At the beginning of the 1900s, when particle physics was in its infancy, Ernest Rutherford was one of the pioneers attempting to learn about the new and fascinating world of the small elements that make up everyday life. To study this, he had one of the first scattering experiments where he took a source of alpha particles and aimed it at a thin

gold foil. The idea was that the alpha particles would hit the gold atoms making up the foil and then scatter off. By looking at these scattering angles, Rutherford would be able to study the properties of these atoms. To his amazement, when the alpha particle struck the gold foil, very rarely it would be deflected back towards his alpha particle source, rather than only being slightly deflected [3]. Rutherford famously said, "It was almost as incredible as if you fired a 15 inch shell at a piece of tissue paper and it came back and hit you." This was a remarkable discovery that we can now see was the discovery of the proton, or more precisely that the nucleus is a highly concentrated area of positive charge. The positively charged alpha particles would sometimes strike the nucleus and, due to both possessing a positive charge, they would be repelled from one another with surprising force. Rutherford's scattering experiment is one of the first in a long series of scattering experiments that continue on to this day. Strategies that were implemented in the early 1900s have been refined, but at its core, we're often doing the same experiment over 100 years later.

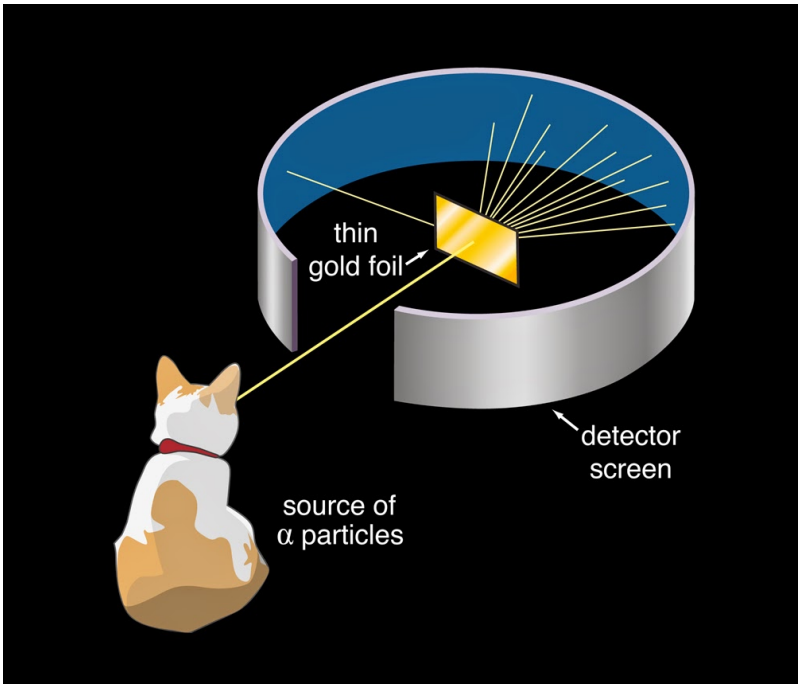

Figure 1.4: Stylization of the Rutherford scattering experiment. Alpha particles were emitted towards a gold foil and then the scattering angles were measured. Because the particles sometimes bounced backwards, Rutherford inferred that there was an extremely small and positively charged object in the center of atoms which we now know is the nucleus.

As these very strategies were being refined as the years went by, an extremely interesting problem started to emerge. Mendeleev had shown the periodic nature of atoms, but through discoveries by Thomson, Rutherford, and others it was shown that the periodic nature could be explained by some underlying structure that made matter more simple at its most base level. It was thought then that everything was composed of protons, neutrons, and electrons which lent a certain elegance in the simplicity. All matter could be created from different combinations of these 3 "elementary" particles. However, those pesky scientists weren't satisfied, and, as experiments such as Rutherford's were refined and repeated at higher energies, suddenly there was an influx of new particles being discovered. These particles seemed similar to protons, neutrons, and electrons, but bafflingly they were not composed of any known particles and seemed elementary themselves. Suddenly the elegance gained by having 3 elementary particles was completely shattered as dozens of seemingly "elementary" particles were emerging. It seemed as if we were back in the exact same situation we had with Mendeleev's periodic table of elements. This problem became known as the "particle zoo" as this rapid influx of new elementary particles left physicists feeling like tired zookeepers exploring a brand new continent and trying to write down all the new life they saw. Wolfgang Pauli said upon the matter, "Had I foreseen this, I would have gone into botany" illustrating the sheer disconnect from expectations and how taken aback the average physicist was at this development. Thankfully, this zoo wasn't here to stay. The pattern that was ran into before with atoms would indeed hold true and as methods advanced and higher energies were reached, a unifying factor would again be found and elegance regained.

Before progressing more into the history of particle collisions, it it worth noting at this point in history the sheer magnitudes of difference in experimental setups from Rutherford's experiments. Rutherford was operating in a simple lab with a target and the barest of detectors. In the intervening years, it became readily apparent that to see things that had previously been unseen, we would need to go to even higher energies. Thus began the age of particle accelerators and getting into setups that looks remarkably similar to our current experiments when compared to the leap between Rutherford and

this point in time. As mentioned previously, the ideas behind particle physics experiment are, fittingly, very elementary in nature. One simply smashes things together and sees what comes out. The difference, however, lies is on how hard one is able to smash your various objects together. So while Rutherford was colliding alpha particles with gold foil with energies on the order of 5 megaelectronvolts (MeV), at this point in history collisions were occurring at center of mass energies over 1000 times larger. These energies were not accessible without many advances and very specific experimental setups.

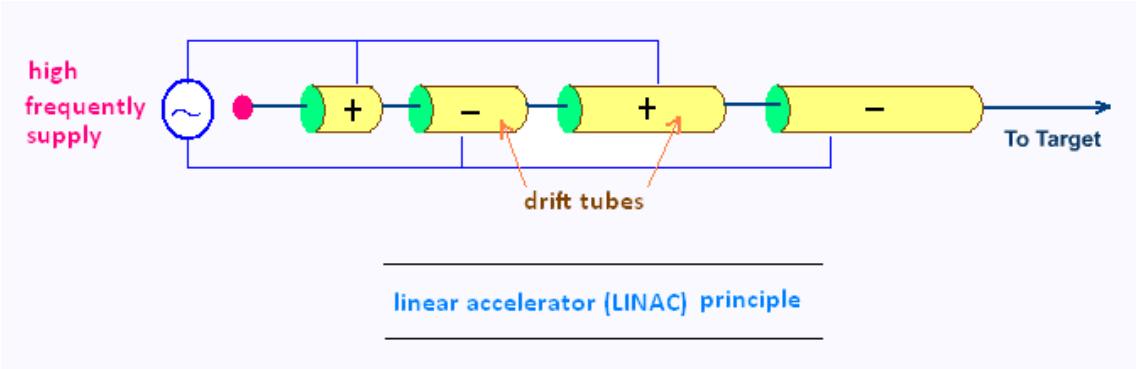

Figure 1.5: Diagram outlining the principles of a linear accelerator. The oscillations being sent to the drift tubes ensure that as the particle bunches hit each tube, they will always gain energy on their way to the final collision.

A particle accelerator, as the discerning reader might figure out, is exactly as it sounds. They are machines whose primarily goal is to accelerate particles to as high an energy as possible and, most importantly, cause those particles to collide. They can collide with other particles that are also being accelerated, or can be set to strike a stationary target. The latter was the more common class of collisions that occurred in early high energy physics, such as with Rutherford's scattering experiment off the gold foil target. Nowadays, many particle accelerators opt for accelerating two beams of particles rather than going for the single beam because this allows a higher center of mass energy, and therefore new kinds of physics, to be seen.

The two primary types of particle accelerators are linear accelerators and circular accelerators. As the names imply, the key difference lies in the type of tubes in which the particles are accelerated. Linear accelerators, as can be seen in Figure 1.5, are particle accelerators in which the particles move in a straight line being being accelerated via the use of oscillating electrical fields. These oscillations allow the particle bunches to

be accelerated continually from the electrical field as they progress down the beam pipe. Typically, linear accelerators operate in fixed target experiments, similar to Rutherford's original scattering. Whatever particle you are accelerating moves down the beam pipe, continually increasing in energy, until it hits the target at the end and then the results of the collision are measured.

The other type of particle accelerator, and the type used in collection of the data for this dissertation, are circular accelerators. One of the main benefits circular accelerators have over linear accelerators is the ability to not have a finite distance to increase energy over. The circular design of the beam pipe means that the particles can circulate again and again, each time gaining more energy, until the specified energy is achieved. The method for increasing the energy of the particle bunches is very similar to linear accelerator design, but the main difference lies in the methods of collisions themselves. While linear accelerators typically use a fixed target type experiment, circular accelerators often opt for a collision between two beams of particles. By accelerating the beams to extremely high energies in opposite directions before colliding, much higher center of mass energies can be reached than in normal fixed target experiments.

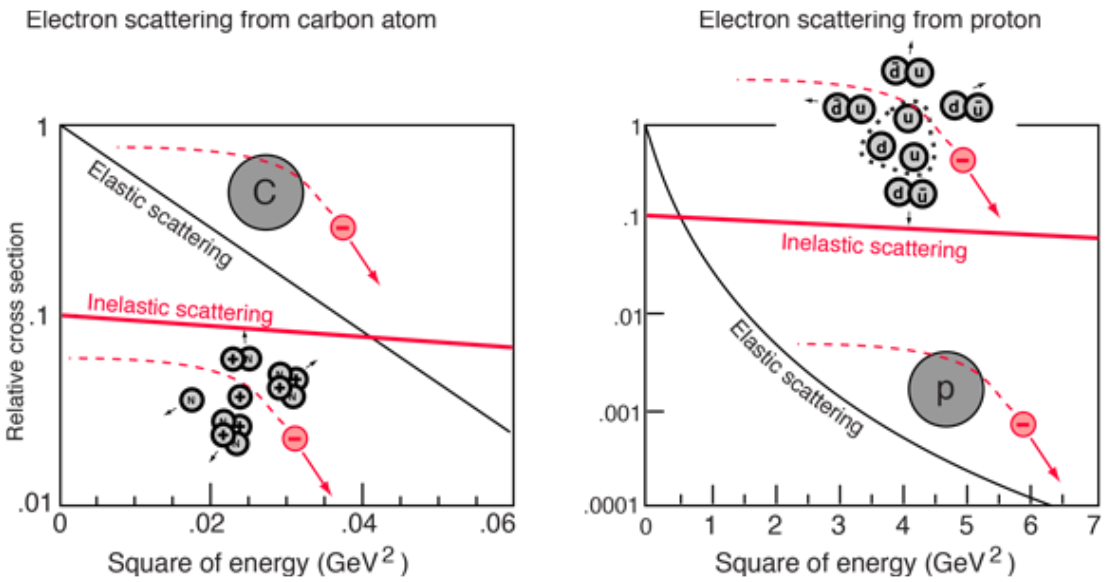

Figure 1.6: Principles of Deep Inelastic Scattering. As energy increased in scattering experiments with electrons and carbon atoms, evidence of substructure of the carbon atom (protons and neutrons) was revealed. By similar principles, and much higher energies, scattering the electron off the proton can additionally reveal substructure of the proton.

Now that we understand the level of technological advancement from Rutherford, we can begin to see how physicists were able to probe the very smallest constituents of matter to solve the dilemma of the particle zoo. As mentioned before, however, the principles of Rutherford's original experiment would again be instrumental. In order to determine if there were substructures to protons, a scattering experiment was proposed at the Stanford Linear Accelerator Center (SLAC) in 1968. The experiment would be scattering electrons off of protons with the hope being that, similarly to Rutherford, the patterns by which the electrons scattered would be indicative of some sort of structure to the proton. As the clever reader might have already guessed, there was indeed evidence for substructure to the proton found at SLAC as can be seen in Figure 1.6. The combination of the elastic cross section decreasing and the inelastic scattering cross section remaining constant was indicative that the electron was scattering off of something within the proton rather than the proton itself. This marks the discover of quarks, which are the pieces that comprise particles such as protons that the electron was scattering off of. Indeed, SLAC was able to go even further and show that a proton was made up of 3 of these quarks, with 2 becoming known as "up" quarks and 1 "down" quark. This much needed evidence for the Quark Parton Model allowed for the taming of the Particle Zoo. By being able to show that there were indeed further structure to particles such as protons, we were able to see that this so-called zoo of elementary particles could instead be pruned down to a handful of elementary quarks.

However, there were still fairly glaring problems to our understanding of what was happening at this most small scale. The most perplexing mysteries of this most small world were that partons, which is our catch-all name for objects within hadrons, appeared to be free during a collision, there was some as of yet unknown parton carrying 50% of the momentum, and finally the most basic mystery of why partons were only found in bound states. The answers to these questions, and indeed many more, can be found thoroughly discussed in Section 1.3. In that section we discuss QCD as the successor to the Quark Parton Model. Through QCD, the interplay between this new classification of elementary particles could be described and would begin paving the way to our current

understanding, which is known as the Standard Model. To fully understand the scope of the SM, we will now discuss the various particles that comprise it to fully see the scope of how monumental a discovery it truly was.

1.1.2 Particles of the Standard Model

As we saw in the previous section, in the 1960s there were seemingly endless amounts of new particles similar to protons and neutrons being discovered. This so called "particle zoo" gave way to the discovery of more fundamental particles and, blessedly, a simplification to classifications of particles which are the hallmarks of a sound scientific theory. Thus, the creation of the Standard Model of Particle Physics gave answer to the particle zoo by classifying 12 fundamental particles and 5 force carriers. At its inception, many of the particles in the SM had yet to be discovered. Thus, further credence was given to the theory over and over as particles it theorized to exist were being discovered. The last among these being the W and Z bosons in 1983, the top quark in 1995, the tau neutrino in 2000, and finally the Higgs Boson in 2012.

The particles of the SM are further broken down into several different categories. The first being the division between fermions, which are the building blocks of all the matter around us, and bosons, which mediate the forces of the SM [4]. These groups and others we will discuss can be seen in Figure 1.7. Fermions are all particles that obey the exclusion principle. What this means is that no two fermions are able to be described by the same quantum numbers. This encompasses the 12 particles from the SM, but additionally all particles that are composed of them. Meaning all matter around us are fermions as well because it is composed of fermions like quarks and leptons.

The other major classification, bosons, are particles which are responsible for mediating interactions such as electromagnetism. For each of the forces described by the SM, there is an associated vector boson. For electromagnetism, the strong force, and the weak force the associated boson is the photon, gluon, and W and Z bosons, respectively. The forces in action can be seen in Figure 1.9. Additionally, there is a singular scalar boson which is the Higgs boson. The Higgs boson is responsible for mediating the Higgs mech-

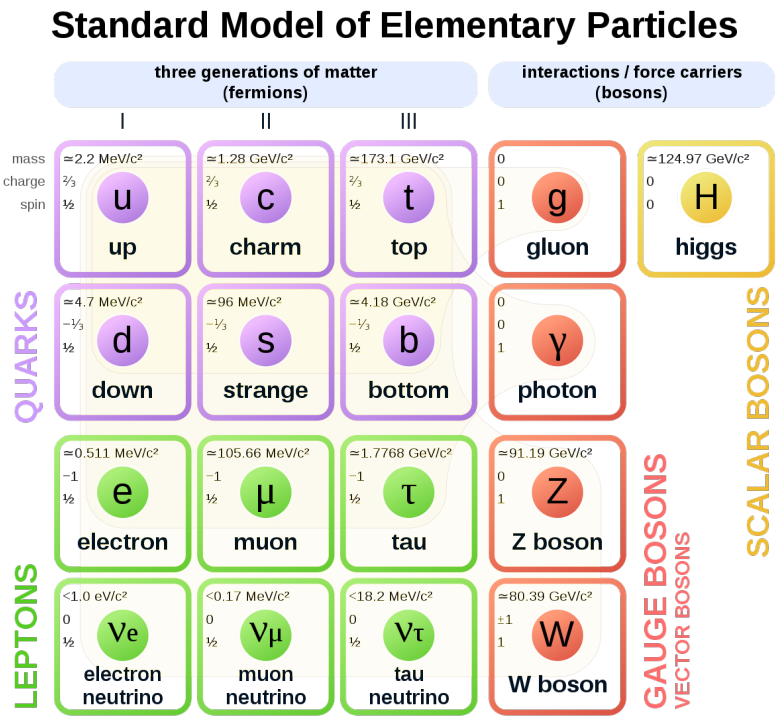

Figure 1.7: Representation of the different particles composing the SM. Particles are separated by classification of groups of quarks, leptons, gauge bosons, and scalar bosons. The numbers in each of the squares represent a given particle's mass, charge, and spin.

anism which is responsible for explaining masses of certain particles [5]. As fermions are unable to have the same quantum numbers, conversely bosons are able to be described by the same quantum numbers.

Within the fermions, there are two further classifications. The first group, quarks, are fermions which must exist in a bound state. They maintain a property known as color confinement, as discussed in Section 1.3, which means that they cannot exist in a color charged state [6]. Quarks have been observed to bind into 2 and 3 quark arrangements, as long as they maintain a neutral color charge as can be see in Figure 1.8. When quarks are bound in a doublet, that is known as a meson (such as a pion). The triplet bound state of quarks is known as a baryon, and this corresponds to the more familiar pieces of matter such as protons and neutrons. There are 6 quarks with flavors up, down, strange, charm, top, and bottom. The names are a quirk of their discovery and do not reflect any particular property of the quarks.

The other classification of fermions are the leptons [7]. As might be expected, a

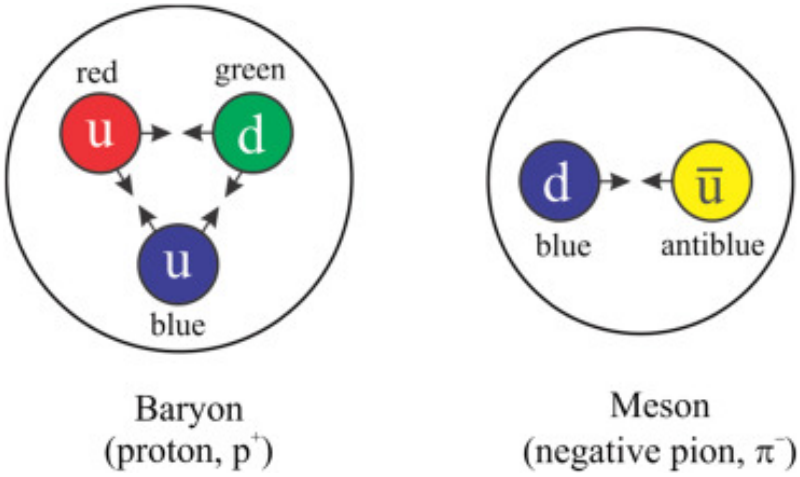

Figure 1.8: Representation of two of the bound states for quarks. On the left hand side is the baryon which is composed of 3 quarks in a color neutral configuration. On the right hand side is a meson which is 2 quarks bound in a color neutral configuration.

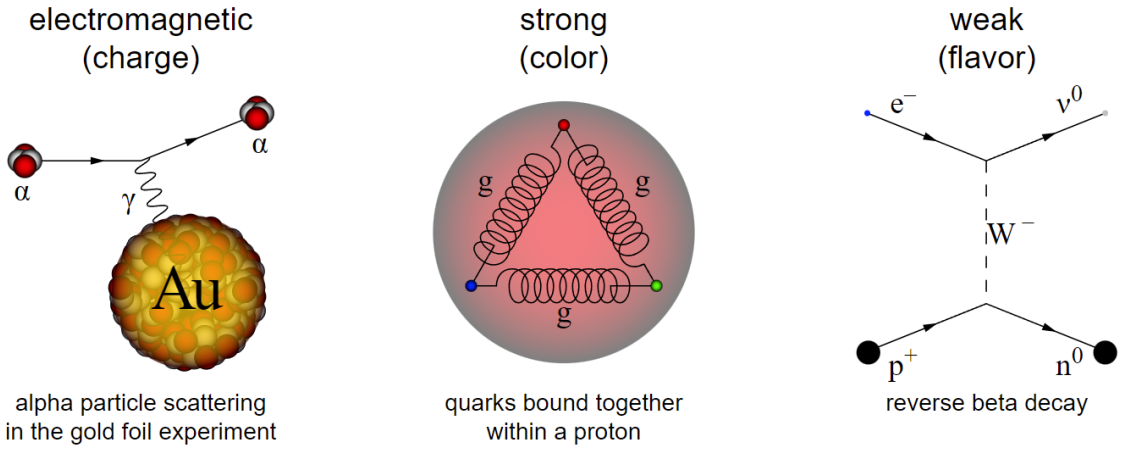

Figure 1.9: The three fundamental forces that are contained within the SM. From left to right, one can see electromagnetism, the strong force, and the weak force being mediated by the photon, gluon, and W boson, respectively.

lepton's distinction from quarks is that they can exist independently of a bound state. This aligns with our familiar understanding of the electron and explains why leptons, generally speaking, were discovered before quarks. Since quarks can exist only in a bound state, there wasn't the ability to directly isolate and observe them until technology had advanced sufficiently. Similarly to quarks, leptons exist in 3 generations of pairs. In the case of leptons, however, there is more of a distinction between each pair. In each generation there is an electron-like particle (such as the electron, muon, and tau). Then paired with each of these particles is its associated neutrino. Neutrinos are weakly interacting particles that have very small masses. This leads to neutrinos being able to

pass through almost all matter with no interaction.

All of the elementary particles have an intrinsic spin angular momentum. Spin is a quantized quantity and the values it can take depend on the type of elementary particle. Fermions, such as quarks and electrons, have half integer spin numbers ($\frac{1}{2}$, $1\frac{1}{2}$, etc.) while bosons have integer spin numbers (0, 1, 2, etc.). Elementary fermions all have a spin of $\frac{1}{2}$, but when combined together into bound states it is possible for them to have greater spin values. Baryons, which are combinations of three quarks, and mesons, which are combinations of 2 quarks, are both examples of this. Interestingly in the meson's case, when two fermions are bound together their spin will end up being either 0 or 1, which means mesons are themselves bosons.

1.2 Quantum Electrodynamics

Quantum Electrodynamics (QED) is the theory that outlines interactions of charged particles and electromagnetic waves. It takes regular quantum theory and then applies to fields of force, such as an electromagnetic field. QED was the first theory that was able to get full agreement between special relativity and quantum mechanics. The high accuracy of predictions made from QED leads it to be on of the most successful theories ever devised. The principle behind QED theory was that the interaction between charged particles, such as electrons, are able to be modeled via emission and absorption of photons. These particles that mediated the interactions are called virtual, meaning they are not directly observable. They merely act as a mediator for the force, and so can be thought of more as a theoretical tool than an actual physical photon that could be observed, as can be seen in Figure 1.10.

The foundations of QED were laid down in 1926 when Dirac formulated equations describing the motion and spin of electrons that, for the first time, was able to create a union between special relativity and quantum theory. From there, in the 1940s others such as Feynman, Schwinger, and Tomonaga were able to further refine the theory into a more robust and widely applicable form. QED describes, at its core, three separate processes and from the myriad ways to combine them we are able to construct any and

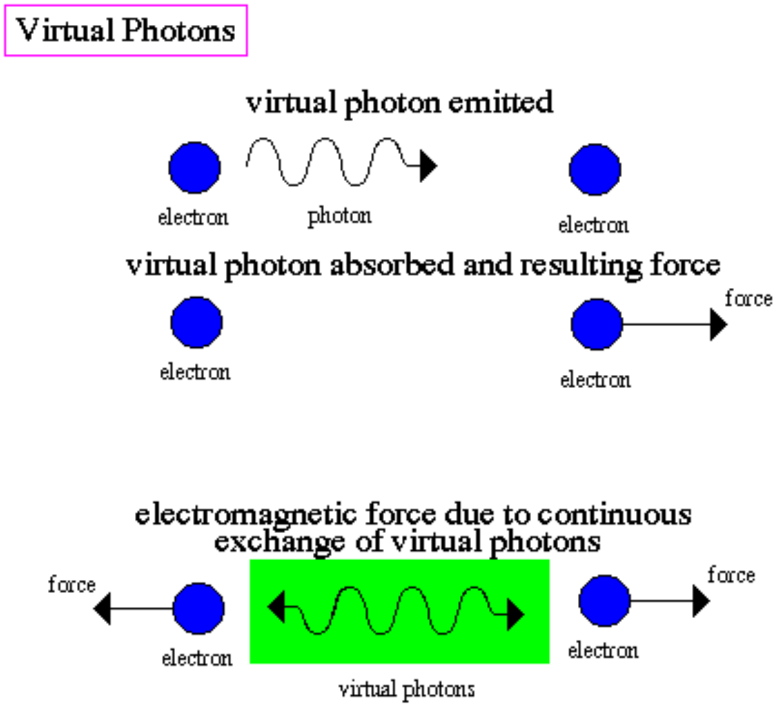

Figure 1.10: A representation of what is meant by "virtual" particles. These particles merely act as a mediator for the force and therefore can be thought of more as a theoretical tool than an actual physical particle.

all electromagnetic interactions. These actions are a photon going from one place and time to another place and time, an electron going from one place and time to another place and time, and finally an electron emitting or absorbing a photon at a certain place and time. Through the use of a clever shorthand, Feynman was able to construct a pictorial way to represent these interactions which became known as Feynman diagrams. An example of the three types of actions that are described in QED can be seen in Figure 1.11. In this interaction, we can see all three types of actions in play. The electron moves through space and time, emits a photon that moves through space and time, and finally is absorbed by another electron. This is only a single interaction, and in reality when using Feynman diagrams one must have all the different possible interactions and sum them up to complete the calculations.

In order to get a full understanding on QED, one must delve past the pictorial representations and get into the math behind it. As QED is a quantum field theory, it has an associated Lagrangian which can then be utilized to predict the outcomes of particle interactions. The QED Lagrangian is

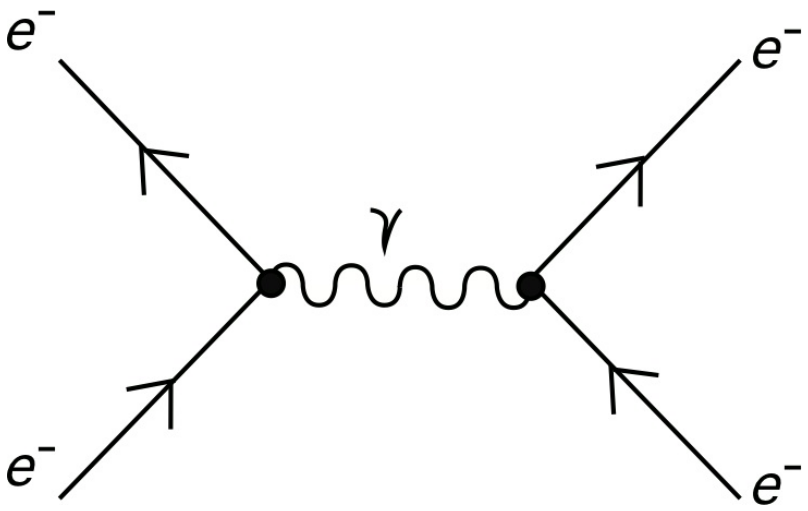

Figure 1.11: A Feynman diagram representing the interaction of two electrons.

$$\mathcal{L}_{QED} = \bar{\psi}(i\gamma^{\mu}D_{\mu} - m)\psi - \frac{1}{4}F_{\mu\nu}F^{\mu\nu}, \tag{1.1}$$

where ψ is a spin-$\frac{1}{2}$ field (such as an electron field), γ^{mu} are the Dirac matrices, D_{μ} is the gauge covariant derivative, and $F_{\mu\nu}$ is the electromagnetic field tensor.

To give a demonstration of how the Lagrangian is utilized, we will show how the equations of motion can be obtained from the QED Lagrangian [8]. First off, we begin with the full definition of the gauge covariant derivative,

$$D_{\mu} = \partial_{\mu} + ieA_{\mu} + ieB_{\mu}, \tag{1.2}$$

noting that A_{μ} and B_{μ} are the covariant four-potential of the electromagnetic field of the spin-$\frac{1}{2}$ particle and an external electromagnetic field, respectively. Taking this and then substituting it into our original Lagrangian yields

$$\mathcal{L}_{QED} = i\bar{\psi}\gamma^{\mu}\partial_{mu}\psi - e\bar{\psi}\gamma^{\mu}(A_{\mu} + B_{\mu})\psi - m\bar{\psi}\psi - \frac{1}{4}F_{\mu\nu}F^{\mu\nu}. \tag{1.3}$$

Given this expanded form of the QED Lagrangian, we can then utilize the Euler-

Lagrange equation for ψ,

$$\partial_\mu \left(\frac{\partial \mathcal{L}}{\partial(\partial_\mu \psi)} \right) - \frac{\partial \mathcal{L}}{\partial \psi} = 0 \tag{1.4}$$

Inserting the QED Lagrangian in and calculating the relevant derivatives will give us

$$\partial_\mu \left(\frac{\partial \mathcal{L}}{\partial(\partial_\mu \psi)} \right) = \partial_\mu (i\bar{\psi}\gamma^\mu) \tag{1.5}$$

and

$$\frac{\partial \mathcal{L}}{\partial \psi} = -e\bar{\psi}\gamma^\mu (A_\mu + B_\mu) - m\bar{\psi}. \tag{1.6}$$

Substituting these back into Equation 1.4 will give us

$$i\partial_\mu \bar{\psi}\gamma^\mu + e\bar{\psi}\gamma^\mu (A_\mu + B_\mu) + m\bar{\psi} = 0 \tag{1.7}$$

with Hermitian conjugate,

$$i\gamma^\mu \partial_\mu \psi - e\gamma^\mu (A_\mu + B_\mu)\psi - m\psi = 0. \tag{1.8}$$

Taking the middle term over to the right will give us

$$i\gamma^\mu \partial_\mu \psi - m\psi = e\gamma^\mu (A_\mu + B_\mu)\psi, \tag{1.9}$$

which should look very familiar to us. The left hand side is the Dirac equation, which describes the motion of spin-$\frac{1}{2}$ particles. Additionally, on the right hand side we have the

interaction with the electromagnetic field and so together we have an equation of motion describing a spin-$\frac{1}{2}$ particle in an external electromagnetic field.

A similar operation can be performed for the A field, starting again with the Euler-Lagrange equation:

$$\partial_\nu \left(\frac{\partial \mathcal{L}}{\partial(\partial_\nu A_\nu)} \right) - \frac{\partial \mathcal{L}}{\partial A_\nu} = 0. \tag{1.10}$$

From there, we can then calculate these derivatives to be

$$\partial_\nu \left(\frac{\partial \mathcal{L}}{\partial(\partial_\nu A_\nu)} \right) = \partial_\nu(\partial^\mu A^\nu - \partial^\nu A^\mu) \tag{1.11}$$

and

$$\frac{\partial \mathcal{L}}{\partial A_\nu} = -e\bar{\psi}\gamma^\mu\psi. \tag{1.12}$$

Taking these derivatives and plugging them back into Equation 1.10 will simplify down to

$$\partial_\nu F^{\nu\mu} = e\bar{\psi}\gamma^\mu\psi. \tag{1.13}$$

Using the Lorenz gauge condition,

$$\partial_\mu A^\mu = 0, \tag{1.14}$$

we can then reduce the equation even further down to

$$\Box A^{\mu} = e\bar{\psi}\gamma^{\mu}\psi, \tag{1.15}$$

where $\Box$ is the D'Alembert operator. This equation is a wave equation of the four-potential, which we can then see is the QED equivalent of the classical Maxwell equation in the Lorenz gauge.

1.3 Intro to Quantum Chromodynamics

Quantum Chromodynamics (QCD) is the theoretical framework outlining strong interactions [9]. As previously discussed, it was created from the desperate need of physicists everywhere when the particle zoo arose and left the world confused at the increasingly large number of seemingly elementary particles. This began in the 1950s with the discovery of several hadrons and culminated when some of the last big questions plaguing QCD were addressed in the 1970s, as will be discussed below.

Strong interactions are interactions between particles that have a color charge which are quarks, antiquarks, and gluons. Quarks are spin-$\frac{1}{2}$ particles that carry an electric charge of $\frac{2}{3}$ or $-\frac{1}{3}$. There are six types of quarks which are known as the different "flavors" of quarks. These flavors are up, down, strange, charm, top, and bottom. The strong force doesn't make any distinction between the force between the quarks, but each of these quarks has a different mass which breaks the flavor symmetry. Gluons are the other classification of particle in QCD and they are different from quarks, which carry color charge, and antiquarks, which carry anticolor charge, in the sense that gluons carry both a color charge and an anticolor charge. While this might seem to indicate that there are 9 types of gluons (3 color charges and 3 anticolor charges), but that is actually not the case. We cannot have a gluon that is in a red-antired, blue-antiblue, or green-antigreen configuration and the fact that this color singlet state cannot exist means that there are 8 distinct states of gluons rather than the assumed 9. Quarks, antiquarks, and gluons can form together into bound states that we discussed in Section 1.1.2. Another word for

quarks and gluons that will be used throughout this thesis is parton, which arose from a model describing composite particles such as protons.

The strong force between two colored partons can be approximated with the expression

$$V(r) = \frac{fc\hbar a_s}{r} + F(r), \tag{1.16}$$

where a_s is the strong nuclear constant, f is an additional color factor that is dependent upon the specific flavor and color state, and F(r) is an additional term. This F(r) term is somewhat unique and atypical to our normal everyday understanding of forces because it appears to increase without limit [10]. In other words, as the two color charged particles get further from each other, the force between them increases. The specific form of F(r) is currently ambiguously defined for a reason. Its exact form isn't currently known and F(r) $\approx r^2$, F(r) $\approx r$, and F(r) $\approx ln(r)$ all are able to explain the data that we currently have. With future experiments, it may be possible to distinguish between the forms of F(r), but for the purpose of this thesis the most important takeaway is that the strong force increases with distance between particles.

Another interesting fact about the strong coupling constant for QCD is that its name is actually a bit of a misdirection. The coupling "constant" is not a constant at all. A better name for it is the running coupling constant because it changes based upon several factors [11]. The full equation for the running coupling constant is

$$a_s = \frac{12\pi}{(11n_c - 2n_f)ln(Q^2/\Lambda^2)}, \tag{1.17}$$

where n_c is the number of color-anticolor pairs (which we know is 3), n_f is the number of flavor-antiflavor pairs, Q is the momentum transferred, and Λ is the characteristic energy scale of QCD. The term n_f isn't as easy to quantify in an exact manner, however. This is because the number of flavor-antiflavor pairs will also depend upon the energy. For example, if Q is greater than the rest mass energy of the strange quark, but below

that of the charm, then n_f will be equal to 3. This $11n_c - 2n_f$ term arises because of an opposing vacuum polarization effect between quarks and gluons. Interestingly, the vacuum polarization effect is different for quarks and gluons. For quarks, the the magnitude increases at smaller distances, while for gluons the magnitude decreases. However, since the maximum value for n_f is 6, this means the gluon polarization effect will dominate the quark polarization effect which leads to the overall decreasing of the coupling constant at higher energies. The running coupling constant will be discussed further down below in the section about asymptotic freedom.

An important fact to note is that the realm of the strong force lies in the extremely small, and so many of our preconceived notions simply do not hold up when attempting to make generalizations. One must be aware of some of the quirks, or else you'll be led on a fruitless chase like so many physicists in the early days of QCD. Two of these quirks are color confinement and asymptotic freedom, both of which exemplify the strangeness of QCD. We will discuss each of these in turn because a level of familiarity with the stranger aspects of QCD will be helpful down the road when discussing other aspects of this thesis.

While there are similarities that can be drawn between QED and QCD, one of the most notable differences is how charge works. As discussed above, in QED we have only positive and negative charges. QCD, on the other hand, has 3 separate sets of charges: red and antired, blue and antiblue, and green and antigreen. These are what are known as color charges in QCD and can be seen in Fig 1.12. Despite the name, the concept of color charge has absolutely nothing to do with color in the visual sense, and is indeed more of a useful tool in the discussion of QCD than a helpful analogy.

One of the most interesting concepts and quirks of QCD is related to color charge and that is the property of color confinement [12]. Generally stated, color confinement refers to the idea that any particle that carries a color charge cannot exist in an isolated and independent manner. Thus, we finally have the explanation for why it took so long for quarks to be discovered. Similarly to how one can knock electrons from an atom and observe the electron, one might think a similar experiment might reveal the existence of quarks inside protons. Unfortunately for physicists everywhere, however, this was not

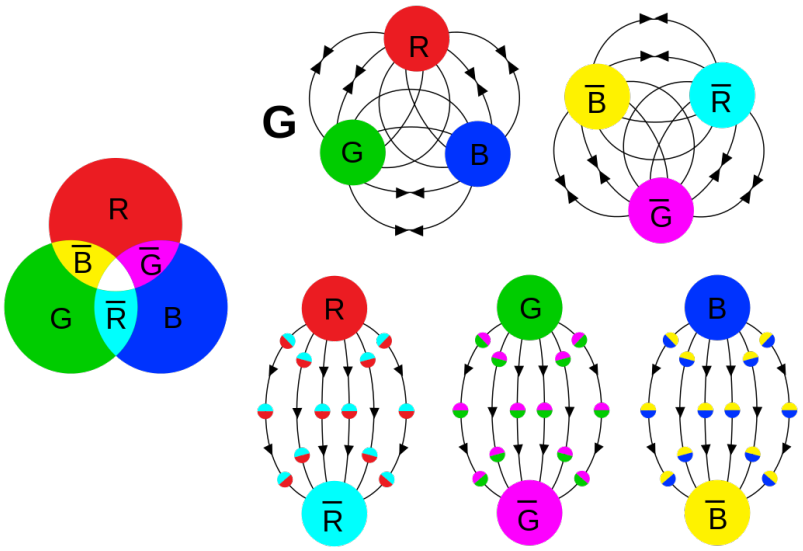

Figure 1.12: An illustration outlining the role that color charge plays in QCD. On the left hand side we can see the 3 color charges with their associated anti color. While on the the right hand side we have depictions of how particles such as baryons and mesons are able to achieve the colorless configuration.

the case. Because of color confinement, if one were to attempt to knock out a quark from a proton, a process similar to the one shown in Fig. 1.14 would occur. Since the strong force increases with distance, it becomes prohibitively more energy expensive to continue moving the quarks away from each other. There will be a critical junction when the energy needed to move the quarks apart is actually more than the energy needed to create a brand new quark-antiquark pair out of the vacuum. With the creation of this new pair in place, the original particle will instead be 2 (possibly different) particles in the final state. Therefore this is what was happening early on in scattering experiments when energies sufficient to begin probing quarks were reached. After a quark was knocked out of some target particle, it would create brand new particles from the vacuum rather than leaving the quark in an isolated spot. It was only after careful monitoring of these outgoing new particles that evidence for quarks was able to be inferred.

The next strange behavior unique to the strong force is that of asymptotic freedom [13]. In broad terms, asymptotic freedom refers to the fact that the strength of strong interactions is inversely proportional to energy and distance. That is, at high interaction energies or small distances, the forces between two color charged objects will decrease. This decreasing in the magnitude of the strong force at sufficiently high energies allows

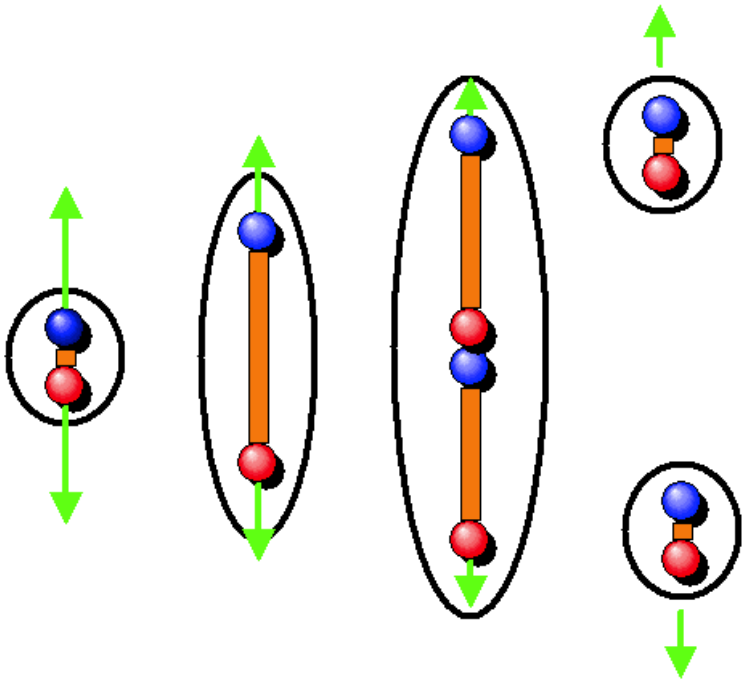

Figure 1.13: A representation of color confinement in action. In this example meson, as the distance between the quarks increases, the force between them increases as well. If this continues, then it will become energetically favorable to create another quark-antiquark pair to keep the original quarks from ever being in an unbound state.

for perturbative calculations to occur [14]. Asymptotic freedom was discovered in 1973 independently by two different groups of physicists and was instrumental in fixing quantum field theory. Before its discovery, there existed a Landau pole, which describes the smallest distance at which a given theory provides physically real results. Below the Landau pole, QCD would predict infinitely strong interactions which clearly was nonphysical and presented a large problem. Thankfully, asymptotic freedom was able to resolve that issue and reign in the problems that had previously been preventing QCD from being widely accepted.

In summary, Quantum Chromodynamics outlines interactions between particles that carry a color charge such as quarks, antiquarks, and gluons. This strong interaction is mediated by the gluon which helps bind together these particles into the more familiar states of matter that we see in our everyday life.

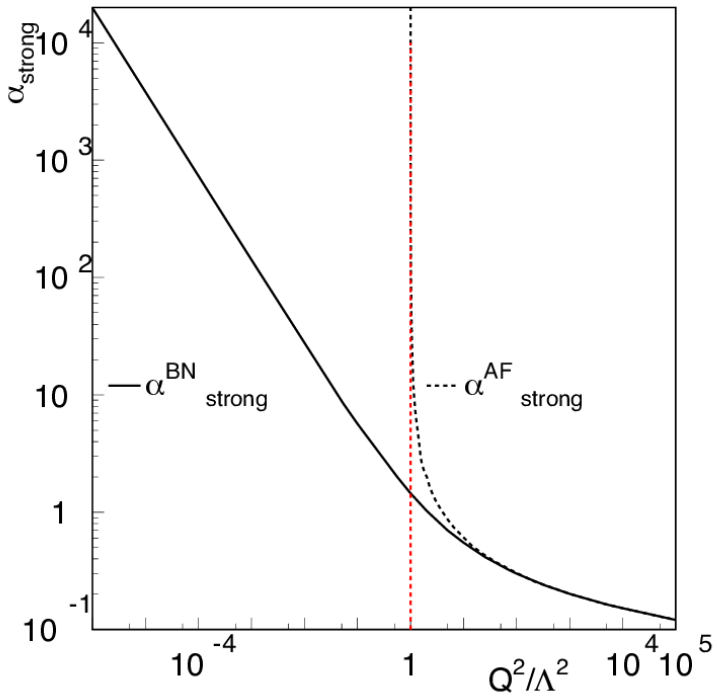

Figure 1.14: A graph outlining asymptotic freedom. As one can see, when the energy scale increases the coupling constant of the strong force will correspondingly decrease until we cross a threshold where perturbative calculations are valid and we say that the particles are asymptotically free.

1.4 Introduction to the Pomeron

Now that we have provided a background in both particle physics and the math used when discussing it, we can now move on to introducing the subject matter for this dissertation. In short, we wish to study the pomeron. The logical question to ask at this point is, "What is the pomeron," because, as the thorough reader has noticed, this is the first time we've mentioned it. The reason for this intentional omission is that it isn't as simple an object as something like the proton. In this section, we shall introduce the necessary background to this most mysterious of objects.

To begin with, we shall have a brief introduction into Regge theory. In the earlier sections of this chapter, we presented the Standard Model as well as Quantum Chromodynamics, but before they came into being, we had Regge theory. Regge theory was developed in 1959 by Tullio Regge. The basic premise of Regge theory can be explained

in terms of our earlier discussion of QED. In Figure 1.11, we explained how two electrons can interact through an exchange of a photon. Regge theory takes this principle and applies it to particles that interact through the strong force. However, in this case there isn't simply a single particle that mediates the interactions. In Regge theory we have families of particles that mediate these interactions and are all very similar, with only differences in spin between them. These families of particles mediating interactions can be represented through what we call a Regge trajectory, as can be seen in Figure 1.15.

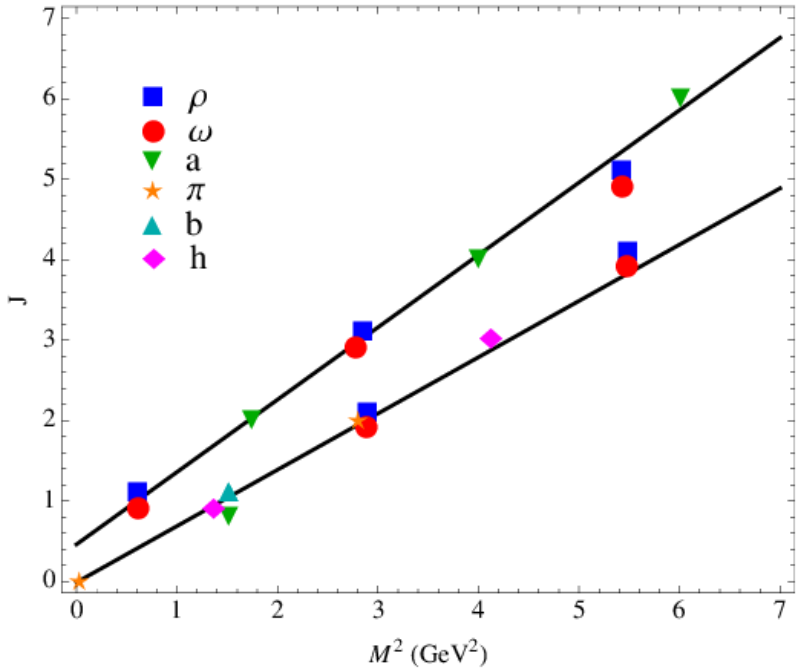

Figure 1.15: Example Regge trajectories. Each of the points on the line represent a particle within the Regge trajectory. M is the mass of these particles and J is the spin. The straight line connecting these particles is a Regge trajectory. Plot extracted from [15]

A Regge trajectory can typically be represented in the form

$$a_R(t) = a_R(0) + a_R^{'}(0)t, \tag{1.18}$$

where $a_R(0)$ is the y-intercept of the Regge trajectory and $a_R^{'}(0)$ is its slope. However, some of the predictions from Regge theory would prove troubling. When talking about the total cross section, or the summation of probabilities for all potential interactions, there were some predictions that fell flat. Regge theory predicted that the total cross section's energy

dependence would be determined by the value of the Regge trajectory at the y intercept. Or, in more exact terms:

$$\sigma_T \approx s^{a_R(0)-1}, \tag{1.19}$$

where σ_T is the total cross section, s is the collision energy squared, and $a_R(0)$ is as defined above. As all the values of $a_R(0)$ found thus far were less than 1, this meant that the total cross section was predicted to decrease with increasing energies. However, that was not the case and it was actually found that the total cross section flattened out, but then begun to increase at higher energies. The solution to this behavior was that there must be another Regge trajectory that is exchanged, but this time it would have $a_R(0)$ of the form

$$a_R(0) = 1 + \epsilon, \tag{1.20}$$

where ϵ is some positive number. Were such a trajectory to exist, then we would still be able to explain the total cross section in terms of Regge theory.

Therefore, to answer the question that we proposed at the start of this section, the pomeron is such a Regge trajectory. This Regge trajectory is unique for a number of reasons. First of all, we have no reason to believe that this Regge trajectory for the pomeron has any resonances. In more simple terminology, we don't have any evidence currently that the pomeron is a particle such as a proton. Rather, we can think of it as a mathematical proposal to bring Regge theory in line with the experimental data of the time.

As we moved on into the 70s and 80s, the pomeron terminology fell away. With the advent of the Standard Model and QCD, Regge theory was seemingly superseded. Despite the best efforts of the time, this pomeron seemed to exist mostly as a mathematical tool to bring our theories in line with the data and didn't have experimental backing. That

is, until particle colliders reached higher energies and an interesting class of particle collisions emerged.

When protons collide, there are sometimes interactions that leave a proton intact while the other dissociates, or break apart. These kinds of interactions represent 15% of all collisions and can be seen in Figure 1.16 In the 1990s, when the Hadron-Electron Ring Accelerator (HERA) was first beginning operation, these types of collisions were seen, but perturbative QCD was unable to fully explain these interactions. The characteristic momentum transfers of these collisions were low enough that perturbative series expansion was no longer a valid approach. As such, theorists were at a loss for a theoretical explanation of what was happening.

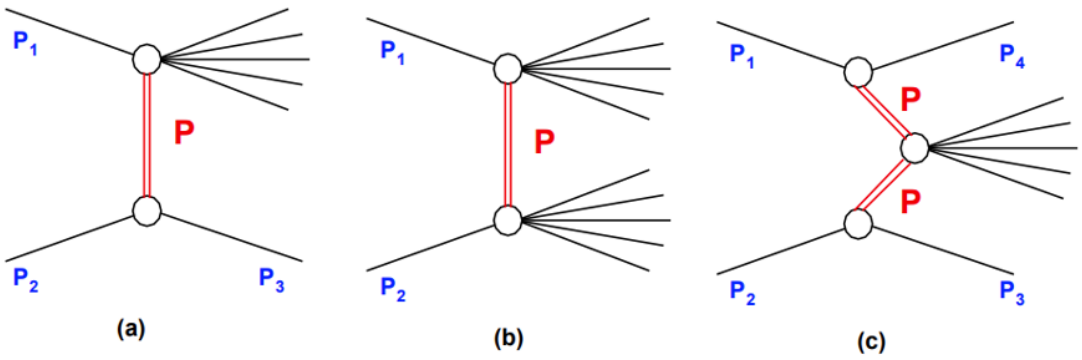

Figure 1.16: Examples of types of collisions that can be explained in terms of pomeron exchange. When collisions of these kind happened at HERA, the recently formulated QCD struggled to explain these kinds of collisions which led to a resurgence in talking in terms of the pomeron and its Regge trajectory. Figure extracted from [16].

Thus gave us the resurgence of the pomeron and thinking in terms of these Regge trajectories. It seemed that Tullio Regge was ahead of his time and his theory of strong interaction began to again gain traction. For now, this is where we shall end our introduction into talk of the pomeron, but we will revisit it in Section 3.3.2 to talk about how we can utilize modern particle detectors, and indeed how this dissertation itself, can help answer the question of what the pomeron is.

Chapter 2: Experimental Setup

Contents

This chapter will discuss in detail the equipment used to gather the data for this dissertation. All data was collected at the Large Hadron Collider (LHC) using the Compact Muon Solenoid (CMS) detector. Section 2.1 will start out with a description of the LHC complex and the various methods used to accelerate the particles to the energies at which they are collided. Section 2.2 will outline the methodology of modern particle detectors. Section 2.3 will briefly discuss the other experiments located at the LHC and their purposes. Section 2.4 will give an in depth discussion to the experiment used for this dissertation, the CMS detector.

2.1 The Large Hadron Collider

In the modern era of particle physics, the trend for exploring new regimes consists of pushing to larger sizes which allows the exploration of even higher energies. The LHC is certainly no exception to that trend, being both the largest and highest energy particle collider to date. Since its first collisions in 2010, it has been used these higher energies to probe previously unattainable kinematical regions by colliding combinations of protons and Lead-ions.

The LHC is located at the European Organization for Nuclear Research (CERN), which itself is a collaboration of mostly European countries that utilize the LHC and associated machinery to conduct research activities [17]. CERN is located in a suburb of Geneva, Switzerland on the Franco-Swiss border, with facilities spanning both countries. One of the original goals for the construction of the LHC was the discovery of the Higgs Boson, as discussed in 1.1.2, which was accomplished in 2012. In addition to that, the LHC is helping address many open questions in physics, such as the existence of extra dimensions, properties of dark matter, and other physics existing beyond the Standard Model.

In its primary mode of operation, the LHC is a proton-proton collider, with certain times dedicated to heavy-ion collisions which consist of lead-ions either being collided together, or with a proton. The beams themselves are accelerated in opposite directions with their paths crossing at 4 locations. At each of these overlaps, there exists one of the experiments discussed in 2.3 and 2.4 whose purpose is to observe and reconstruct the collisions happening between these beams. There are 2 general purpose detectors and 2 that focus on more specific physics processes.

The construction of the LHC represents one of the largest man-made objects ever created. It was a collaborative effort of over 100 countries to provide the funding for this 27 km ring which ranged from 50 to 175 meters underground. A picture of the LHC complex at surface level with representation of the ring's location can be seen in Figure 2.1.

The basic principle of circular colliders is that one can accelerate a charged particle,

Figure 2.1: A satellite photo of the LHC complex at surface level. Each of the 4 main experiments is shown. The actual ring itself is located underground at depths of up to 175 meters.

such as a proton or a lead-ion, via the use of an electric field described by

$$F = qE, \tag{2.1}$$

where E is the electric field and F is the force that is imparted upon a particle with charge q. In the case of the LHC, this q is either the charge of a proton, or 82 times that charge in the case of a lead-ion. As there is such a marked difference between the particle being collided, we can see that it isn't simply a matter of changing the source of particles, but rather an incredibly complicated process to adjust everything to account for the different charges of the colliding particles.

The path each particle takes as its energy is increased is different depending on whether its a proton or a lead-ion [18]. A breakdown of the different elements necessary

to accelerate the particles to their final energy can be seen in Figure 2.2. For protons, their path begins from a bottle containing hydrogen atom which is then ionized via use of an electric field to strip off the electrons. They are then injected into the PS Booster (PSB) at an energy 50 MeV from Linac2. At PSB they are then accelerated to 1.4 GeV, at which time they are fed into the Proton Synchrotron (PS) and accelerated even further to 25 GeV. From there, they enter the Super Proton Synchrotron (SPS) to be accelerated up to 450 GeV. They are subject to the extreme magnetic fields of the LHC which cause them to maintain their orbit as they are accelerated up to their final energy of 6.5 TeV, at which time they are they ready to be collided. The protons themselves are grouped together into what are known as bunches, which consist of groups of protons (around 1.2 x 10^{11}) every 7.5 meters.

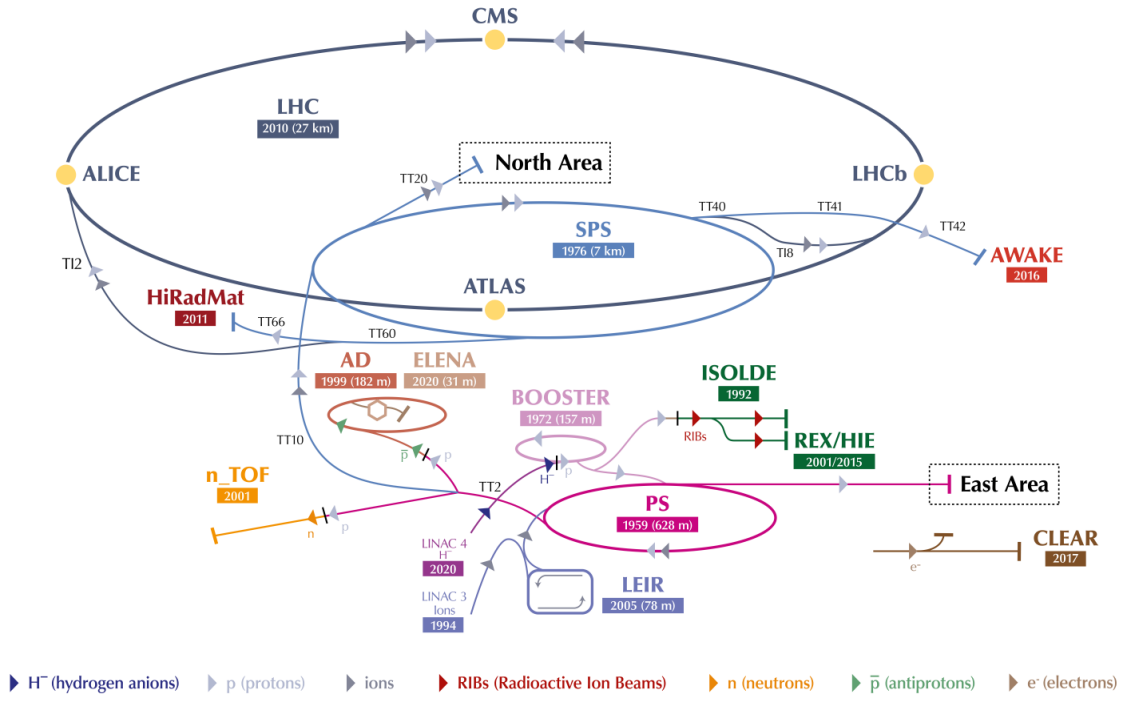

Figure 2.2: A graphical representation of the LHC complex. In this diagram, we can see the many different rings utilized in accelerating the particles up to their maximum velocities. Figure from [19]

.

Lead ions, on the other hand, have a much different path on their way to reaching their final energies [20]. They began their journey as a highly purified sample of lead atoms that are then heated up to 800°C. This causes the lead ions to vaporize and they are then subjected to an electron current which ionizes the gas. They are not all equally

ionized, however, and therefore must be accelerated to 4.2 MeV/u (energy per nucleon) and then passed through a carbon foil to get a pure sample of Pb^{54+}. After getting this pure sample of Pb^{54+}, it is then accelerated up to 72 MeV/u via the Low Energy Ion Ring (LEIR), upon which time it then converges to the path taken by the proton and enters the PS. There it is accelerated to 5.9 GeV/u, injected into the SPS where it is accelerated to 177 GeV/u, and finally it then enters the LHC to be accelerated to its final energy of 2.56 TeV/u. In the case of both protons and lead ions, upon being injected into the LHC they are injected going both clockwise and anticlockwise directions in a manner that allows them to collide at the 5 designated interaction points.

The manner in which the LHC accelerates the protons and lead ions up to their final energies of 6.5 TeV and 2.56 Tev/u, respectively, is through the use of its extreme electric fields. These fields are generated through the use of specialized radiofrequency (RF) cavities. There are 16 RF cavities located on the LHC, 8 for each direction. The cavities themselves open spaces inside a highly conductive material. They are specifically configured so that when an electromagnetic wave is applied to it at a specific frequency, a standing wave is created which can then be used to increase the energy of the particles circulating throughout the LHC. They are driven by an extremely high power klystron, which is a tube containing electron beam as can be seen in Figure 2.3. A klystron's purpose is to receive an input wave function and then amplify that signal greatly via the application of high energy electrons. This amplified signal is then passed on to the RF cavity through the usage of a waveguide. Once the RF cavity receives this amplified signal, it's then used to keep the particles tightly packed into their bunches which increases the luminosity by maximizing the number of collisions that occur. Additionally, the RF cavities provide energy to the particle bunches when they pass through. As the bunches pass through the RF cavity, a small amount of energy is imparted upon them as can be seen in Figure 2.4 and the specific configuration of the waveform means that the beam energy is only increased and the particle beams never hit a trough. By repeating this millions of times over, the energy will increase to its final values of either 6.5 TeV or 2.56 TeV/u for protons or lead-ions, respectively.

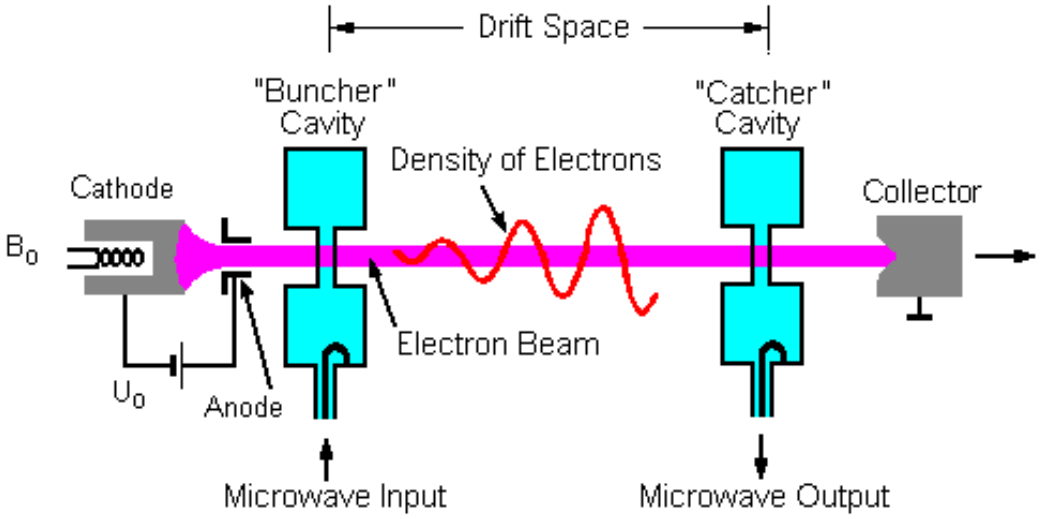

Figure 2.3: A klystron operates by producing an electron beam via the application of a voltage across the cathode. The "buncher" cavity receives the electron stream and the wave input. The combination of these two creates bunches of electrons that travel to the "catcher" cavity at the frequency of the input wave. This causes an amplification of the original wave and that signal passes through a waveguide to the RF cavity.

These particles are moving so close to the speed of light that they circulate the 27 kilometer ring 11,245 times per second when the particles are moving at their highest energies. Therefore it becomes vitally important to have a mechanism to keep them in a steady path around the ring in order to get them to eventually collide at these enormous energies. This is managed by very powerful magnetic fields which are produced from superconducting magnets. The basic principle of using a magnetic field to steer the particle beams can be seen from the following equation

$$\mathbf{F} = q\mathbf{v} \times \mathbf{B}, \qquad 2.2$$

where **F** is the force imparted upon the particle, **v** is the velocity of the particle, and **B** is the magnetic field that is acting upon the particle with a charge of q. Naturally, you're going to need a very complicated, and very powerful, system of magnets to keep particles moving near the speed of light tightly confined. As such, the LHC contains over 50 different types of electromagnets, each working in concert to ensure that the particle

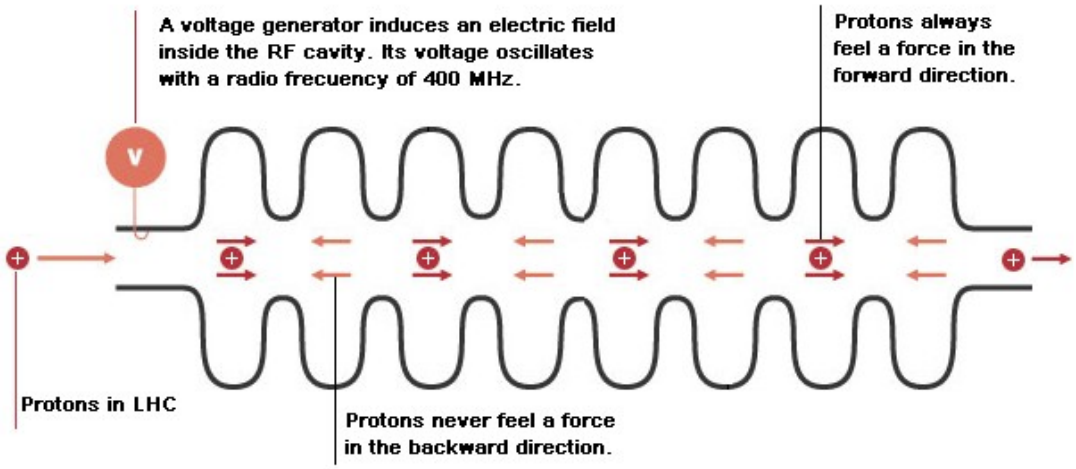

Figure 2.4: The main purpose of the RF cavities is to keep the particles bunched together as well as impart energy upon them during the initial phases. The specific frequency of the electric field inside the RF cavity allows the particles to only ever receive forces in the proper direction. Repeated loops through the LHC ring lead to the particle beam reaching its final energy after many passes.

beams stay on the proper path with incredible precision. The main dipoles are capable of producing magnetic fields up to 8.3 T which is more than 100,000 times the stronger than the magnetic field of the Earth. As these are all electromagnets, their strength is produced via the current running through them. To produce magnetic fields this strong, however, requires an equally large current. The currents needed can reach up to 11,080 amperes, but under normal circumstances a current of that magnitude would cause any material it was traveling through to melt. This fate is avoided by all of the LHC's magnets utilizing a liquid helium cooling system which reduces their temperature down to -271.3 °C. At this temperature, the electric cables used in the operation of these magnets enters a superconducting state which eliminates resistance or loss of energy.

The most important magnets for the operation of the LHC are the dipole magnets, the quadrupole magnets, and finally the magnets used to squeeze the beams right at the moment of collision. These dipole magnets, as seen in figure 2.5 are responsible for bending the paths of the particles and keeping them contained withing the structure of the LHC. There are 1232 of these dipole magnets, each measuring 15 meters and weighing 35 tonnes. Despite being called dipole magnets, each of them is additionally equipped with sextupole, octupole, and decapole magnets as well which allows for very fine corrections

to the magnetic fields. Another important type of magnet that is used by the LHC is a quadrupole magnet. There are 392 quadrupole magnets and their primary responsibility is preventing the beams from dispersing by keeping them focused into bunches. The final type of magnet that will be discussed in this section is responsible for the most elementary operation of any particle collider, the collisions themselves. These magnets perform this most crucial of operations by taking the (relatively) diffuse beams and condensing them down so that the proton bunches will have a higher chances of colliding. The function of these magnets can be seen in Figure 2.6

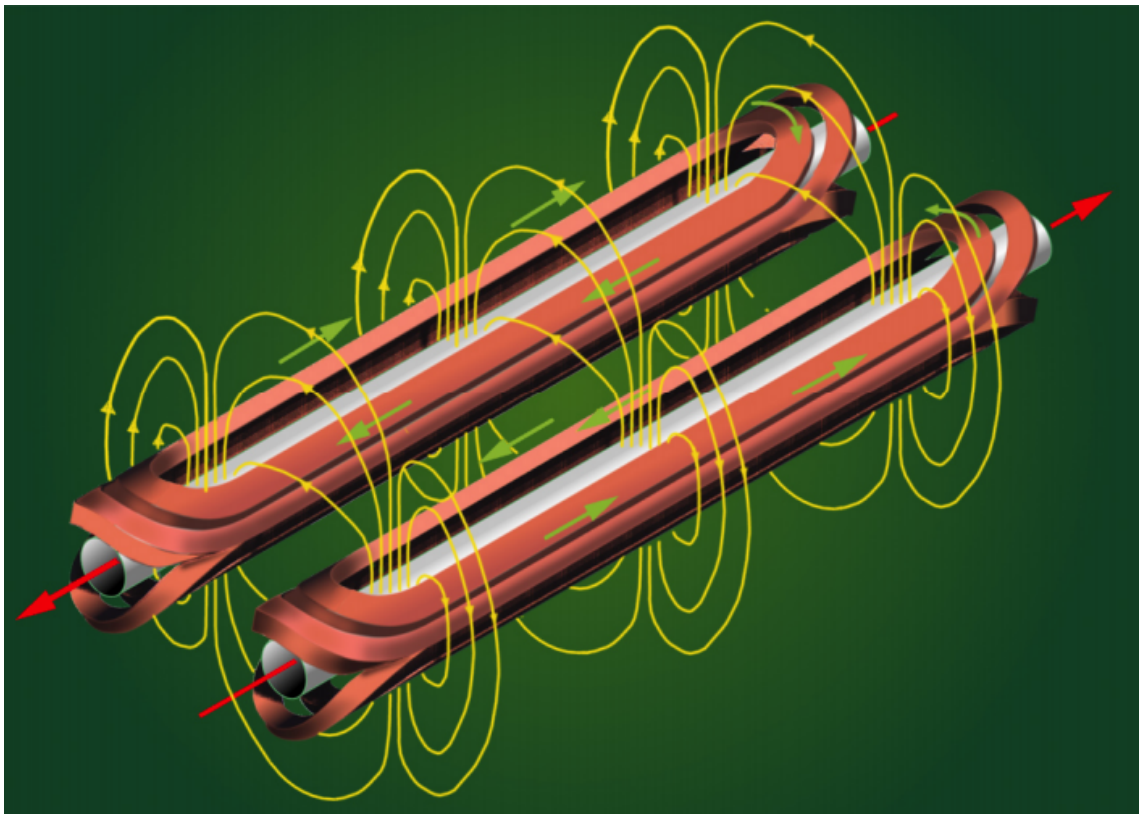

Figure 2.5: A diagram of one of the 1232 dipole magnets that are located within the LHC. These types of magnets are responsible for keeping the highly energetic particles constrained to a circular path throughout the LHC. Additionally, the magnetic fields that are produced by the dipoles can be seen.

As might be expected, running the LHC is by no means a simple feat in terms of energy expenditure. Particles are constantly being accelerated to speeds near the speed of light, but also each of the detectors require massive amounts of energy to function. The total energy used per year by the LHC is on the order of 750 GWh. This dissertation was written in Lawrence, KS, which boasts a population of 100,000 people, yet uses less

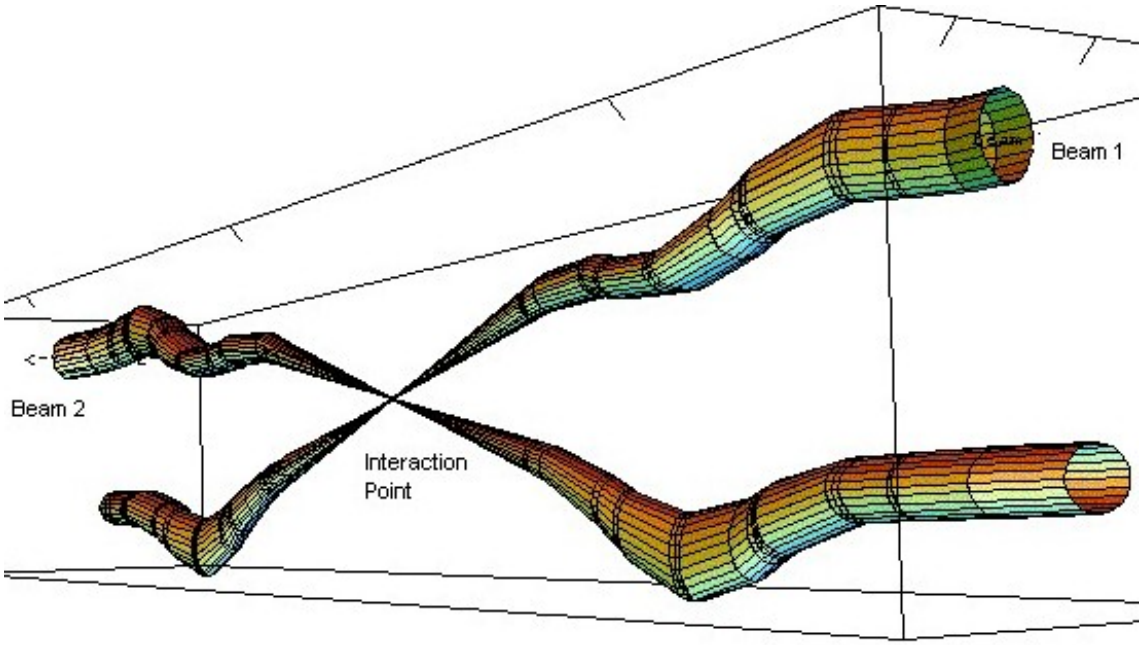

Figure 2.6: A representation of the paths the beams take before collisions. When circulating throughout the LHC, the beams are relatively diffused, which would make collisions between them a relatively rare event. In order to increase the interaction rate, the beams are condensed down to extremely small spaces just before colliding which drastically increases the chance of a collision.

than 5% of that energy per year.

2.2 Principles of Detectors

It's worth a brief discussion of the methods by which a detector actually "detects" anything. These are the most basic tools with which we are able to explore these unseen realms and so worth our time to have, at least at a basic level, an understanding of how they work and the limitations one must be aware of. Therefore the goal of this section is to discuss a couple different types of detectors and discuss how they function.

In the most basic terms, a detector is able to detect via interactions between the particles themselves and whatever material it is made of. This will induce some sort of change in the detecting material which can then be interpreted by additional machinery as "detecting" a particle. The fact that the measurement is altering the very material itself, in some limited capacity, hints that this process has very real limitations that need to be addressed. If we are to be conducting experiments, and more importantly drawing conclusions about nature from them, we must be aware of these limitations and actively

work to mitigate them. Thankfully, this fact was known by the scientists who designed CMS and so the 3 types of detectors we will talk about in this section all are uniquely suited for this task.

The first type of detector we will discuss are gas filled detectors, as seen in Figure 2.7. Their typical construction is a metallic cylinder that is full of gas, with a single wire running through the center of this gas chamber. This wire running through the center of the cylinder is the positive electrode, or anode, while the cylinder itself is the negative electrode, or cathode. A large potential difference is applied between the cathode and anode, which will cause any charged particle within the gas to be accelerated to either the wire or the cylinder, depending on its charge. It was said previously that a detector detects via interaction between the detector and the particles themselves. In this case, that interaction happens with the gas inside the chamber. Particles that fly through it will impart some energy to the gas particles, causing them to become ionized. These ionized particles then are attracted to the cylinder, while the electrons that are removed are attracted to the wire. When the electrons reach the wire, this creates an electrical pulse which is then passed on to be interpreted by software as a particle detection. For gas detectors, the sensitivity to the level of ionization depends on the potential difference that is applied across the cathode and anode.

The next type of detector that is utilized at CMS are semiconductor detectors. As the name implies, their primary construction is some sort of semiconducting material, such as silicon. Similarly to a gas detector, ionizing radiation interacts with the material in order to create an electrical pulse. As it passes through the semiconductor, the radiation will create free electrons and electron holes. The number of these created is proportional to the energy of the initial radiation. Therefore, when a potential difference is applied across the semiconducting material, any free electrons move to a node and this can then be passed on to machinery where it is interpreted as a particle hit.

The final type of detector we will discuss are scintillation detectors, as can be seen in Figure 2.9. As the principle variation between detectors thus far has been the material of its construction, it should come as no surprise that these detectors are composed of

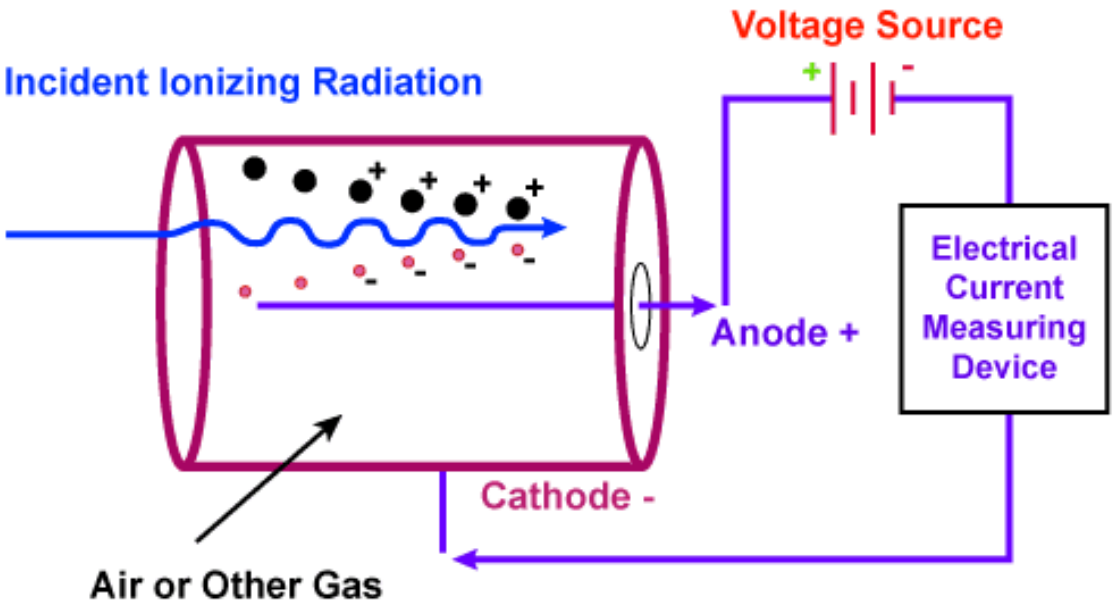

Figure 2.7: Simple schematic of a gas type detector. As ionizing radiation enters the cylinder, it causes the gas atoms to ionize and the electrons are attracted to the central wire. This electrical pulse is then sent on to be measured and interpreted as a particle hit

materials that scintillate, or emit light. When ionizing radiation strikes these materials, they will emit light. A critical difference here, however, is the presence of additional objects such as a photomultiplier tube (PMT). PMTs absorb the light emitted from the scintillators and then create avalanches of electron which then go on to create an electrical signal that can be interpreted by the software as particles detected. Not all scintillating detectors have avalanches such as this, but those that do often have extreme sensitivity and can often detect individual photons that strike their detectors.

A subset of scintillating detectors that is used frequently in high energy physics is Cherenkov detectors. In this case, the material used is a dielectric, which is a material that is electrically insulating and one that becomes polarized in the presence of an applied electric field. Therefore, when ionizing radiation passes through, it creates a disturbance in the medium as it becomes polarized. If the radiation is moving with sufficient speed, namely faster than the speed of light in that medium, it will scintillate as the detectors described above. These types of detectors are frequently used in high energy physics because of the inherent noise cancellation properties. Most of the particles we produce in high energy physics tend to be, as one might guess, high energy and therefore fast.

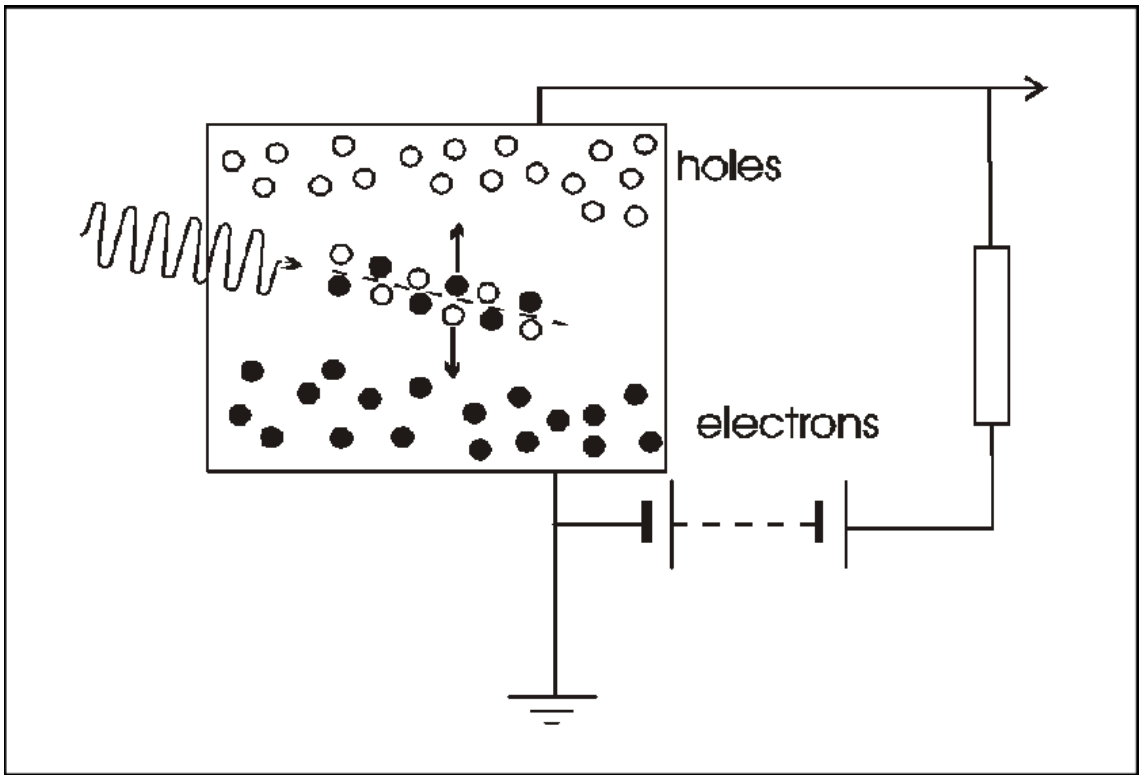

Figure 2.8: Simple schematic of a semiconductor detector. As the ionizing radiation passes through the material, it creates electrons and hole proportional to its energy which will migrate through the material. When the electrons reach the bottom, they create an electrical pulse.

Having a detector that is only capable of detecting fast particles allows for some noise reduction.

One important aspect of detector design is the property known as response time. Response time is defined as the time it takes the current generated by the detector to rise to a value that's 63.2% of the final state value. In other words, this property defines how quickly a detector is able to go from initial detection to reporting that detection. Oftentimes the experiment in which one is operating encourages the use of different types of detector based off how quickly detection is needed. In an experiment such as CMS where collisions can happen every 25 nanoseconds, this is extremely critical. Therefore each of the detector types talked about during this section can have response times in the nanosecond range which allows operation to proceed even with collisions happening so frequently.

The final issue with detectors that needs to be discussed is the inherent limitations to the materials used. No material is perfect, and so that means that there is no such thing

as a perfect detector. The most notable limitation that is present among all types is the fact that there is some downtime between detections. One cannot have a detector that detects particles at all times. For example, when a particle strikes a scintillation detector there will be a brief period of time when the material needs to "rest" in order to be able to scintillate again and detect more particles. Typically, this is an extremely small time, but it's worth noting in order to appreciate the level of complexity and design of a machine such as CMS. All the topics discussed in this section have been delved into, with much more detail, in order to create a machine that is able to study these fundamental aspects of the universe in the best possible manner.

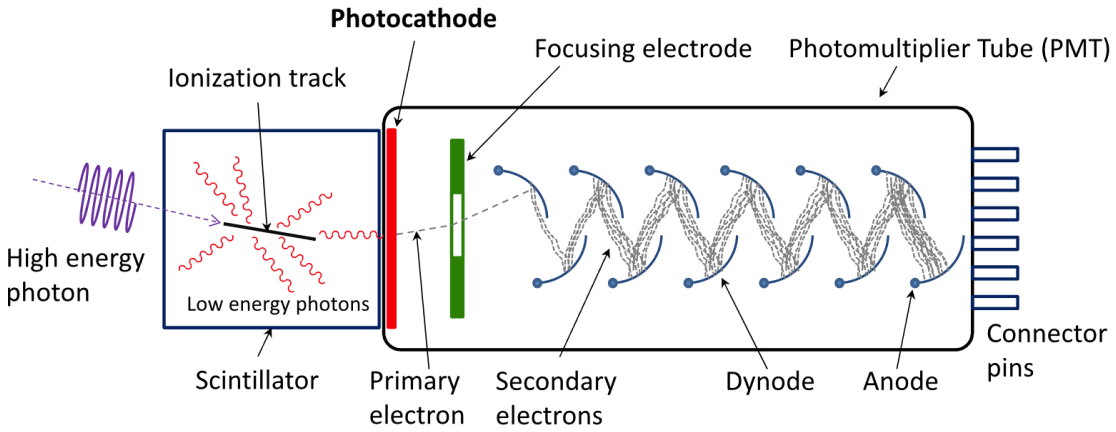

Figure 2.9: Schematic of an average scintillation detector. As the ionizing radiation enter the scintillator, many low energy photons are emitted which then interact with a photomultiplier tube to enhance the low energy photons and create an electrical signal.

2.3 Experiments at the LHC

The goal of this section will be to, in brief, discuss the experiments at the LHC that were not used in collection of the data used in this dissertation in order to have a comprehensive description of the LHC. These experiments are A Toroidal LHC ApparatuS (ATLAS), A Large Ion Collider Experiment (ALICE), and Large Hadron Collider beauty (LHCb). In the section following this, section 2.4, we will thoroughly discuss the experiment that was used to collect the data for the purposes of this dissertation, the Compact Muon Solenoid (CMS).

2.3.1 ATLAS

One of the two general-purpose detectors is the ATLAS experiment [21], as can be seen in 2.10. As such, its goal is to attempt to fully reconstruct the particle collisions that occur. It is composed of three toroidal superconducting magnets which aid in particle identification. Being a general purpose detector similar to CMS, discussed is section 2.4, it shares many of the same physics goals such as looking for extra dimensions or searching for dark matter. The different construction and technical approaches allows independent verification of physics results to allow a higher degree of confidence, such as in the case of the discovery of the Higgs Boson in 2012.

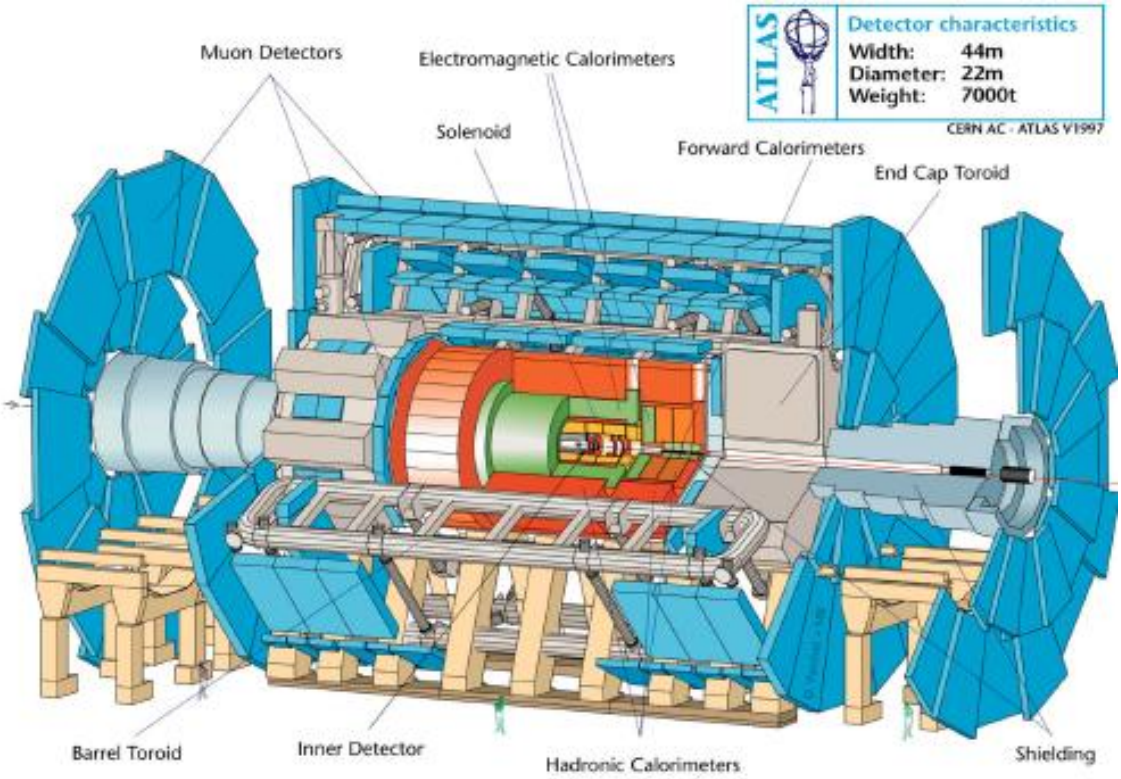

Figure 2.10: The full general purpose ATLAS detector highlighting many of its subdetectors.

2.3.2 ALICE

While the majority of operations at the LHC are focused on proton-proton collisions, there exists a subset that focuses on the heavy-ion runs and one detector in particular specializes in this kind of physics. One such experiment is ALICE [22] that can be seen in

Figure 2.11. One of the main goals for ALICE is the study of strongly interacting matter at extreme energy densities which is known as quark-gluon plasma. This type of matter is similar to the state of the universe moments after the Big Bang and studying this kind of matter helps further the understand of QCD. Additionally, they study confinement and chiral-symmetry restoration.

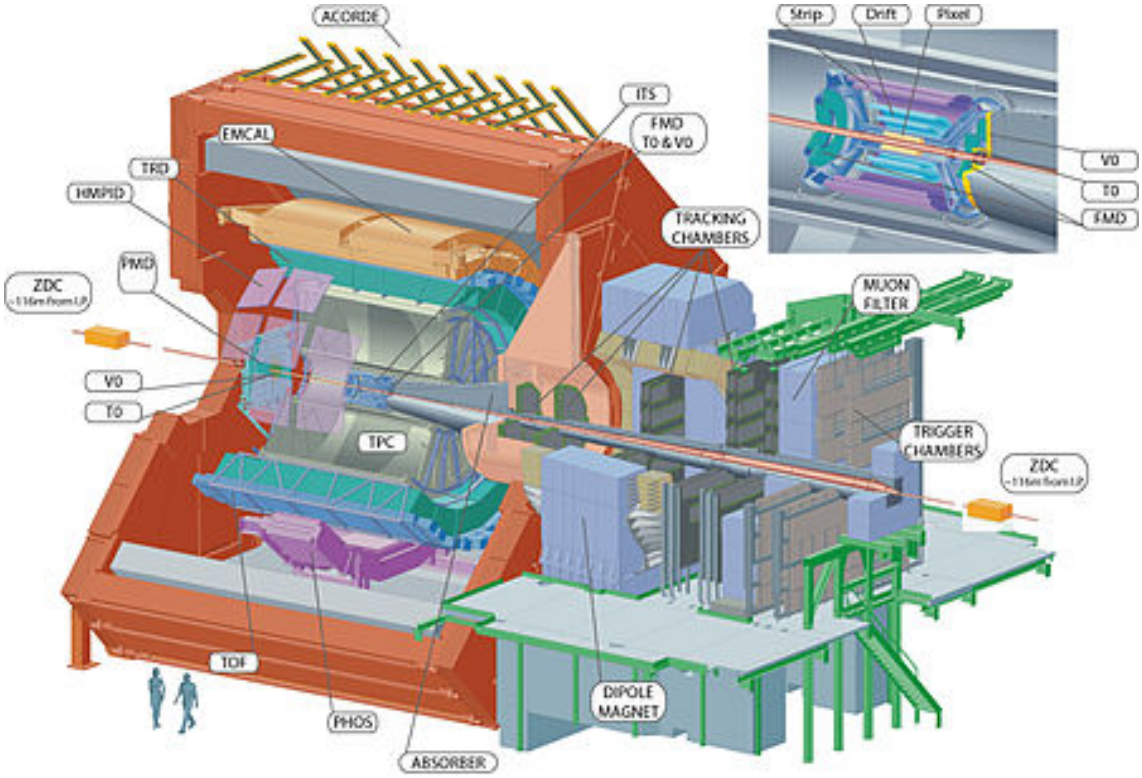

Figure 2.11: The full ALICE detector highlighting many of its subdetectors identified as well as humans for scale.

2.3.3 LHCb

The experiment we will be briefly discussing before finally talking about the detector used in this analysis is the LHCb detector [23] as seen in 2.12. As one might expect from its name, LHCb focuses on studying the beauty (or b) quark. By doing so, they hope to understand the differences that are observed between matter and antimatter. Interestingly, LHCb opts for an open detector, unlike those seen at ATLAS or CMS which are completely enclosed whose goal is to fully capture the outgoing particles rather than specializing as LHCb does. Additionally, LHCb is able to study various forward physics topics due to their overlap with the region where b quarks typically appear.

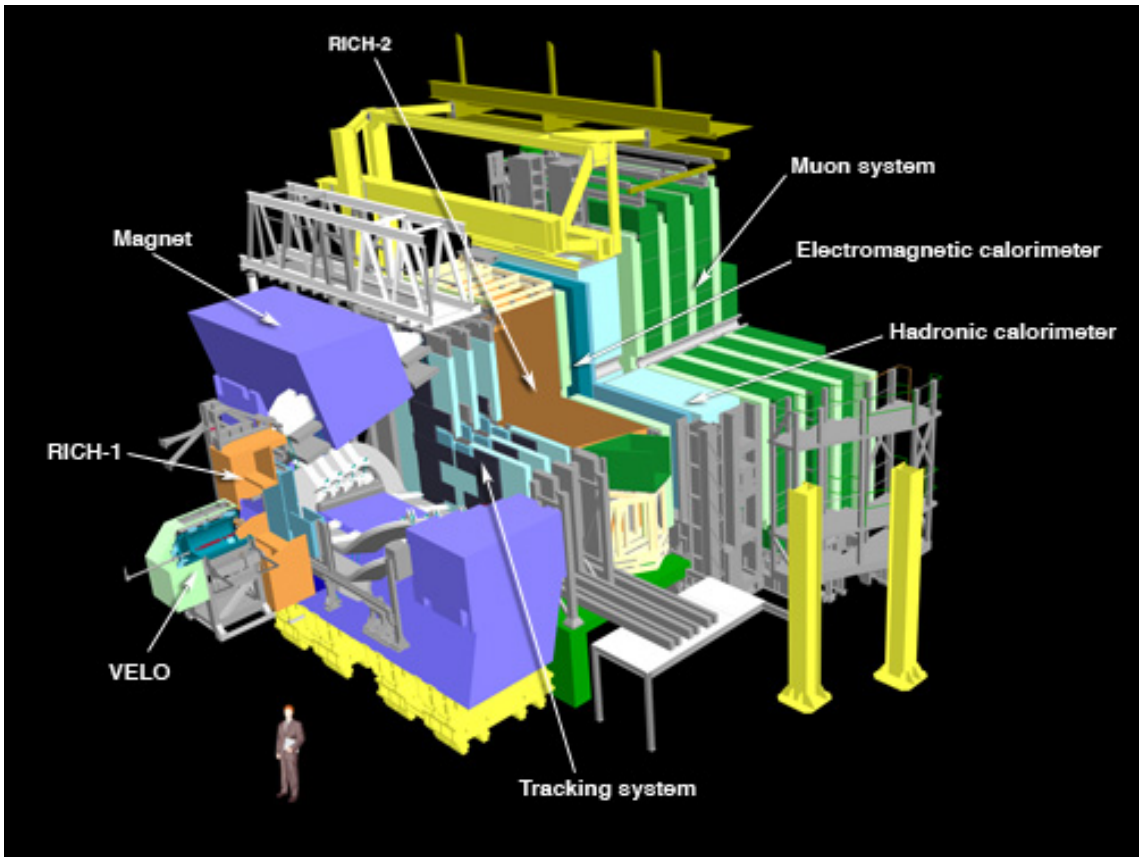

Figure 2.12: The full LHCb detector highlighting its different subdetectors as well as a human for scale.

2.4 The CMS detector

The final experiment we'll be discussing is the CMS detector [24], which was used in the gathering of the data for this dissertation. Similar to ATLAS, the CMS detector is a general purpose detector whose goal is to fully reconstruct the outcome of a particle collision. Therefore, it employs as much coverage as possible in order to minimize the amount of particles that escape detection. Indeed, CMS is able to detect in an almost full 4π solid angle. The "compact" nature of CMS is a relative thing, as it weighs in as 12,500 tonnes, has a length of 21.6 meters, and a diameter of 14.6 meters. A diagram of CMS can be seen in Figure 2.13 highlighting the different elements of the detector that we will discuss more in depth in the following sections. CMS employs a concentric cylindrical construction around the beam axis, employing an almost onion-like design where each layer specializes in detecting a certain class of particles. At the heart of its construction

is the superconducting solenoid magnet. which aids in particle identification by bending charged particles in characteristic paths. Additionally, we will discuss the silicon tracker, the electromagnetic calorimeter, the hadronic calorimeter, various forward detectors, and finally the muon detector. A cross section of the different layers that make up the onion of CMS can be seen in Figure 2.14 and will be beneficial to reference in the following sections.

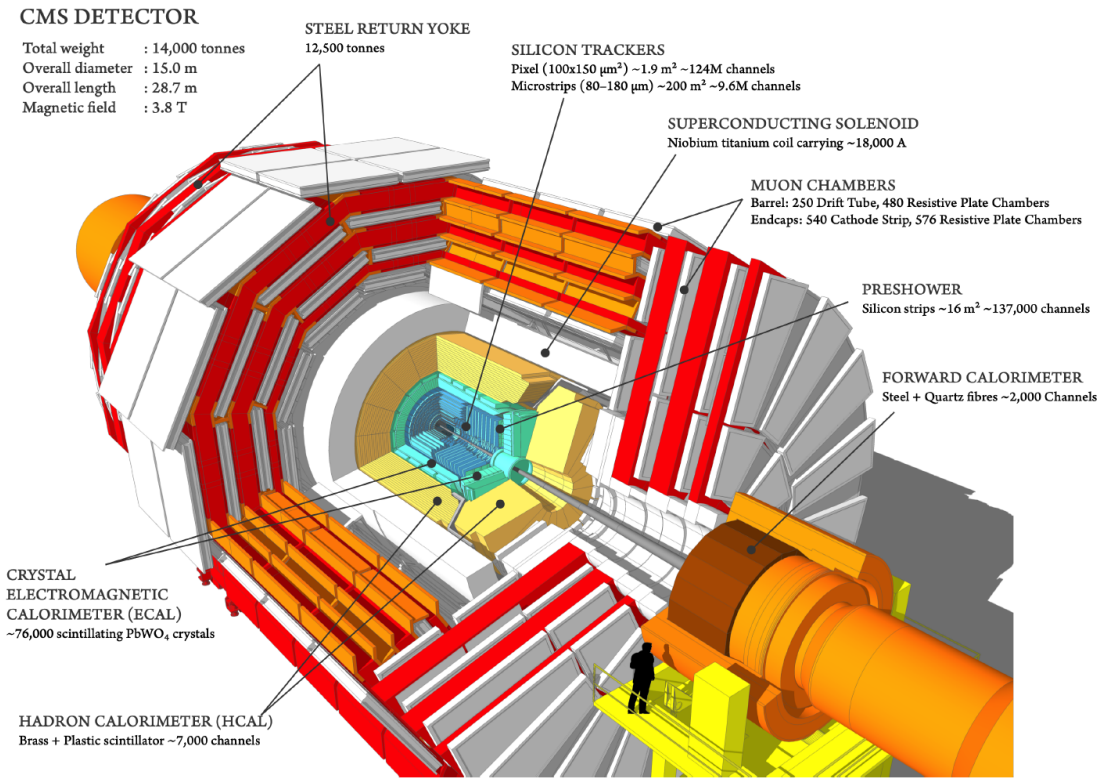

Figure 2.13: The full CMS detector with a human standing by it to illustrate the large scale of the detector. Additionally, each of the various subdetectors is labeled. Figure from [25]

When discussing the composition of CMS, it will also be helpful to first discuss the coordinate system used throughout the experiment. CMS uses a right-handed coordinate system, with $\hat{\mathbf{x}}$ pointing towards the center of the LHC, $\hat{\mathbf{y}}$ pointing perpendicularly upwards to the LHC ring, and $\hat{\mathbf{z}}$ pointing in the anticlockwise direction when looking at the ring from above, as can be seen in Figure 2.15. This rectangular coordinate system, however, is not the most commonly used in CMS. A spherical coordinate system is the more typical one used with the azimuthal angle ϕ being defined via the $\hat{\mathbf{x}}$-axis in the x-y plane and the polar angle ϑ being defined via the $\hat{\mathbf{z}}$-axis in the z-y plane. Another common way to discuss

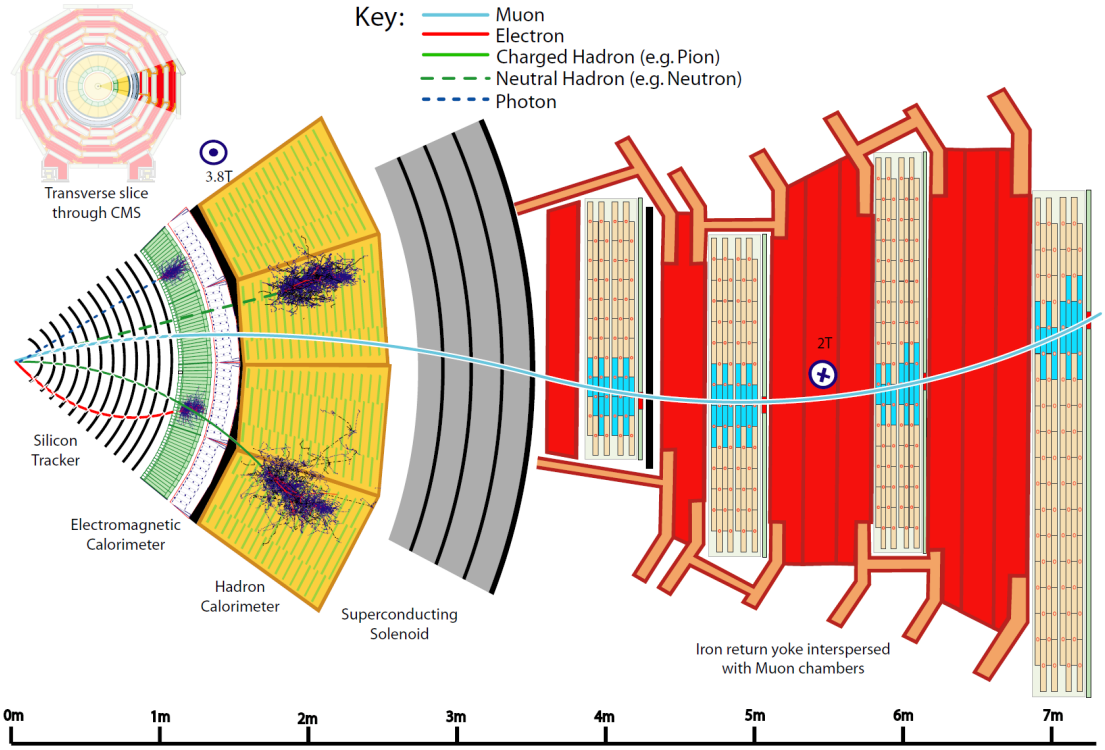

Figure 2.14: A cross section of the CMS detector. In this, you can see each of the individual layers that compose it as well as the paths of various particles throughout the detector. The different paths ending represents it being detected in that specific layer.

angles in the z-y plane is to use a pseudorapidity, or η, because of the fact that differences in pseudorapidity are Lorentz invariant and this allows us to have a coordinate system not dependent upon the longitudinal boost of the reference frame. Pseudorapidity can, however, be related back to the polar angle through the use of a simple transformation,

$$\eta = -\ln(tan(\frac{\vartheta}{2})). \tag{2.3}$$

2.4.1 The Solenoid Magnet

The driving force behind the ability of the CMS detector to correctly identify and observe the paths of all the outgoing particles is its extremely large magnetic field. This is because the larger the magnetic field, the sharper the curve of the path of the charged particles. Analyzing this curvature is the main way to identify the momentum of the

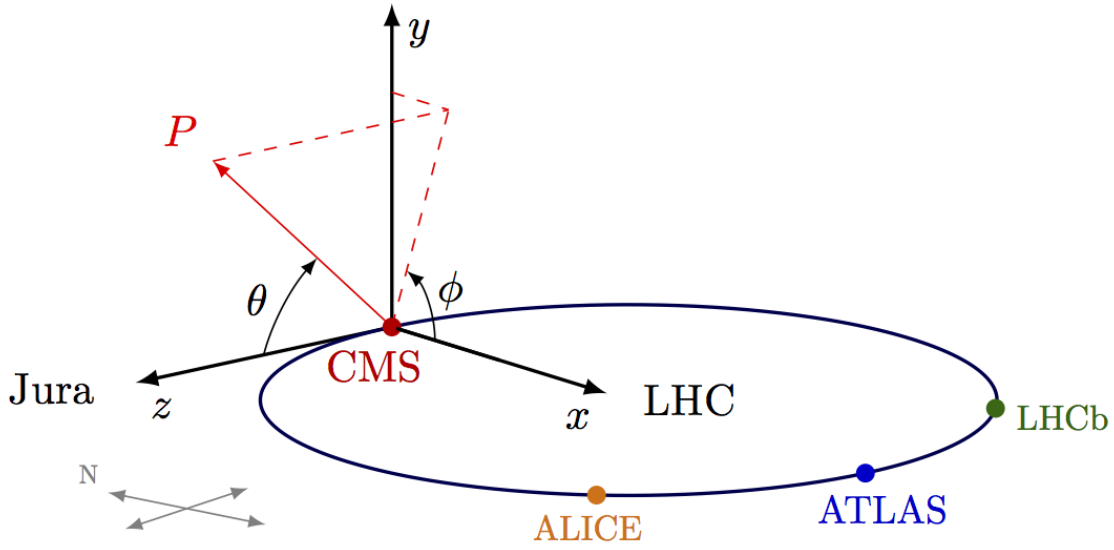

Figure 2.15: The coordinate system used by CMS overlaid with the LHC ring. The typical $\hat{\mathbf{x}}$, $\hat{\mathbf{y}}$, and $\hat{\mathbf{z}}$ direction can be seen along with the more commonly used spherical coordinates.

particles which then aids in the identification of the myriad particles that are produced in collisions. The solenoid is capable of reaching a massive 4 tesla, over 100,000 times larger than the magnetic field of the Earth. It accomplishes this via the use of a superconducting coil with 2168 turns which carries an electric current of 19.1 kA. The dimensions of this solenoid are 12.9 meters long and a 5.9 meter inner bore diameter.

The coil itself is composed of four layers that are made from a stabilised reinforced NbTi conductor that is mechanically reinforced with an aluminum alloy. In order to operate in a superconducting state, a portion of the solenoid operates at liquid helium temperature. Additionally, the solenoid is housed within a steel structure that is known as the yoke. The yoke is a comprised of a 12 sided wheel-like structure that surrounds the magnetic solenoid to provide support. Another role of the yoke is to form the skeleton of CMS as a whole and additionally return the magnetic flux and is therefore also known as the "return yoke." The magnetic field strength and lines themselves can be seen in 2.16. As with any solenoid, the magnetic fields within the coil are uniform and also where the strongest magnetic fields are generated. The behavior of the "return yoke" can also be seen via the path of the magnetic field lines on the right hand side of the figure as well.

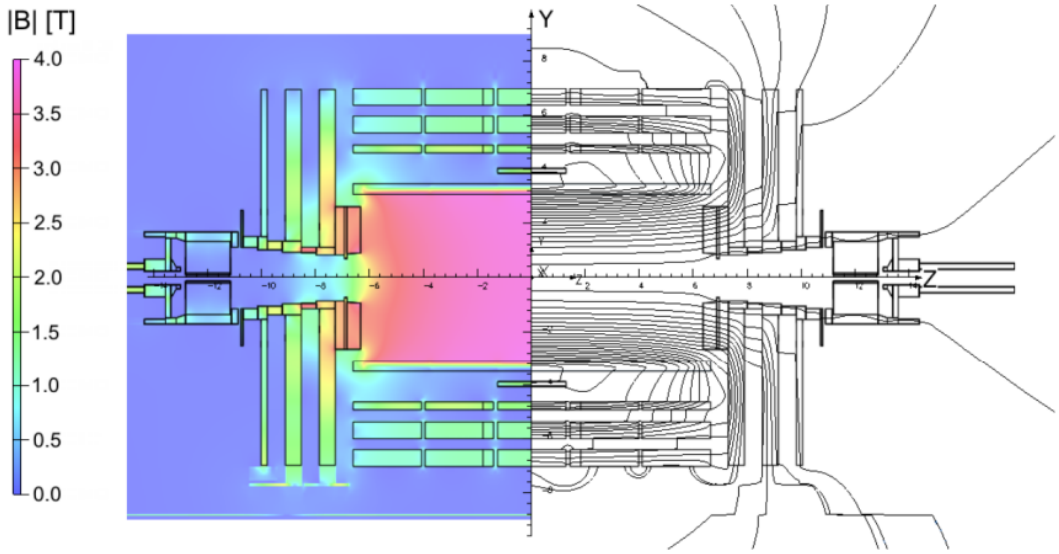

Figure 2.16: On the left hand side we can see the strength of the magnetic fields at various points in CMS, with the maximum being inside the coil as expected. The right hand side shows the magnetic field lines themselves. Figure from [26].

2.4.2 The Silicon Tracker

The superconducting solenoid is a single part of the larger whole in particle detection and reconstruction in CMS. Its usage allows very precise measurements, but this is because of the support of many other subsections, such as the silicon tracker. The silicon tracker is a semiconductor detector whose role is to provide position measurements of charged particles in order to reconstruct the paths taken by them after the in initial collision. These paths are what are known as "tracks" and, as the silicon tracker is the piece closest to interaction point, it is instrumental in obtaining the full picture of what happens when particles collide. Therefore, the silicon tracker is designed to have a very high resolution to allow reconstruction of these extremely small and fast moving particles with very little downtime as the collisions are happening as quickly as every 25 nanoseconds. Additionally, the silicon tracker's goal is to not disturb the particle when it is taking these measurements. As such, it needs to be very lightweight in terms of interaction so as to not interfere with their trajectory, yet still hard enough to resist the high amounts of radiation it gets from being so close to the beamline. The decision was made to construct it entirely out of silicon. At the very center of the detector, there are

the pixels and, further out, there are the silicon microstrips. Both of these layers register the hits from particles moving them which produce a small electric signal that is then amplified and joined with information from detectors further out in order to fully recreate the path of the particles.

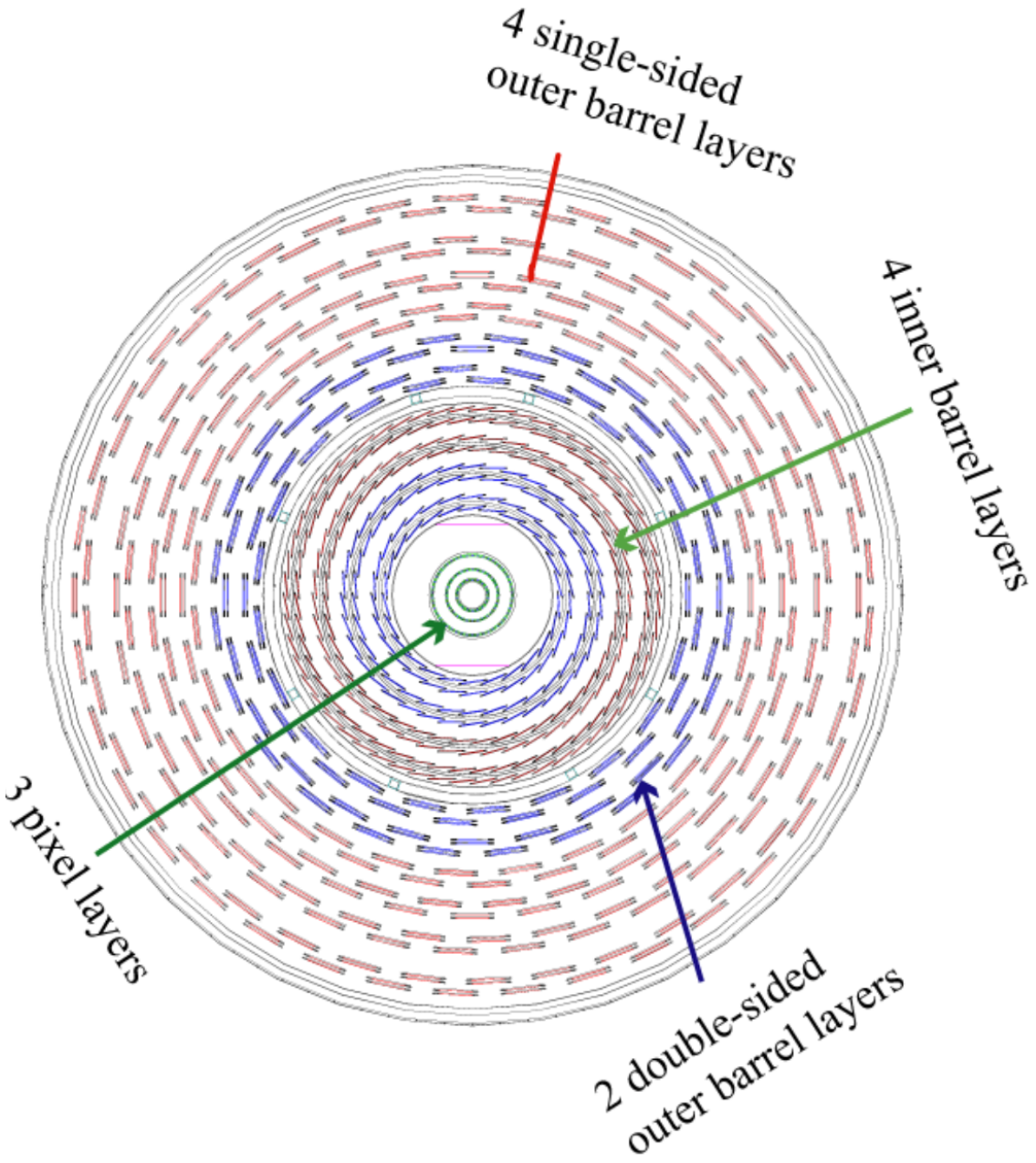

Figure 2.17: View of the CMS silicon tracker in the plane perpendicular to the beam. As a particle moves from the center, it must pass through the different layers which allow the path to be reconstructed.

The silicon tracker has a pseudorapidity coverage of $|\eta| < 2.5$, a length of 5.8 meters, and a diameter of 2.5 meters [27]. It can separated into two sections, the silicon pixel

section and the silicon strip section. As seen in Figure 2.17, the tracker is composed of concentric rings of pixel rings at the center and then strip rings further out. When a charged particle travels outwards, it must pass through each of the rings in turn. Each of these rings will record a hit and, through the use of the CMS reconstruction software, the overwhelming amount of information that is generated can be broken down into separate particle tracks and IDs. The pixel tracker is composed of 1440 modules comprising 3 barrels at distances of 4.4, 7.3, and 10.2 centimeters, respectively. There are also two endcap discs on either side of the barrel located at $|z|$ = 34.5 centimeters and $|z|$ = 46.5 centimeters. The resolutions of each of the pixels is approximately 10 μm in rϕ and 20-40 μm in z. The strip portion is composed up of 15 148 silicon strip modules that are configured into 10 barrel sections surrounding the inner pixel layers. Additionally, there are 3 small and 9 large endcap disks. The four sections composing the strip detector are the Tracker Inner Barrel (TIB), the Tracker Outer Barrel (TOB), the Tracker Inner Disks (TID), and the Tracker Endcaps (TEC). Altogether, these pieces of the silicon tracker work to allow CMS to have an unprecedented look at the output of particle collisions.

2.4.3 The Electromagnetic Calorimeter

The next layer to discuss is the Electromagnetic CALorimeter (ECAL), which is responsible for the absorption and detection of electrons and photons [28]. In order to do this, a very robust material is needed and therefore it is composed of lead-tungstate ($PbWO_4$) which has an extremely short radiation length. What that means is that when an electron or photon strikes this material, its energy is quickly attenuated which is vital when collisions are happening at the LHC every 25 nanoseconds. An additional property is the very fast scintillation in lead-tungstate which leads to 80% of the light is emitted within the 25 nanoseconds between collisions. The combination of these two properties means that a lead-tungstate construction is ideal to for the detection of electrons and photons. The ECAL is composed up of 36 supermodules, each of which has around 1700 $PbWO_4$ crystals inside of it. Additionally, each of the endcaps is also made from the same types of crystals with 7324 per endcap. Each of these crystals has about the volume of a small

cup of coffee and weighs in at 1.5 kg.

An electron or photon that strikes one of these crystals with sufficient energy will produce photons via bremsstrahlung radiation. These photons will, in turn, strike the crystals again and produce their own photons and this is what is known as a cascade. This process will repeat until all the energy is absorbed by the detector. This emitted light from the collision of photons or electrons can then be measured by the photodetectors because the amount of light that is produced can be related back to the original energy of the particle that set off the cascade. These photodetectors are crucial for the detector's operation and they can be found on the back of each of the crystals. In the barrel region, there are two avalanche photodiodes on each crystal, while the crystals on the endcap have vacuum phototriodes.

At the front of each of the endcaps, there are preshower detectors. Their goal is to help sort through the massive amount of photons that are present in these collisions. It allows CMS to distinguish the case where you have a single high-energy photon, which is indicative of interesting physics, and the more mundane closely grouped low-energy photons. The preshower detector is made of two layers of lead with a layer of silicon strip detectors. Like most aspects of CMS, the crystals themselves are kept at a constant temperature of 18°C in order to maintain peak response and signal amplification.

2.4.4 The Hadronic Calorimeter

The goal of the Hadronic CALorimeter (HCAL) is to measure the energy, position, and time of arrival of hadrons, which as discussed in Section 1.3 are particles that are made of quarks and gluons (e.g. protons, neutrons, pions) [29]. Additionally, because of the complete coverage offered by the HCAL, it can give indirect measurements of particles such as neutrinos that are much harder to directly measure. This is because of the hermetic design of the HCAL. By detecting, to the best of its very good ability, every particle that it can, a full picture of the collision can be obtained and any imbalances would indicate that one of these difficult to detect particles were created. Part of this hermetic design is ensuring that there are no straight paths out of the center that doesn't pass through one

layer or another on its way out. Therefore, the layers are slightly staggered to make sure that there are no gaps.

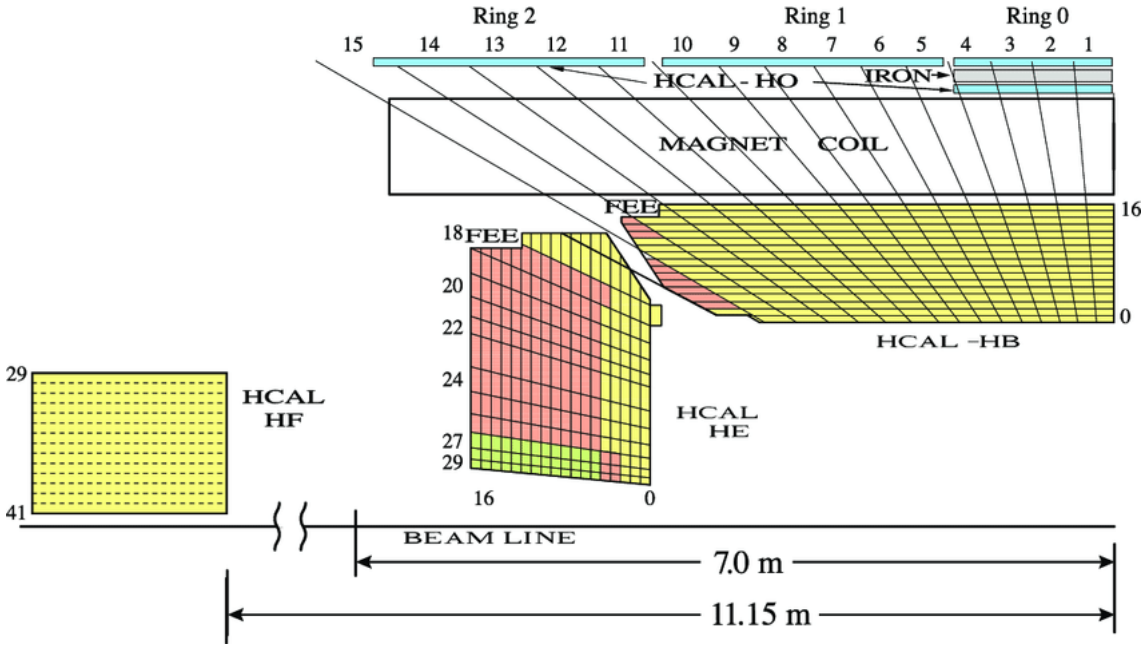

Figure 2.18: Schematic of the Hadronic CALorimeter (HCAL) and its various subsystems. We can see here the hadron outer (HO) subsystem and how it gets its name from being outside the magnet coil.

HCAL is broken up into four distinct elements as can be seen in Figure 2.18. The hadron barrel (HB) and hadron outer (HO) comprise the barrel itself, while the hadron endcap (HE) and hadron forward (HF) comprise the edges of HCAL. Interestingly, portions of HCAL encompasses portions of the superconducting solenoid as talked about in Section 2.4.1. HO sits outside the magnet and ensures that there are no energy leaks that go undetected and helps HCAL maintain its hermetic design. HB and HE make up the standard barrel-like design that we've seen thus far repeated for various subsystems in CMS. HF, however, is the forward portion and its goal is to measure particles that are generated at very high pseudorapidities, or, in other words, very close to the beamline.

HCAL implements alternating layers of brass-alloy absorber and active plastic scintillator plates that will produce a signature rapid light pulse as a particle passes through it. Each of these plates covers an area of $\Delta\eta \times \Delta\phi = 0.0087 \times 0.0087$ rad. There are 17 layers of plastic scintillator plates that are alternated with the brass-alloy absorber plates in order to form 16 projective towers in each half barrel. When a particle strikes one of

the scintillator plates, it is then sent to a photodetector which will then amplify the signal. Many instances of this in a given region result in what is known as a "tower," and the resulting amount of light that is collected can then be related back to the energy of the inital particle.

2.4.5 Very Forward Detectors

The majority of the machinery in CMS is dedicated to detection of particles in the vicinity of the interaction point, but there remains important physics that is happening close to the beamline. In order to detect these types of particles, there are several dedicated subsystems to CMS that focus on this region." This does, however, present an issue in the fact that anything close to the beamline under normal circumstances would be constantly bombarded with enough radiation that even the hardest radiation shielding would fail over the course of a run. To circumvent this, these forward detectors are present only in situations where the radiation will be at a manageable level. These situations are low luminosity proton-proton collisions, proton-lead collisions, and lead-lead collisions. The two forward detectors we will discuss, in brief, is the Centauro And STrange Objects Research (CASTOR) detector and the Zero Degree Calorimeter (ZDC).

CASTOR is a calorimeter that is located extremely close to the beamline (around 1 cm away) at approximately 14.4 meters from the interaction point [30]. As it is only on one side of the detector, CASTOR has a pseudorapidity coverage of $-6.6 < \eta < -5.2$. It is composed of plates made out of tungsten and quartz and is a Cherenkov detector. The primary goal of its construction was in search for deeply penetrating particles, like strangelets, that are connected to exotic events that are seen in high energy cosmic ray interactions. However, as a detector close to the beamline, it is also very useful for finding rapidity gaps which can be signs of interesting physics. Overall, the CASTOR detector is in a very unique position at the LHC because no other experiments have a calorimeter with this η coverage and this gives any analysis using a very large benefit.

The other forward detector we will discuss is the ZDC, a Cherenkov detector like CASTOR, that is composed of tungsten absorber plates and quartz fibers as the active

medium [31]. A large difference, however, is that there are 2 ZDCs and they are located ±140 m from the interaction point, which corresponds to a pseudorapidity of $\eta > 8.3$. It also has myriad uses in heavy-ion collisions as it is too near the beamline to be used in proton-proton collisions. Most typically, it is used for determination of the centrality of heavy-ion collisions by measuring the numbers of nucleons that do not participate in the collision. It can, however, be used in many types of analyses such as charge exchange processes or looking for events with intact lead ions, such as this analysis.

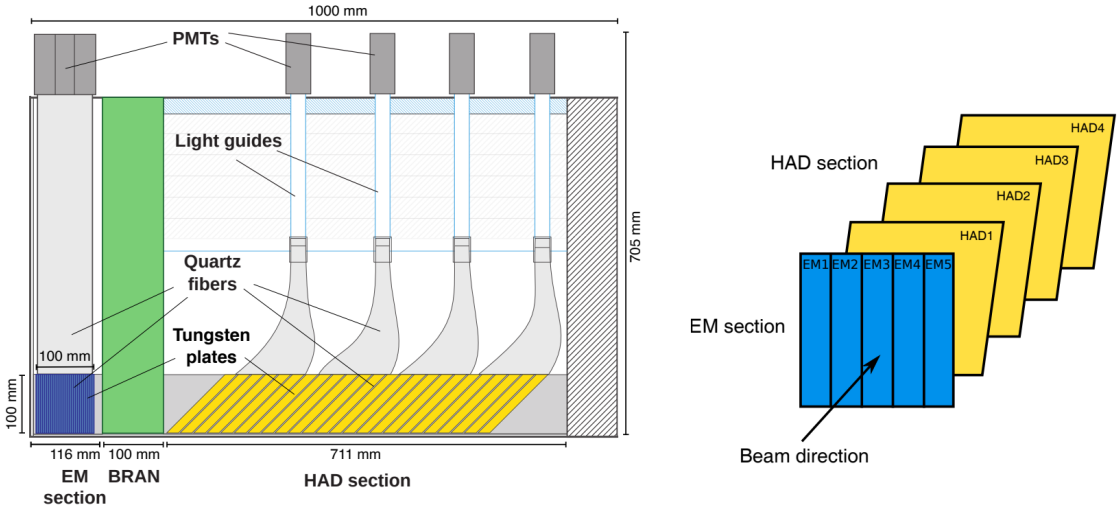

Figure 2.19: A schematic view of the ZDC with the segmentation represented on the right hand side.

2.4.6 Muon Chambers

The final layer we will talk about are the muon chambers which, as one might guess from the naming of the experiment, are a sort of specialty for CMS. Muons are rather tricky to detect as they have much larger masses than their cousins, the electrons, which leads to them not undergoing brehmsstrahlung radiation as readily. As such, they can pass right through the ECAL and HCAL without leaving a trace of their passing. In fact, a muon can pass readily through several meters of iron without interacting. The only path they would leave would be right at the beginning at the silicon tracker. Therefore, CMS was constructed with this limitation in mind. A very special set of chambers, known of muon chambers, were placed on the outer limits of the detector whose sole goal was to detect and measure these relatively hard to detect particles.

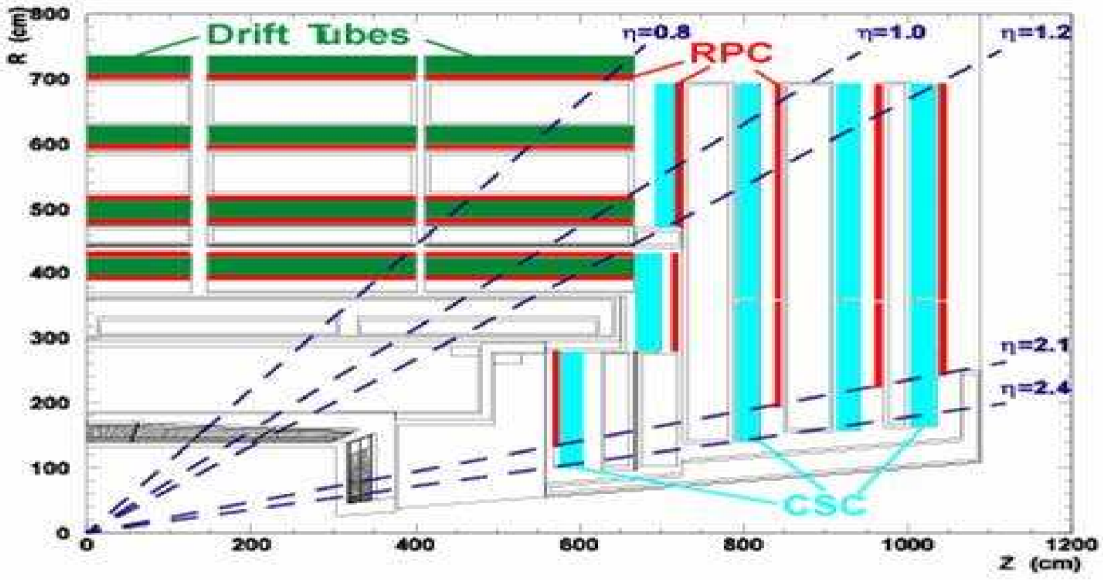

Figure 2.20: Schematic of the muon chambers on CMS. Each of the individual types of detectors and their positions in pseudorapidity can be seen.

There are a total of 1400 muon chambers used in the identification and measurement of muons: 250 drift tubes (DT), 540 cathode strip chambers (CSC), and 610 resistive plate chambers (RPC) as can be seen in Figure 2.20. The DT system is located outside the barrel region of CMS and the individual pieces consist of a tube filled with gas and a wire running through the center of it. Each DT chamber is composed of 12 aluminum layers, each with around 60 of such tubes. The wire running through the center of the tubes maintains a positively charged state. As such, when one of these very massive particles pass through the gas an electron is knocked off of the gas and is drawn to the charged wire. From this, CMS is able to determine the point at which the muon struck the DTs and obtains information about its positioning.

In the endcap region, we have CSCs who are responsible for detecting muons in a region with much higher particle rates. Similar in nature to DTs, they consist of a gas chamber with positively charged wires, but additionally have negatively charged wires crisscrossing the positive wires. This perpendicular design allows for more information to be obtained from each muon as the electrons knocked from the gas are attracted to one wire while simultaneously being repelled by the other. In each of the CSC modules, there are six layers which, when combined with information from the tracker, allows very

reliable tracks to be constructed and matched with the information from the outer muon chambers.

The final type of muon chamber is the RPCs, which can be found in both the barrel and endcap regions. These act as a sort of redundancy for the other two types of muon chambers, hence their being placed adjacent to both types of chambers. They are able to do this by acting as a trigger system to differentiate between actual muon hits and potential false alarms. RPCs are fast gas detectors that are composed of two parallel plates with opposite charges. These plates are made up of a highly resistive plastic material and have gas between them. In a similar fashion to those previously mentioned, when an electron hits this gas an electron is moved and then is attracted to one side of the detector. The main difference in construction, however, is that when a potential muon strikes, there is a deliberate delay where information from many of these detectors and those around it are used to verify the nature of the particle it detected. Similar to all of the detectors used in CMS, the muon chambers have an extremely fast response time on the order of 1 ns.

Chapter 3: Collider Theory

Contents

The goal of this chapter will be to translate the concepts and ideas from Chapter 1 and 2 and bring them into our physical reality. In the first chapter we were introduced to QCD and in the second we got a description of experimental methods. Now we shall introduce how these QCD concepts look in reality and how the most minute of details on the QCD scale can correspondingly lead to a drastic change in the macroscopic. In Section 3.1, we will talk about that translation from the QCD scale all the way up to our detectors. With knowledge of this path, it becomes easier to work in the opposite direction and use our macroscopic observations to learn more about QCD in later sections. Afterwards, in Section 3.2 we will discuss the CMS Triggering methodology and software that allow us to find data relevant to the physics we wish to study. Finally in Section 3.3 we shall present an introduction into Ultra-peripheral Collisions (UPCs) as well as cover previous pomeron physics studies as the language and terminology unique to these kinds of interactions are very important to this dissertation. With the culmination of this chapter, we shall then be able to move on to the physics analysis of this dissertation with a strong foundation and common understanding.

3.1 QCD Collider Phenomenology

While discussions of QCD in the abstract theoretical sense are useful, there is still the other half of the problem that needs to be addressed and that's how all this strange behavior such as asymptotic freedom and color confinement would translate into observables that we could measure. The realm of QCD is so far below our normal frame of reference that we need to use very particular pieces of machinery to even catch a glimpse of what's happening at that scale. To that end, we have particle colliders whose sole goal is to help us reach this most mysterious of realms. Therefore, the goal of this section to present how the behaviors of these particles can be translated from the extremely small QCD scale to trends on the larger scale where we can observe and work our way backwards [32]. This will be done by following along the path of a particle taken from collision all the way to the end states that we can observe in our detectors, as can be seen in Figure 3.1.

3.1.1 Coordinates

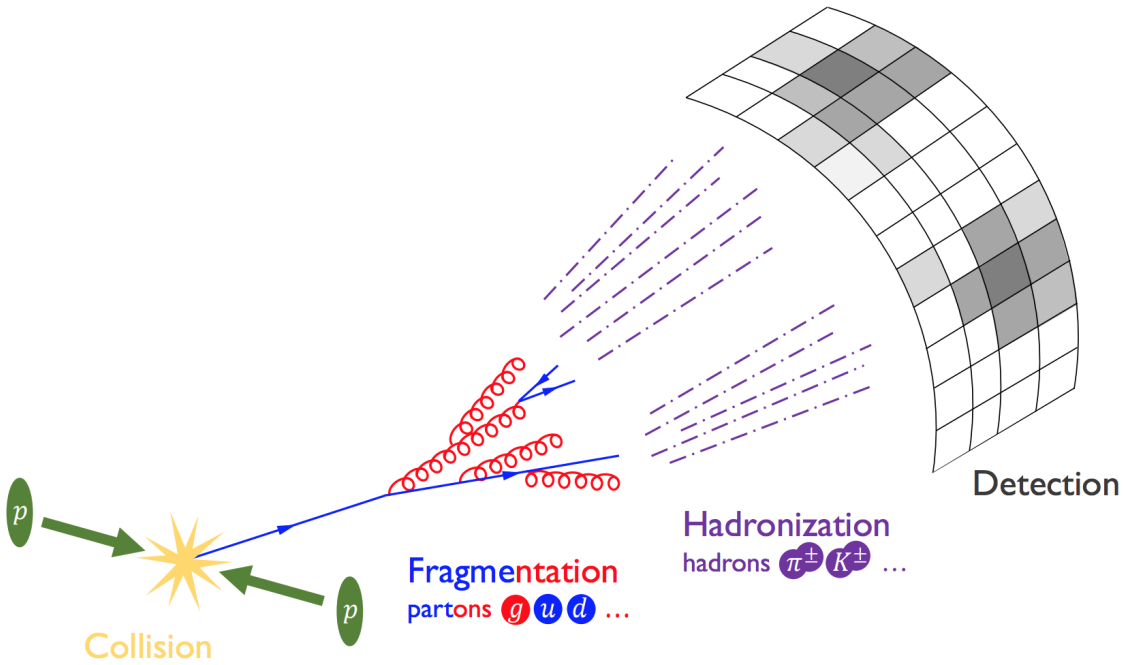

Figure 3.1: While QCD deals with the extremely small, there's a matter of translating the behaviors seen at those small scales up to the more macroscopic, and detectable, behaviors that we run into at particle colliders.

While the first step taken in a particle collision is, as one might think, the collision,

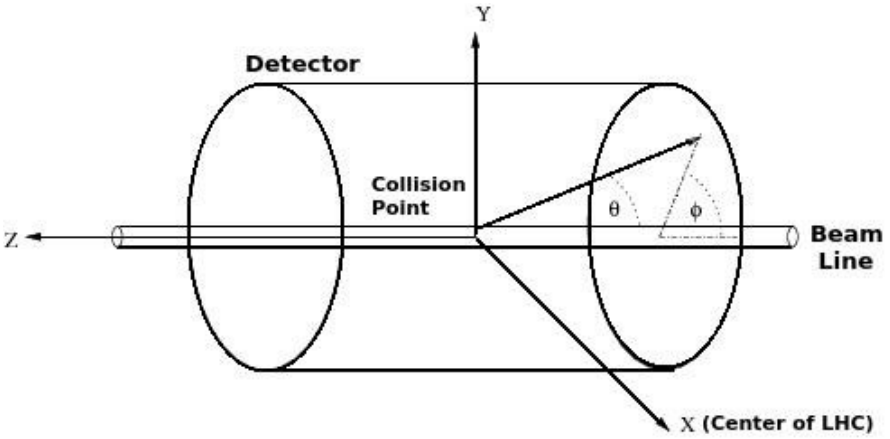

Figure 3.2: The coordinate system that will be used throughout this thesis. The primary axes are z, ϕ, and ∂ (or η, which is calculated from ∂ but isn't shown)

it would be beneficial to first discuss the framework upon which the collision occurs. An in depth discussion of the machinery used for the thesis was presented in Section 2.1, so we will not go too detailed, but a brief talk of the coordinate system the particle colliders typically utilize will be beneficial when talking of the path taken by particles after colliding. As seen in Figure 3.2, the traditional x, y, and z coordinate system aligns with x towards the center of the circular detector, y aligned upwards, and z along the beampath. That isn't, however, the typical coordinates used at the LHC. Typically, it is defined with the angle ∂ being defined along the z-y plane, with an angle of 0°meaning that the particle is traveling along the beamline. Another definition for the angle with respect to the beamline is η, or pseudorapidity, that is defined from ∂ in the following manner:

$$\eta = -ln\left(tan(\frac{\partial}{2})\right). \tag{3.1}$$

Pseudorapidity should not be confused with rapidity, which also can be used as a measure of a particles position with respect to the beam axis and transverse plane and can be calculated in the following way:

$$y = \frac{1}{2} ln\left(\frac{E + p_z}{E - p_z}\right), \tag{3.2}$$

where E is the energy of a particle and p_z is the momentum in the z-direction. While

a useful quantity, rapidity is a harder variable to measure for relativistic particles as it requires us to know the full momentum of the particle along the z-axis, which in reality can be a problem for particles that are very forward. Their physical positioning in space makes it harder to cover the region of phase space with a detector suitably radiation hard to measure particles for any reasonable length of time. Therefore, pseudorapidity is used instead. The reason pseudorapidity is "pseudo" is because of the fact that in the limit that $p_T \gg m$, the two quantities will converge. Additionally, it should be noted that differences in pseudorapidity are Lorentz invariant, while pseudorapidity itself is not.

Other variables of note when looking at positions of various particles in a particle detector is R, which is defined as the position of the particle in $\eta - \phi$ space, and p_T, which is the portion of a particle's momentum that is perpendicular to the beamline (also known as transverse momentum). These variables can be calculated in the following way:

$$p_T = \sqrt{p_x^2 + p_y^2}, \tag{3.3}$$

where p_x and p_y are the components of momentum in the x and y-direction, respectively. While R can be calculated as

$$R = \sqrt{\eta^2 + \phi^2}, \tag{3.4}$$

where η and ϕ are defined as above when discussing coordinates used in CMS.

Now that we have a groundwork to build upon, we can begin talking about how the effects from QCD can be seen in particle detectors.

3.1.2 From Collision to Detection

When talking about how the effects of QCD can be translated from the micro to the macro, one must start with some particles interacting. In high energy physics, this typically happens during a dedicated particle collision within some detector. There isn't

too much to be said for this step in the process, as it only encompasses the briefest instant in time before the next step begins. In more precise terms, the collision is the step when the interaction occurs between our interacting particles. For an example of the type of interaction one might see, we can look at Figure 3.3. In this example interaction, we have a lead ion that is "colliding" with a proton. We say it is "colliding" because the proton isn't exactly interacting directly with the constituents of the lead ion, but rather with an emitted photon. In a similar fashion, the proton is "colliding" via exchange that has vacuum quantum numbers, otherwise known as pomeron exchange [33]. Collisions such as this one are known as Ultra-peripheral collisions, and will be discussed further in Section 3.3 and similarly pomeron physics will be discussed in Section 3.3.2.

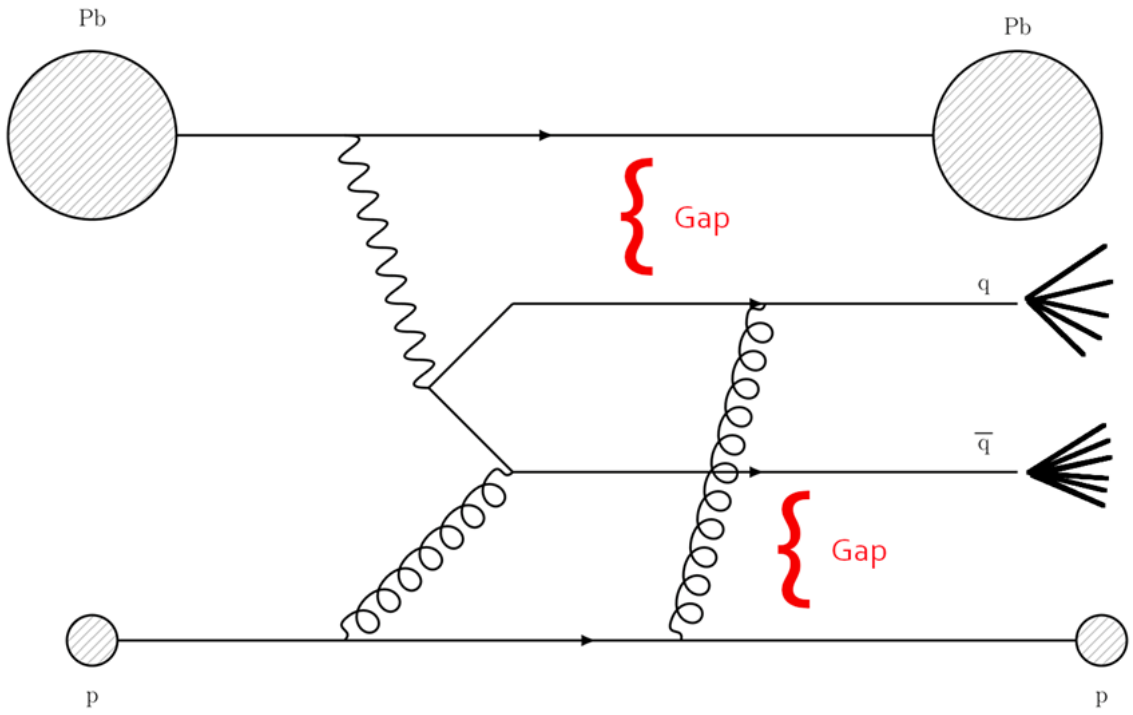

Figure 3.3: An example of the "collision" that can occur. We have interactions involving quarks and gluons and therefore this is the realm of QCD. The first step on the way to detection.

This interaction is simply one example of the sort that occurs millions of times per second at colliders like the LHC. At this point is when the math and predictive power of QCD can come into play. We have interactions between quarks and gluons, but now we must see how the transition from micro to macro happens.

While this all takes place within the detector, there still remains several steps before

the actual detection can occur. The next step after our initial interaction, or collision, occurs is fragmentation [34]. This step occurs in the instants after the collision when the outgoing particles from the interaction are no longer interacting. In contrast to the collision, fragmentation fosters a bit of chaos into the system by having the outgoing particles at this point begin to split and multiply. As quarks must remain confined, when these outgoing quarks get to a certain distance from each other, it becomes energetically favorable to create new quarks out of the vacuum to maintain that confinement. This process can be seen in Figure 3.4

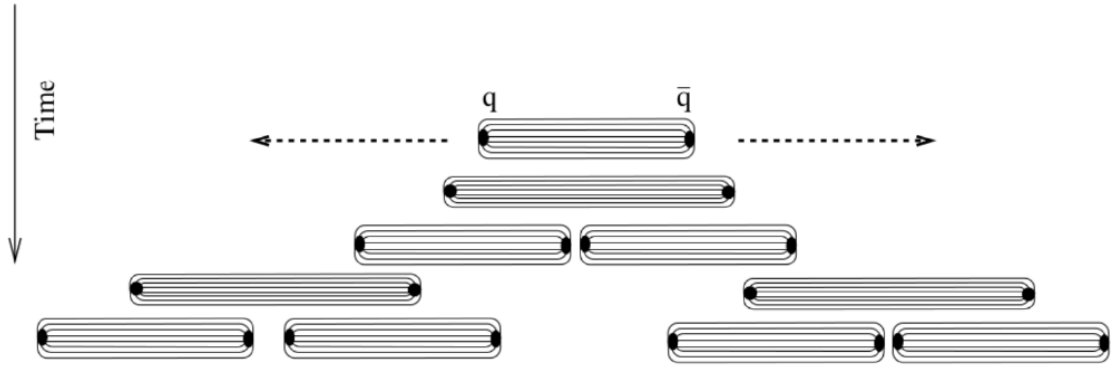

Figure 3.4: The processes of fragmentation and hadronization are oftentimes interlinked, so this represents both these processes as the initial quarks (represented as q) fragment off and end up creating new hadrons.

After fragmentation has occurred repeatedly, we will reach a state when the quarks no longer have sufficient energy to break apart any further. This is the process that happens after fragmentation and is known as hadronization [35]. At this point all the previously chaotic quarks will coalesce into bound states. Additionally, it's worth pointing out that this process of fragmentation and hadronization doesn't follow a set path. If we have two collisions that occur in the exact same way, the random gluon radiations that occur can lead to very different looking final states in terms of the actual particles present.

After an initial interaction occurs and we have some process where a quark is emitted, it can further muddy the system through what we call gluon radiation. A quark with sufficiently high energy can radiate gluons in a fashion similar to an electron emitting photons. Compared to photons, however, the gluon is an object that carries a color charge. Due to confinement, this gluon radiation that is carrying a color charge will

then also behave similarly to our initial quark, albeit at a lower energy. Therefore gluon radiation can end up making events much more eventful, in the sense that many low energy particle will be created in addition to the initial interaction.

Finally, we are at the point where the final stage of the process comes into play. This outgoing assortment of particles will then finally reach the detector itself. Since Chapter 2 was all about the detection process and our specific detector, the specifics of detection will be glossed over. For our purposes, whatever assortment of particles there are at the detector level will then interact with the detector and the "event" can be reconstructed.

However, the "event" we reconstruct isn't always the same as the initial collision. Gluon radiation and other random effects can causes drastic changes between the initial and final states. Thankfully, our detectors are the solution to this problem. While any one event is random, collections of events should have overall trends. Therefore, the detector's role and utility is allowing us to gather data and look at the overall trends. These trends can then be related to initial conditions before fragmentation and hadronization occurred. This will then allow us to get information about the collisions where the QCD was actually happening and we will have finally come full circle. From initial collision to the detector and back again, as physicists we are able to work with this kind of indirect observation in order to learn more about the fundamental nature of the universe.

3.2 CMS Data Triggering and Software

3.2.1 CMS Trigger

In the previous sections we covered both how the effects from QCD propagate up to a detector and how these very detectors work, but now we need to discuss how CMS is able to sift through the immense amounts of data that is coming in each and every second. At stable operating condition, the LHC is able to deliver bunch crossings every 25 nanoseconds, with each bunch crossing able to have up to 20 hadron collisions. This amounts to a potential 10^9 interactions happening every second, which is much more than our current technology can reliably process and keep. Therefore, a trigger

system is devised which allows us to parse down those 10^9 interactions down to the most interesting 10^2 events [36]. This is accomplished through the use of what are known as triggers whose primary goal is to act as an active filter that is able to snag events that have the potential to be interesting. There are several types of triggers used throughout CMS and they operate on a tiered system. Events which pass the first trigger are then passed on to the next, and often more discriminating, trigger.

At its most basic level, we have what are known as the Level 1 (L1) trigger. The goal of the L1 trigger is to simply pare down the sheer volume of data that is received every second down to a more manageable level. It accomplishes this by looking for the most basic principles of "interesting" events. Typically this is something as easy as the number of particles, extremely high energy particles, or just strange combinations of particles. The L1 trigger trims down the rate of information from a billion events per second down to 100,000 events per second. From there, we go on to our next set of triggers.

The next set of triggers are known as High Level Trigger (HLTs) and they typically correspond to more specific triggers [37]. These triggers are carefully designed to look at this still large amount of events and make a snap decision if it is an "interesting" event or not. The specifics of what an "interesting" event is depends on how the trigger is designed. This means that there are hundreds of different triggers used throughout CMS and each one is carefully designed to get specific types of physics in one collection. There exist very general triggers that get average collisions, but there are also highly specific triggers that might not go off nearly as often, but correspond to a much more rare physics event and allows study of things that would often get lost in the noise otherwise. From these triggers, collections of data that correspond to a specific purpose are gathered and then utilized by analyzers in order to conduct studies related to what the trigger was designed to select.

3.2.2 CMS Software

For the purposes of this section, we will be focusing more on the software that CMS uses for the reconstruction of the events after they are detected. While the detectors are

able to measure energies deposited and charges of particles, it is the role of the software to take these many blips and hits and compile them together into something that analysts are able to utilize. This is accomplished via what is known as the particle-flow (PF) algorithm [38]. From the copious amounts of data coming from the detectors, the PF algorithm will reconstruct the energy depositions, hits, and various data points gathered into more familiar physics shapes. The PF algorithm is able to identify certain particles via their characteristics.

For example, depending on which calorimeter energy is deposited, we can begin to identify the various particles. If a track has energy deposited into the ECAL, then it becomes an electron-candidate. While a track with energy deposited into HCAL would be considered a charged hadron candidate. Finally, a track with no associated calorimeter deposit would then be considered a muon candidate. This is the most simple example of the PF algorithm in action, but groups of criteria like this are what compose the PF algorithm and allow it to take the multitudes of blips to reconstruct and translate them into something ready for analysis.

Another aspect of the PF algorithm that will be instrumental for this analysis is the role of identifying jets. Jets are a narrow cone of various particles that are formed when a gluon is struck with sufficient energy to remove it from its previously bound state. This occurs in a manner similar to the process described in the previous section and can be seen back in Figure 3.4. The issue, however, is the disconnect between what happens in the initial state and what we see in our detector. From our point of view, we only see the particles in the end state and so the trick becomes being able to accurately group together and infer which of the chaotic swarm of particles originated from the same quark. Often there can be multiple jets in the same region of phasespace leaving your detector looking like a grand mess without any hopes to detangle your multiple jets.

The solution to this problem is yet another algorithm. This time, the algorithm is specifically designed to identify jet characteristics in order to group the particle similarly to how the PF algorithm worked. For this analysis, jets used were reconstructed using the anti-k_t jet reconstruction algorithm [39]. The anti-k_t algorithm identifies jets by looking

at several qualities between two particles. If we have two particles, x and y, we designate two qualities of d_{ij} and d_{iB}. The quality d_{ij} refers to the linear distance between these two particles, while d_{iB} refers to the distance from particle i to the beamline. If $d_{ij} < d_{iB}$ then particles i and j are recombined into a jet and then the process is repeated with the next nearest particle. This process continues with the jet growing and growing until we get to the situation where $d_{ij} > d_{iB}$. In this case, the jet is declared complete and is then removed from the listing of objects and the process can begin again.

The anti-k_t algorithm will continue in such a fashion until all the potential jet objects have been grouped together. It is a tool in the belt of the PF algorithm and instrumental in helping clean up the events and making them ready for analysis. With that, we end the journey of our initial collision as it worked its way from the interior of our detector, to detection, and finally translated into usable physics results for the good people of CMS. The remainder of this chapter will be dedicated to describing a certain subclass of physics interactions that is of particular importance for this analysis.

3.3 Overview of Ultra-peripheral Collisions and Pomerons at Particle Colliders

3.3.1 UPC Theory

Within the myriad collisions that occur at particle colliders, there are many different subclassifications of events. One such class of events that is very relevant to this thesis are ultra-peripheral collisions (UPCs) [40][41]. It might, however, be better to write it as "collisions," because in these types of events the particles do not directly collide. In these types of events, the particles themselves come extremely close, but never to the point where their radii directly overlap. Or, in more precise terms, these "collisions" occur when the electromagnetic fields of a particle interact with either the other particle's electromagnetic field or the particle itself. Typically, these occur with "near misses" where the distance at which they interact is just past the sum of the radii of interacting particles, but they can occur at longer distances with lower probabilities. These types of collisions

at the LHC allow the study of photon-mediated interactions at center of mass energies orders of magnitude higher than past colliders.

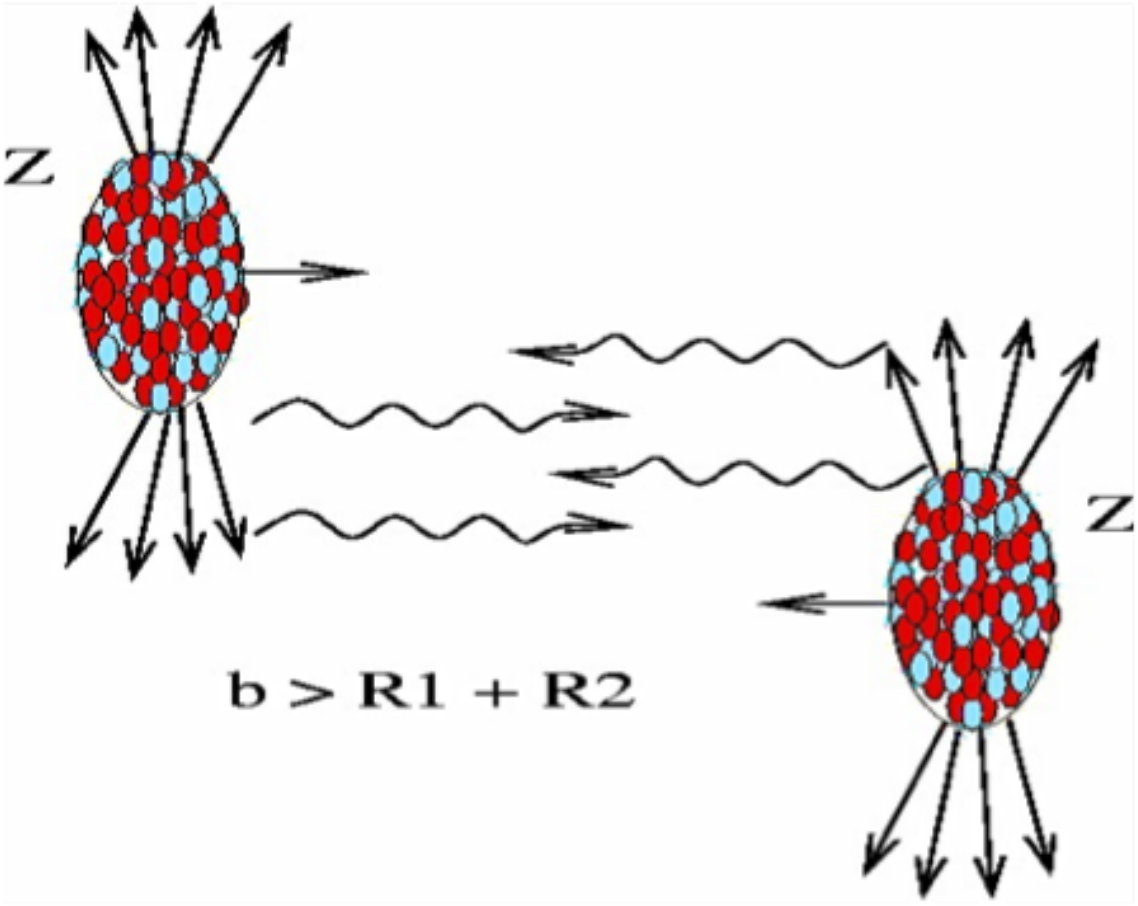

Figure 3.5: Example of two particles that are undergoing an ultra-peripheral collision. Their impact parameter (b) is greater than the sum of radii and therefore they are left to interact solely through their EM fields.

An example of UPCs can be seen in Figure 3.5 which shows two lead ions undergoing an ultra-peripheral collision. As any processes that occur in UPCs are typically electromagnetic in nature, they act as an excellent tool for studying those electromagnetic processes without hadronic contamination [42]. However, as will be seen in this analysis, UPCs can also be used for a different purpose. Photons mediate electromagnetic interactions and do not have any substructure. This combination of properties makes them perfectly suited as a probe to study other hadronic processes if one can find the right kind of UPC.

3.3.2 The Pomeron in Particle Colliders

As mentioned in the conclusion of Section 1.4, the advent of modern particle colliders allowed new probes to be made into the structure of the pomeron itself. In this section, we will be presenting one such probe which represents the culmination of the efforts of a previous particle collider at a much lower energy. This measurement was of diffractive photoproduced dijets in ep collisions at The Hadron-Electron Ring Accelerator (HERA) [43]. HERA was an electron-proton collider ring that was in operation from 1991 to 2007 at Deutsches Elektronen-Synchrotron (DESY) laboratory in Hamburg, Germany. Both electrons and positrons were accelerated up to 27.5 GeV and collided with protons of up to 920 GeV. These types of collisions were instrumental in probing various aspects of QCD and cross section measurement and a display of what an event might look like can be seen in Figure 3.6.

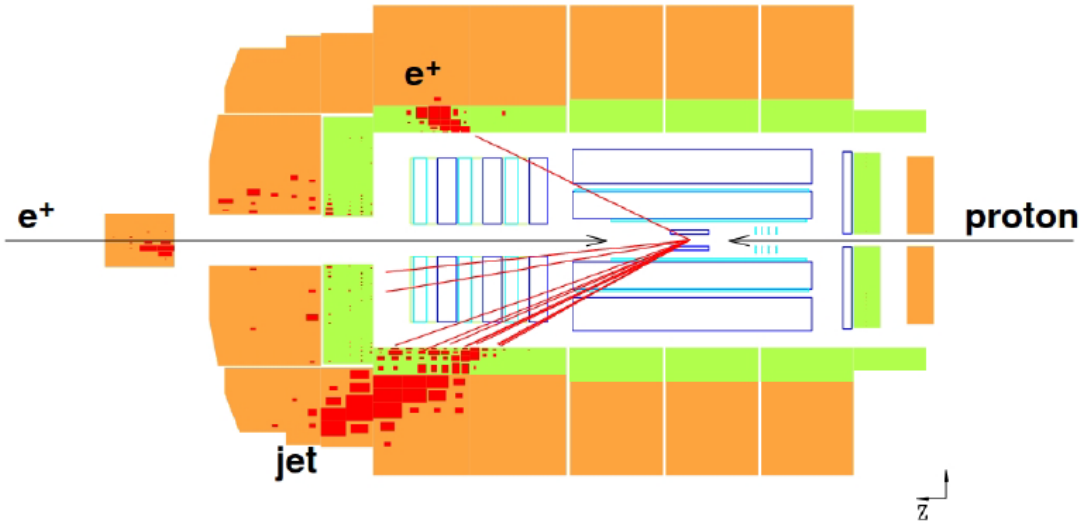

Figure 3.6: Example of the types of collisions that could be seen at HERA. A positron is scattered by the protons which results in the proton fragmenting and giving us a jet in the forward region in the final state.

For our purposes, however, we will be focusing in on a particular study conducted by H1, which is a particle detector located at HERA. HERA collided electrons or positrons with protons at energies up to 318 GeV. Diffractive processes, which had the form ep $\rightarrow$ eXY, were conducted and studied extensively at HERA [44]. In these kinds of processes, the interacting hadron can either stay intact, or dissociate via an exchange which has

vacuum quantum numbers, which we now know as pomeron exchange.

As mentioned previously, the question of what exactly a pomeron is still eludes us. We can define it as the Regge trajectory that allows a more complete description of experimental data, but that still falls short of a full description. It remains an overwhelmingly mysterious object that we can use to describe the physics that happens to a certain degree, but it still has a quark and gluon structure that can be probed with modern technology. Therefore, measurements such as the ones conducted at HERA represent an important piece of the puzzle to discovering more about this mysterious structure. By puzzling out what its made of, we are able to become one step closer to giving a full description better than simply a Regge trajectory. Since it maintains so much mystery, it becomes even more relevant to have as many measurements at as many different colliders and energies as possible. The fact of the matter remains that our understanding of it is so lacking at the moment, that it's entirely possible that the "pomeron" we are talking about for these experiments at HERA isn't the same "pomeron" as we use when talking about physics at the LHC.

The study of note conducted at HERA is one examining diffractive photoproduced dijets, which the discerning reader will recognize as the subject matter of this dissertation. The primary observables of note for this analysis at HERA are

$$x_\gamma = \frac{\sum_{i\in jets}(E_i - P_{z,i})}{\sum_{i\in X}(E_i - P_{z,i})} \tag{3.5}$$

and

$$z_{IP} = \frac{\sum_{i\in jets}(E_i + P_{z,i})}{\sum_{i\in X}(E_i + P_{z,i})}, \tag{3.6}$$

where z_{IP} is the momentum fraction of the parton relative to the pomeron and x_γ is the momentum fraction of the parton relative to the lead ion. The top sum in these variables runs over all the jets in the event, while the bottom sum is over all of the hadronic final

state particles that were detected. E_i is the ith particle's or jet's energy and $P_{z,i}$ is the ith particle's or jet's momentum in the z-direction. These observables allow us to probe the quark and gluon content of the pomeron. Theorists are able to utilize distributions from experimentalists in order to refine their data. However, before this dissertation, the analysis presented in this section represented one of the last times such information was measured.

In this analysis at HERA, the photon is emitted from the positron which is then scattered and left undetected. The photon then goes on to interact with the proton via pomeron exchange, as can be seen in Figure 3.7. Interactions such as this one are vital for gaining an understanding of the pomeron and its behavior. The interaction between the photon and the pomeron allow us to utilize the photon as a probe into the structure and general behavior of the pomeron. Since the photon does not have any substructure, it acts as an ideal probe for situations such as this one. The results and findings of this study conducted by H1 can be seen in Figure 3.8 along with the comparison to theoretical models. Theoretical models overestimated the measured total cross sections for these processes, which confirms finding of an earlier study done by H1. Overall, however, it appeared that the theoretical models had excellent predictive power and were able to describe the shape of the distributions within uncertainty.

As mentioned earlier, results such as these ones allow us to gain a greater understanding of what exactly the pomeron is. We know it is vital for explaining our experimental data, however what exactly the pomeron is remains unknown to us. Questions as basic as "are all pomerons the same," or the more important question of "why do our normal calculations fail to explain this," elude us to this day and so by examining the behavior of pomerons at each energy available to us, we can begin to break apart these mysteries. One of the best ways we are able to answer these questions is by repeating measurements such as this one at the highest energies. In the modern day, we can reach center of mass energies an order of magnitude higher than studies conducted at H1 which will allow us to analyze the behavior of the pomeron over a wide range of energies. These kinds of in depth studies into the pomeron is what is needed to finally illuminate this most myste-

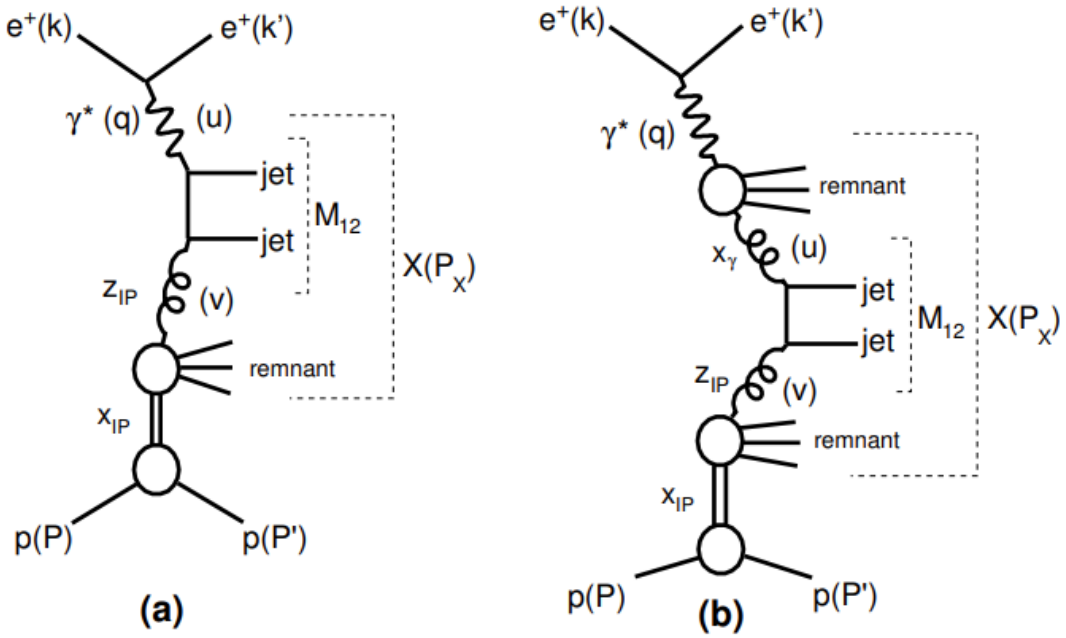

Figure 3.7: Leading order diagrams of the direct a) and resolved b) diffractive dijet production. Figure extracted from [43].

rious of objects. However, studies of this nature have not been conducted at the LHC, which represents a significant gap in our data and that is one that this dissertation seeks to fill. As such, in Chapter 5 we present an analysis looking at the same variables looked at HERA, but this time at the LHC. The characterization of these variables, namely z_{IP} and x_γ, over these wide ranges of energies allow us gain information about the structure of the pomeron at the highest energies we've ever been able to reach.

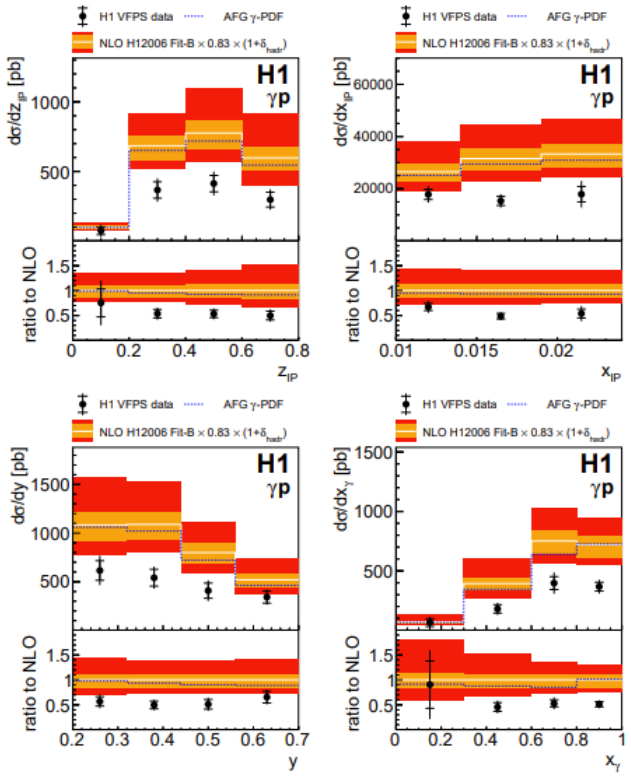

Figure 3.8: Diffractive dijet ep cross sections in the photoproduction kinematic range differential in z_{IP}, x_{IP}, y, and x_γ. The white line represents the theoretical predictions and a ratio between data to simulation can be seen below each plot. Figure extracted from [43].

Chapter 4: Monte Carlo Contact

Contents

This chapter will discuss some of the service work conducted at CMS as part of this author's PhD program. The Monte Carlo (MC) approach is a very important aspect of physics knowledge and understanding. It represents a bridge between the theoretical and experimental sides of physics by allowing direct comparisons between theorists' predictions and empirical data. Experimental results, such as the ones presented in this dissertation, can be used by theorists to refine their theories, which can then in turn be implemented in MC programs to get physical predictions. These predictions can then be compared to data and the cycle can continue on. As CMS is an extremely large collaboration with over 4000 physicists currently part of it, it isn't feasible for each and every member of the collaboration to produce their own MC for experimental comparison. Therefore, there are experts appointed known as Monte Carlo Contacts who handle the brunt of the work needed to produce the myriad types of MC that are needed every day by the collaboration. In Section 4.1, we will discuss the general process of MC production in CMS and why it is such a lengthy process. In Section 4.2, the specific work done as part of this PhD program will be outlined. While the MC work done by the author does not directly correlate to any specific analysis, the work done to produce it has indirectly lent a hand to almost every analysis that was conducted while the author was a MC contact.

4.1 Monte Carlo at CMS

The role of simulation in modern day physics is incalculable. It's the manner in which the predictions and models of the theorists are translated into the physical realm to be

studied by experimentalists. The interplay between theorists and experimentalists is one of the most powerful driving forces to modern physics as predictions are put to the test at particle colliders. Results gained through experimentation then go to influence the theorists and the whole process can begin anew.

Put simply, MC is computer-generated physics events. It it somewhat of a testing grounds where we put our knowledge of the basic physics to the test. Our understanding of how particles interact is input as the basis of the code and then the simulations output what reality would look like, given our understanding of it. Therefore, it can be completely disconnected from our empirical data and allow direct comparisons between theory and reality. If the simulations of reality line up with reality perfectly, then we could have evidence of the depth of our understanding. However, in many cases reality and the simulations do not line up which indicates flaws in our understanding that need correcting. With this knowledge in hand, theorists can refine their theories which leads to a furthering of the field as a whole.

This is only possible due to the power of simulation and gives MC techniques one of the most prominent roles in modern physics. The ability to have predictive power is what makes a science something other than a display in mathematics. However, this is often not a simple endeavor as all these experiments take place in real machinery with real physical limitations and issues [45]. By issues, it is not meant problems within the detectors themselves, but rather specific quirks and unique aspects individual to each detector that change the reality that is seen in it. Often, the distribution that is obtained within a detector is subject to biases that influences the distribution and sometimes makes it unrecognizable when compared to the "true" distribution at the theoretical QCD level [46].

This illustrates one of the many important aspects of MC at an experiment like CMS. The influence of our incredibly complicated and large machine can lead to detector effects that need to be unraveled from the physics in order to make direct comparisons between experiments. Disentangling detector effects from the detector measurements is known as unfolding, because one takes the distribution from our detector and then "unfolds"

it to show the true fundamental distribution. This process, however, requires an intimate knowledge of the detector and how its myriad quirks will influence each and every fundamental physics quality. Luckily, we have MC where there are dedicated teams of experts whose main goal is to ensure that the productions are ready to be compared with empirical data.

As noted before, CMS is an extremely large collaboration with over 4000 individuals working to ensure function of our detector while simultaneously working on their own physics analyses. While not every physicist that is a member of CMS currently has an ongoing analysis, more often than not there is something they are actively working on. In almost all cases, any kind of analysis will require some MC in order to provide predictions, corrections, or acceptance. An average period of MC production in CMS can be seen in Figure 4.1. At any given time, there are many analyses or studies ongoing by the many members of CMS and almost all of them have a need for MC. Each and every one of these analyses relies upon accurate simulation and fast production in order to keep the scientific beast of CMS rolling along.

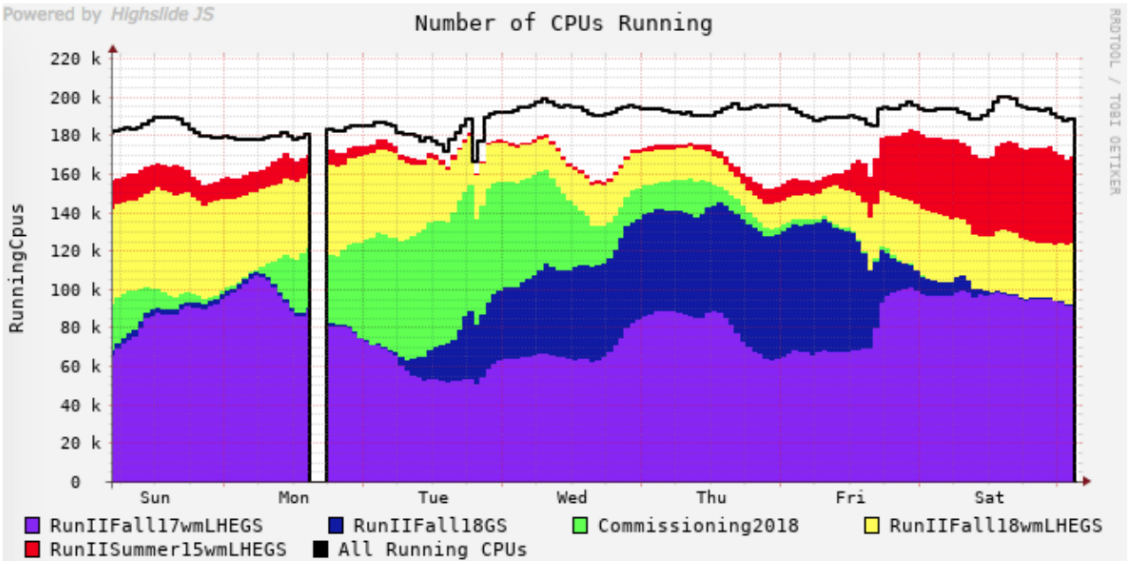

Figure 4.1: A graph representing the computing power that is solely dedicated at CMS to production of MC for the many analyses currently ongoing. Each of the different colors represents a different "campaign" which relates to a certain period of time of machine operation.

However, with a machine as complicated as CMS, it is unfeasible for each member of the collaboration to produce and, most importantly, understand the detector and how to

simulate its effects in order to accurately make predictions [47]. Therefore, the solution to the need for MC coupled with its difficulty in production lead to the creation of a dedicated MC expert. These experts are tasked with the charge of being responsible for the production of MC within their specific subgroup. The number of MC contacts for a specific subgroup depends on the number of members, but regardless of size the need for MC is always pressing. While this chapter will be a brief one, as much of the work was done in formats not readily presentable, it represents a significant effort of learning and work on the author's part and is worth cataloging for this thesis.

4.2 Monte Carlo Contact

This section's goal is to attempt to illustrate the work done by the author as part of their service work for the purposes of this PhD. As mentioned above, a MC Contact is someone who is responsible for the production of MC for an entire subgroup. Since the author was working in heavy-ion collisions, it was natural for the author's subgroup they were in charge of to also be heavy-ions (HIN) The issue, however, lies in the fact that this role was one of the few spots in CMS where the work doesn't comprise some form of data analysis. Much of the work was done in testing, producing, and troubleshooting the many kinds of MC that was needed by the HIN subgroup and so does not lend itself to a flashy chapter where one is able to outline and quantify the effort put forth. Therefore, it is hoped that the reader will be able to understand that in this case the chapter length isn't proportional to the work done.

MC work done by a contact can be broken down into 4 separate elements. These elements and a summary of the work and process by which a MC contact operates can be seen in Figure 4.2. These are privately produced MC, officially produced MC, testing/troubleshooting general MC productions, and finally cataloging the MC produced for the entire HIN group. To begin with, we will discuss the privately produced MC. In terms of MC production, the two sides of the coin are privately produced and officially produced. Often, the two are functionally the same in terms of content, but official MC is sanctioned by additional contacts associated with MC production who ensure that it is properly

produced. However, they are distinct and so bear distinct treatment and discussion.

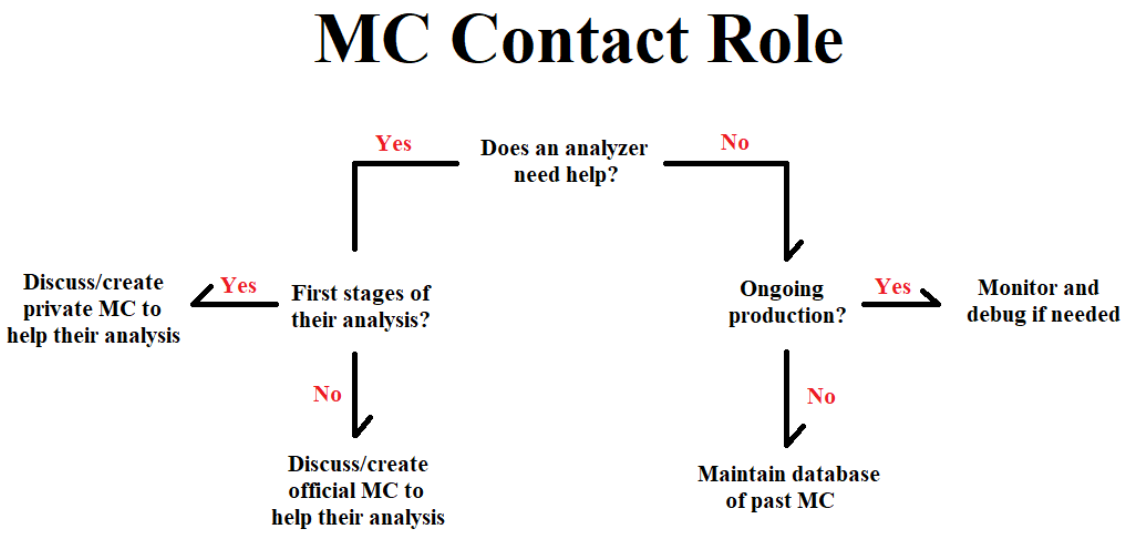

Figure 4.2: Overview of the duties of a MC contact. The needs of the heavy ions group dictated how much of the effort on the part of the MC contact was in advising versus actual MC production.

Private MC typically encompasses productions before one is at the final stages of an analysis, or when one needs to test out new parameters for simulation. These sort of productions can be made with many different MC generators (such as Pythia6, Pythia8, HIJING, EPOS, HYDJET, STARlight, etc.). The reason for having so many different generators is due to the fact that we often specialize in what we wish to study and generators typically have some types of processes they specialize in. For example, HIJING is a generator that specializes in heavy-ion collisions, however it isn't as good for more general studies of proton-proton collisions and so that's why we have a generator like Pythia8. Therefore, a wide breadth of knowledge of the different generators is needed as different analyzers will have different physics they wish to study. In these cases, the role of the MC contact was not only to produce the needed MC at the most basic generator level, but then to simulate additional effects as needed. One of the more common cases for private production was in trigger development, see Section 3.2.2, where one needed to be able to make snap decisions on the physics content of an event without the luxury of full reconstruction. By producing MC that simulated the raw output from a detector, trigger experts are able to refine their definitions in order to ensure that we maximize the amount of data obtained that is relevant to the studies we wish to conduct. This is just one of the

cases for which private MC is utilized, but it represents the most far reaching effects of one of the privately produced files.

The more common type of MC request that one has to field is an official MC request. Similarly to private requests, these can be with any number of MC generators and it was the role of the contact to be able to handle any of these requests, or quickly figure out how to handle a new one. MC samples were typically produced at the behest of fellow CMS analyzers. These analyzers would be conducting a study and would need MC that accurately described the effects of the CMS detector in order to have direct comparison with theory. The process for producing these kinds of samples involved much oversight, as this was one of the more crucial portions of a study at CMS, and so we had to be sure that everything was in order. This led to the final task that was undertaken by MC contacts, troubleshooting.

Oftentimes a request from an analyzer would not be a straightforward affair. The role of the MC contact was to produce MC, but a more important role was to make MC that made sense. This meant that we often could not take an analyzer's word on the production and its various properties. In order to ensure everything was correct, we would go and create a small sample ourselves in order to test and see how the MC performed before it was officially introduced into the system. This meant an intimate familiarity with all the different generators was required because one never knew what the next kind of production would look like.

The final role of a MC contact was maintaining and adding to the collection of MC produced by oneself and all previous MC contacts for a specific subgroup. This task wasn't particularly arduous, but maintaining and upkeeping the records of MC production in HIN represented a fairly significant commitment of time on the contact's part. The history of MC production is instrumental for anyone conducting an analysis, as often the processes one wants have already been requested. Therefore maintaining an accurate and clean record of the MC produced, as in Figure 4.4, was one of the main tasks undertaken by the author.

Available Samples

Generator	Evt Type	# Evts	Content	DataSet	T2 copies	More Info	Notes
Minimum Bias							
Hydjet	Min Bias Drum5F	942K	AODSIM	MinBias_Hydjet_Drum5F	MIT	McM	RAW
EPOS	Min Bias	96K	AODSIM	Min Bias ReggeGribovPartonMC	MIT	McM	RAW
AMPT	Min Bias NoStringMelting	96K	AODSIM	Min Bias NoStringMelting	MIT	McM	RAW
AMPT	Min Bias StringMelting	10K	AODSIM	Min Bias StringMelting	MIT	McM	[1]
Unembedded							
Pythia8	QCDPhoton_pThat-15	973K	AODSIM	QCDPhoton_pThat-15	MIT	McM	RAW
Pythia8	QCDPhoton_pThat-30	928K	AODSIM	QCDPhoton_pThat-30	MIT	McM	RAW
Pythia8	QCDPhoton_pThat-50	981K	AODSIM	QCDPhoton_pThat-50	MIT	McM	RAW
Pythia8	QCDPhoton_pThat-80	1120K	AODSIM	QCDPhoton_pThat-80	MIT	McM	RAW
Pythia8	QCDPhoton_pThat-120	1059K	AODSIM	QCDPhoton_pThat-120	MIT	McM	RAW
Pythia8	QCDPhoton_pThat-170	943K	AODSIM	QCDPhoton_pThat-170	MIT	McM	RAW
Pythia8	QCDPhoton_pThat-15_Filter30	889K	AODSIM	QCDPhoton_pThat-15_Filter30	MIT	McM	RAW
Pythia8	QCDPhoton_pThat-30_Filter30	841K	AODSIM	QCDPhoton_pThat-30_Filter30	MIT	McM	RAW
Pythia8	QCDPhoton_pThat-50_Filter30	883K	AODSIM	QCDPhoton_pThat-50_Filter30	MIT	McM	RAW
Pythia8	QCDPhoton_pThat-80_Filter30	929K	AODSIM	QCDPhoton_pThat-80_Filter30	MIT	McM	RAW
Pythia8	QCDPhoton_pThat-120_Filter30	1149K	AODSIM	QCDPhoton_pThat-120_Filter30	MIT	McM	RAW
Pythia8	QCDPhoton_pThat-170_Filter30	1035K	AODSIM	QCDPhoton_pThat-170_Filter30	MIT	McM	RAW

Figure 4.3: A small sliver of the total MC records that were produced and documented by the author during their time as MC contact for HIN.

4.2.1 An Example Effort

In order to illustrate the process of MC production, we will use an example that encompasses many of the different elements that needs to be undertaken by a MC contact. Many of the individual elements in this example needed to be done regularly, but this is a unique situation where all these different potential tasks as a MC contact needed to be done for one request. In order to provide a good basis for explaining the individual elements, we will be referring to Figure 4.4 throughout this section which outlines the overall task of MC production.

We were contacted by a new analyzer to CMS who was early on in conducting a study of the following process.

$$B_c^+ \rightarrow J/\psi\pi^+. \tag{4.1}$$

To study this process, they would like to request a MC sample corresponding to this process as well as simulation of the background. As discussed previously, when particles

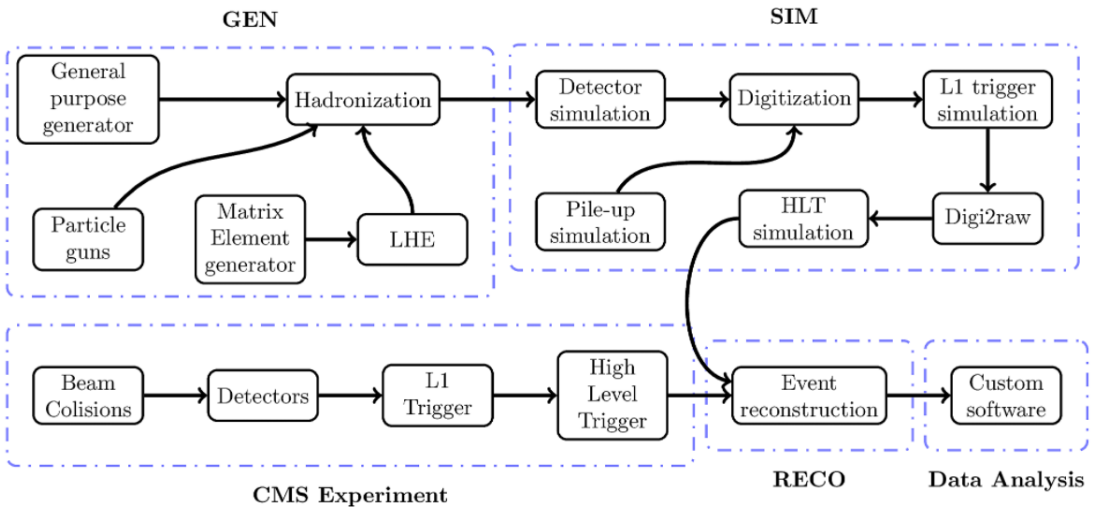

Figure 4.4: An overview of the process for MC production at CMS. There are 3 main sections in production and those are GEN, SIM, and RECO. At the RECO stage the MC simulation should look identical to empirical data. Each is comprised of many different elements that are all necessary for full event simulation. Under the CMS Experiment section we can see the way in which data is collected which is then compared with MC.

are colliding it often is not a purely clean event. There are many processes happening in the background such as secondary collisions or even processes that mimic the final state behavior of the process you want to study and so proper simulation of those types of background interactions are key for accurate comparison with empirical data.

For their MC, the analyzer wished to use a new (to the MC contact) generator named BCVEGPY2.2. When an analysis is in the early stages, we often wish to do cross checks privately before submitting an official request as often there are tiny mistakes or bugs that need to be ironed out before entering the system officially. As contact, my job was to attempt to produce a small MC sample using BCVEGPY2.2 and then propagate it through each process in turn. The processes that were simulated can be seen in the above references Figure 4.4. This necessitated learning a new MC generator which, as is often the case, wasn't a simple task. Most of the work at this point was spent learning how to run BCVEGPY2.2. This finished, this process and generator could then be approved to run officially in CMS once fully simulated from GEN to RECO.

The next step in producing this officially was another technical step. MC production is done in "campaigns" at CMS which indicate what types of particles, what energies, and in what year you wish to simulate. In this analysis' case, they wished to do proton-proton

collisions at 5 TeV under the conditions present in the winter of 2017. However, since they wished to use a MC generator that wasn't native to the CMS software, we had to create what is called a pLHE campaign. The purposes of a pLHE campaign are to allow a bridging between nonnative MC generators and the official winter 2017 proton-proton campaign. As it was the first requested simulation of this kind, a pLHE campaign had to be created. This wasn't a MC contact task, but we provided much of the information utilized in the creation and testing of this new campaign.

Once the campaign was complete, the process could then be submitted officially into the system. In normal circumstances, this was the end of most of the work on the MC contact's part. We would monitor the production, but in the large majority of cases nothing goes awry. However, in this case we had problems arise. Some of the specific quirks of BCVEGPY2.2, namely how it output certain variables such as energy and momentum, were causing errors in the system that weren't detectable by our private simulations. The reason this was not detected by our private simulations was because we could produce the events directly, but the official MC required already generated events and this discrepancy caused errors.

At this point, our task was to identify the error and fix the incompatibility. This necessitated much more testing and working with the analyzer in order to isolate the problem and then get things running again. Once this was complete, the processes requested by the analyzer were able to continue on and finish production. Finally, the last task was to document the task for any future analyzers who might benefit from this MC sample.

It is worth noting that this task was simply one of many that were constantly coming in. Often many requests needed to be juggled in parallel and so many tasks such as these were constantly being undertaken at a time. While the efforts of a MC contact oftentimes aren't glamorous, they represent an important effort for the giant beast of analysis that is CMS. With over 4000 individuals collaborating within CMS, there is constantly a need for MC production. Almost all analyses undertaken during the author's tenure as a MC contact required some form of production that the author then produced. This encompasses

many different physics results over the course of the last years that were contingent upon proper simulation of basic physics interactions as well as reproduction of all the individual detector effects. As MC is the bridge between reality and theory, these efforts cannot be dismissed and without MC, our current understanding of the world would surely suffer as a result.

Chapter 5: Analysis of Diffractive Dijet Photoproduced Events at 8.16 TeV in pPb

Contents

In this chapter, we describe the main measurement that was made for this dissertation, namely the measurement of diffractively photoproduced dijets for the first time at the Large Hadron Collider. In Section 5.1, we will present the motivations for this measurement as well as provide some context for these events at past detectors. Then, in Section 5.2 we shall discuss the dataset used for this analysis. Afterwards, in Section 5.3 we will begin looking at the data collected by examining the jets measured. Next, in Section 5.4 we will take the next step by looking at how best to identify events that contain gaps within them. Finally, in Section 5.5 we will present for the first time at the LHC a measurement of Z_{IP} and x_γ in diffractive photoproduced dijets.

5.1 Motivation

Before we get into meat of the data analysis, it's important to maintain a perspective of why we are doing this measurement and present specific context for this type of measurement. The subject matter of this dissertation is looking at photoproduced diffractive dijets in proton-lead collisions [48]. The sort of processes that can be seen in such events look like:

$$pPb \rightarrow XPb, \tag{5.1}$$

where X can be any number of processes. For this dissertation, we will be focusing on events where X is a dijet system which we can see in the final state. These types of events have been extensively studied at the electron-proton collider HERA, but there remains a sizable gap at the LHC for similar measurements [49]. In diffractive processes such as these, the interacting hadron can dissociate via an exchange that has vacuum quantum numbers, otherwise known as a pomeron (IP) [50]. Although these types of processes are very common at colliders, direct probes into the pomeron itself often prove challenging. In response to this critical gap in our understanding, we propose one such probe into the behavior of the pomeron in this dissertation.

A more illustrative example can be seen in Figure 5.1, where a leading order representation of the types of events this dissertation focuses on can be seen. In this example, the lead ion will emit a photon while the proton will emit a pomeron, which at leading order can be represented as an exchange of two gluons. These two particles will interact and leave us with dijets in the final state and a gap on either side. While we won't be able to see every aspect of the final state, such as what happens to the protons and lead ions, if we make some clever choices in kinematic cuts, we can be extremely confident that we are seeing the events we wish to study.

An important factor to discuss when talking of the motivations for a measurement is what kind of collisions one wants to utilize. At the LHC, there are a number of different types of particles that are collided such as protons, lead ions, and even some more atypical particles such as xenon. Therefore, one must take great care when considering the types of collisions along with the amount of data available to make their measurement. For this analysis, we will be using the proton-lead dataset that was collected by CMS in 2016 at $\sqrt{S_{NN}}$(center of mass energy) =8.16 TeV.

Collisions between protons and lead ions are uniquely suited for a measurement such as this one. As mentioned above, the specific type of event we wish to find are events

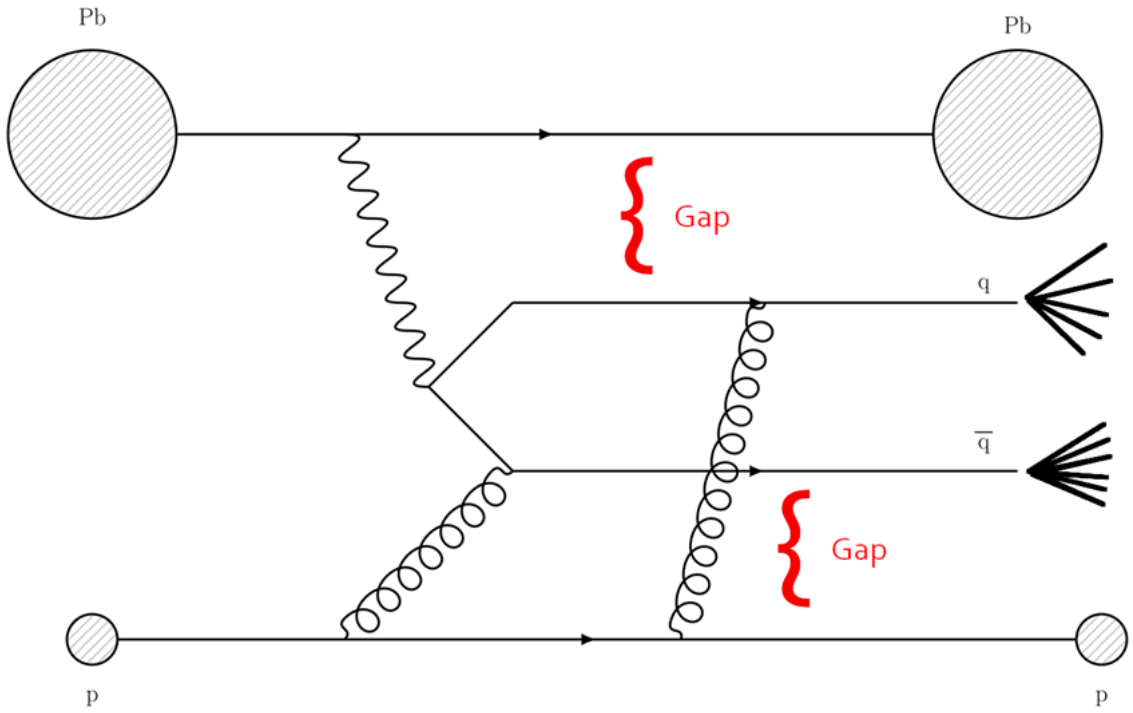

Figure 5.1: A leading order representation of the types of events that we are hoping to observe. In the initial state, we have a lead ion that emits a photon and a proton that interacts via pomeron exchange. These particles interact, and in the final state we have two central jets and a rapidity gap on both forward regions of the detector.

where the lead ion emits a quasi-real photon that subsequently fluctuates into a quark-antiquark pair and the proton emits a pomeron. These two particles will interact, leaving us with two central jets in the final state. However, as observers we are not privy to the intermediate steps along the path from collision to the final state. All we are able to know is that we have beams of protons and lead ions circulating and that sometimes we end up with two jets in the final state. Jets are some of the most common objects at the LHC and so it becomes vitally important to ensure that the physics we see corresponds to the initial states we wish to study. Therefore, we exploit a property of protons and lead ions in order to make sure that when we see certain signs, they correspond to the processes which we wish to study.

The property we are exploiting is that of the lead ion's propensity to emit photons. As the ion is accelerated to velocities near the speed of light, it will undergo a Lorentz contraction, and, since lead ions are highly charged particles, their electric field will also be contracted. This contraction of the particle and its electric fields, as can be seen in Figure 5.2, causes an enhancement of the photon flux equal to the charge of the particle

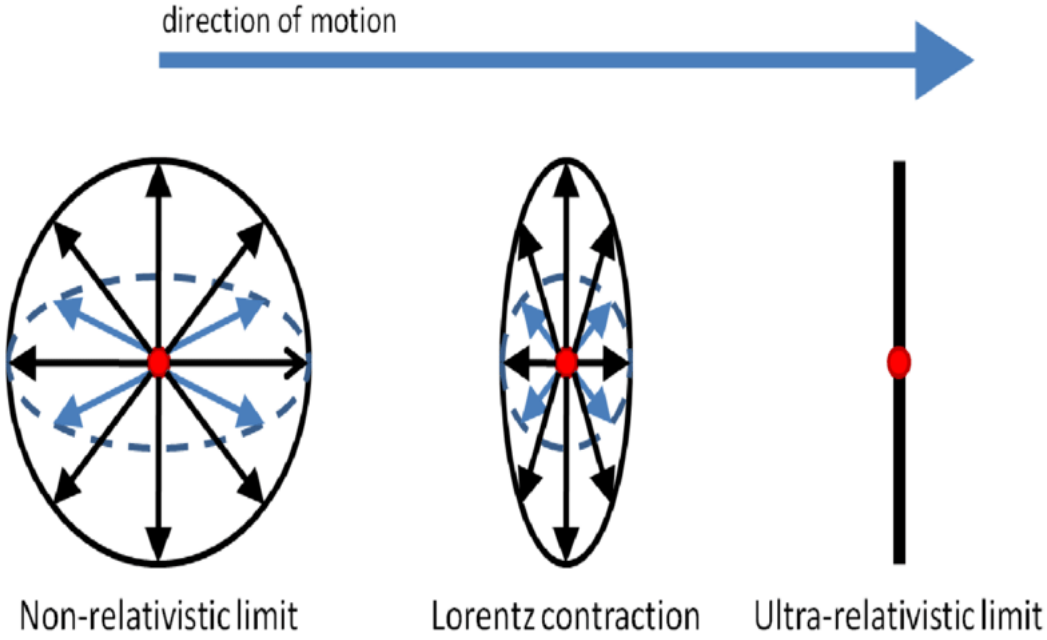

Figure 5.2: As lead ions are highly charged non pointlike particles, when they are accelerated they undergo a Lorentz contraction which cause them to look pancake-like. This effect also compresses the electric field thereby enhancing the photon flux by a factor of Q^2 (Q = 82 for lead).

squared. Lead ions have a charge of +82, which amounts to an enhancement of 6,724 when compared to a proton, as can be seen in Figure 5.3. As mentioned above, both pomeron emission and photon emission have gaps in the final state as a signature. This, combined with the enhancement of the photon flux, means that if we have a gap in both sides in the final state when looking at proton-lead collisions, we can be certain of the initial states that we are not normally privy to.

Since the lead ion is so much more likely to emit photons, if we see a gap in the final state on the lead side then we can be extremely certain that it's due to photon emission. Conversely, if there's a gap in the final state on the proton side, we can be extremely certain it's due to pomeron emission as protons are much more likely to emit pomerons than photons. That's not to say that we can't have the reverse happening where a lead ion emits a pomeron and a proton emits a photon, but we can minimize the chance of this by exploiting these facts. Monte Carlo studies will allow us to quantify the chances this happen and calculate the uncertainties it will provide, but based on these properties we can assume any effect will be minimal. By conducting this measurement in proton-lead

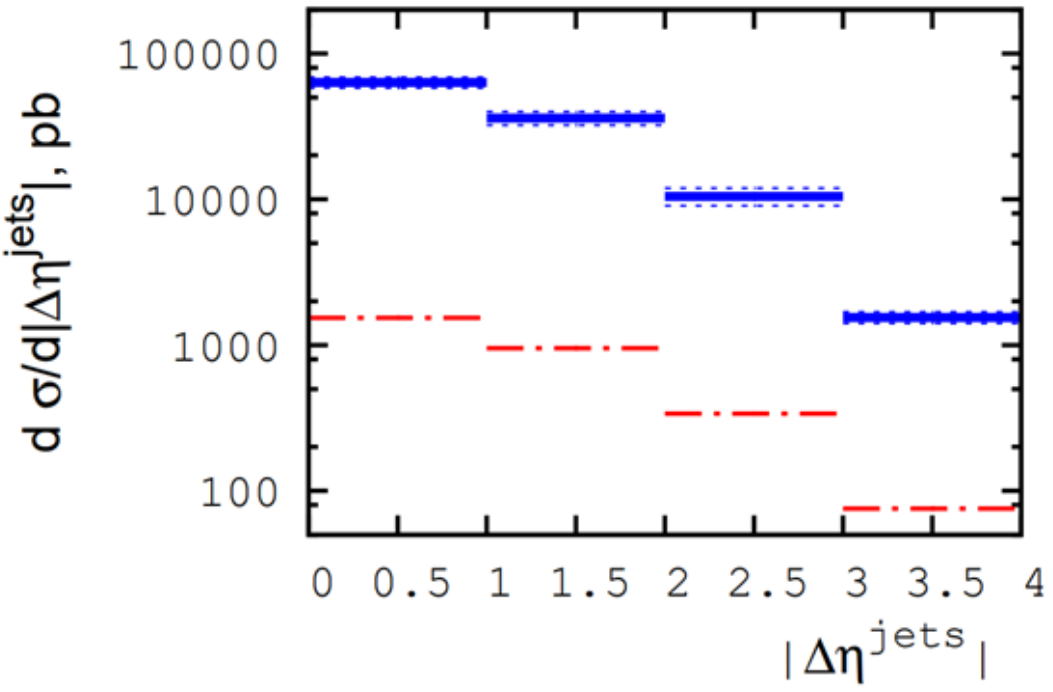

Figure 5.3: The differential cross section for diffractive photoproduction of dijets with the different contributions split into two sets. The blue line represents contribution to the cross section where the photon is emitted from the lead ion, while the red dotted line represents the contribution where the photon is emitted from the proton. This large difference is due to the lead ions extremely large photon flux. Figure extracted from Ref. [51]

collisions we are uniquely situated to see the exact events we are hoping to study while simultaneously minimizing the chances of lookalike events sneaking past our notice.

The pomeron remains one of the more nebulous physics objects, and so measurements such as this are extremely vital for furthering our understanding of it. Photons are very well known physics objects, and additionally have no substructure. These facts combine to make the photon an extremely good probe to study pomeron and gain a greater understanding of it. Additionally, this is the first time a measurement such as this has been conducted at the LHC and therefore presents an extremely compelling motivation to conduct such a study.

5.2 Data Selection

As mentioned in the previous section, the data used for this analysis comes from the 2016 proton-lead (pPb) run at the LHC at $\sqrt{S_{NN}}$ = 8.16 TeV. These types of collisions are unique in the LHC, however, as they represent an asymmetric collision which amplifies the efforts of colliding in almost all respects. Rather than having similar particles being accelerated in similar ways, in pPb collisions they must be sent on very different paths on their way to the final collision.

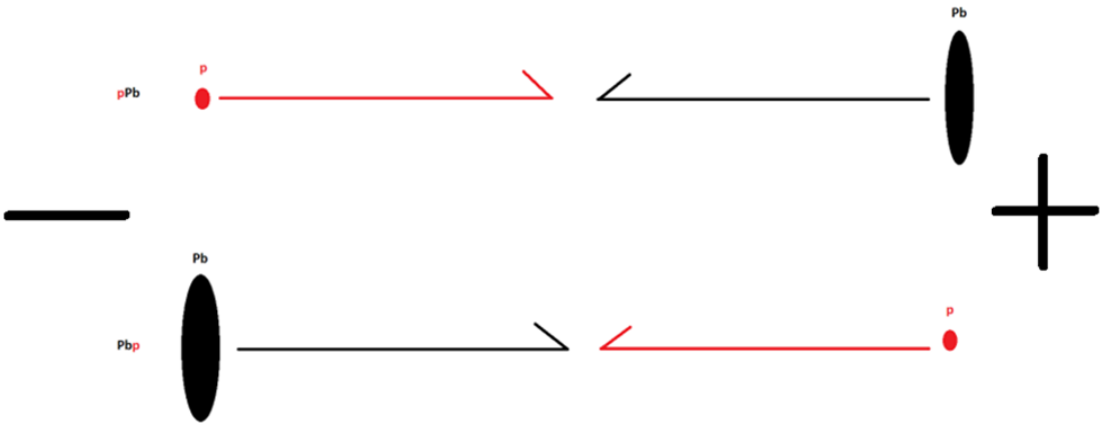

Figure 5.4: When dealing with an asymmetric system, it becomes very important to have a firm understanding of the actual geometries that are happening. pPb collisions occur when the proton is heading towards +Z (up the beampipe), and Pbp collisions occur when the proton is heading towards -Z (down the beampipe).

Another aspect that must be considered when talking of pPb collisions is that of

direction. In symmetric collisions, which are by far the most common at the LHC, one doesn't have to consider factors such as which direction each beam is coming from. However, in pPb collisions that is very much a real concern that needs to be factored in when doing an analysis. There are pPb collisions at the LHC, but there are also Pbp collisions. The difference between these two might not seem clear at first, but if one looks at Figure 5.4, one can see the difference between pPb and Pbp. When the term pPb is used, that refers to the proton moving in the positive Z direction (up the beampipe), while Pbp refers to the proton moving in the negative Z direction (down the beampipe). We are able to distinguish pPb vs Pbp through the use of a filter that separates the events into two datasets.

During the 2016 run, there was an integrated luminosity of 64.378 nb^{-1} of pPb data taken and 115.277 nb^{-1} of Pbp data taken. The mismatch between the datasets is mostly due to the fact that after running in pPb configuration, CMS was able to efficiently gather more data when the beam directions were switched. Because of the fact that CMS is a general purpose detector, and is therefore symmetrical, we can symmetrize one of the sets of data to match over with the other and therefore use the full combination of pPb and Pbp data. This process, while simple in theory, involves many moving parts and corrections that must be undertaken in order to minimize the effects of the detector. However, despite symmetrization, the two halves of the detector aren't exactly identical which leads to biases depending on direction. This introduces a systematic uncertainty that we will discuss in Section 6.2. For the analysis, the Pbp data was symmetrized to the pPb, but that is an arbitrary decision and the same results would be achieved if the reverse was done, as one can again see in Section 6.2. It should also be noted that all plots and figures produced for this dissertation were created through the use of the ROOT which is a high energy physics data analysis program.

As mentioned earlier, the LHC is producing more data than could ever reasonably be processed with our current technology. Therefore, triggers were implemented in order to allow an active filter to be in place when collisions were occurring. If the event that occurs satisfies one of these triggers, then the data is kept. Specialists design and cater these

triggers to catch physics events of a certain kind while minimizing the irrelevant events.

For this thesis, the trigger used is "HLT_PASingleEG5_HFTwoTowerVeto_SingleTrack_-v1". As mentioned in Section 3.2, triggers are vital simply due to the volume of information. Each collision has an extraordinary amount of data and, when combined with the collisions occurring once every 25 nanoseconds, this means it simply isn't feasible for our detector to collect each and every event. The solution is a trigger that is able to quickly and efficiently determine if the event that just occurred has a high chance of being "interesting," whereby we mean events that we are interested in studying Our trigger is the standard UPC dijet trigger and it has 3 elements. The first element is that a transverse energy of at least 5 GeV must be deposited in one tower of the electromagnetic calorimeter. Its second element is a veto on the number of towers over the noise threshold in either Hadronic Forward detector. If there are more than 2 towers above noise in both HFs, then the event is thrown out. The final element is that at least one track must be reconstructed in the pixel detector. Combining these elements together selects events which are prone to having rapidity gaps, which we mentioned above were one of the main ways of identifying UPCs. The main principle in action to select UPCs is asking for HFs to be mostly empty on at least one side. It should be noted, however, that the HFs were further restricted to be completely empty on both sides for this analysis as will be discussed below.

For a full description of how we will ensure that our sample is pure, refer to Figure 5.5. It will be useful to refer back to throughout the chapter as a reminder of the overall picture of this analysis.

Figure 5.5: A summary of the cuts that will be utilized in the next section in order to ensure we see the photoproduced dijets as desired. Each subsequent step reduces the background until the final stage when we have a highly pure sample.

5.3 Jet Properties

For this measurement, there are two main factors in the final state that we need to be concerned with. These factors are the rapidity gaps and the dijet system. This section, and the one following it, will focus upon one of these aspects in order to combine them in the final section for our main observable. Therefore, the goal of this section is to ensure the quality of our jets.

To begin with, we will start with the simplest aspect of ensuring jet quality. Aptly named, it is what is known as jet quality cuts. These properties were all assembled from a collection of jet experts whose goal was to ensure that any jets passing these criteria would constitute a "good" jet [52] [53]. The properties of this can be seen in the below table.

Jet Quality Cuts	
Jet Property	Quality Cut
Neutral Hadron Fraction	< 0.99
Neutral EM Fraction	< 0.90
Number of Constituents	> 1
Charged Hadron Fraction[1]	> 0
Charged Multiplicity[1]	> 0
Charged EM Fraction[1]	< 0.99
Neutral EM Fraction[2]	> 0.01
Neutral Hadron Fraction[2]	< 0.98
Number of Neutral Particles[2]	> 2
Neutral EM Fraction[3]	< 0.90
Number of Neutral Particles[3]	> 10

Table 5.1: A full list of the jet quality cuts that were made for this analysis. These values were all obtained from a jet study that was conducted by fellow members of CMS. [1] for $-2.4 \leq \eta \leq 2.4$ [2] for $2.7 \leq |\eta| \leq 3.0$ [3] for $|\eta| > 3.0$

All of these jet quality cuts have been performed from the very beginning, so any jets that are seen in this thesis can be assumed to pass these cuts and are therefore "good" jets. The difference between a "good" and a "bad" jet arises mostly from the fact that jets are not always composed of the same particles. As they arise due to random fluctuations of chance as a colorly charged object is emitted, each jet is unique. Within the full set of jets, there exist certain variations that are comprised of particles that we can detect to a much higher accuracy. This in turns allows our jet variables to be similarly defined at

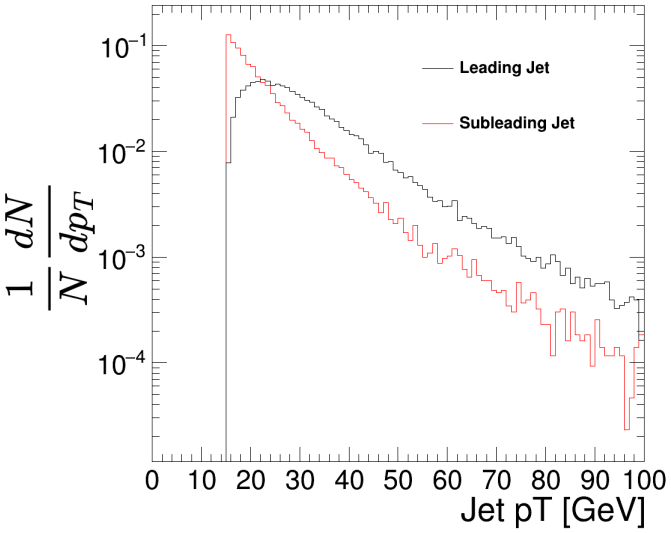

Figure 5.6: The leading and subleading jet p_T spectrum. As expected, the subleading jets tend to peak at lower p_T. For the purposes of our analysis, we require that both jets have p_T > 15 GeV/c. The y-axis can be thought of as a percentage of events in each bin. It should be noted that a cut was made on the p_T of the jets immediately after the trigger was applied. This trigger was rejecting events with leading jet p_T < 15 GeV. This was done with the knowledge that we'd apply higher cuts later on and was done purely for disk space.

a high accuracy. These cuts ensure that the jets we see are ideal for physics analyses by merit of them being extremely well defined. By that, we mean that the jets' various properties are known to high precision and won't have any sort of systematic biases due to machinery or other quirks that may arise. For photoproduced dijets, the average jet p_T is lower than a typical collision at the LHC, which is expected due to the nature of the source of the jets. Given that they arise from photon emissions, they tend to have a smaller p_T overall.

While the full spectrum of jets is interesting, a more useful measurement for this analysis is looking at the leading and subleading jets as in Figure 5.6. This refers to the jet with the highest p_T as the leading jet, with the jet with second highest p_T as the subleading. It should be noted that at the earliest stages of data gathering a cut was made on jet p_T. Any event with leading jet p_T < 15 GeV was thrown out as we knew that those events wouldn't be of interest and, most importantly, disk space was a commodity and this greatly cut down on that usage. In order to ensure that the jets weren't produced by some other process, we ask that both the leading and subleading jets have $p_T > 20 GeV/c$.

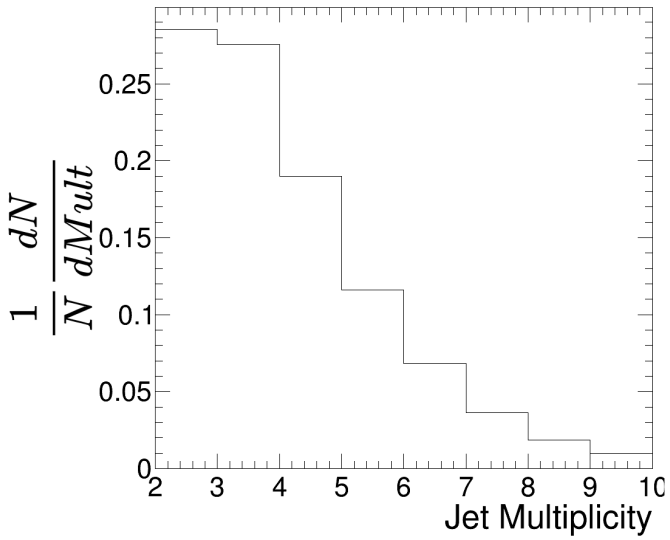

Figure 5.7: The distribution of number of jets present in any given event after the EG52Tow trigger.

When compared to the rest of CMS, these might seem like very low p_T jets, but in the realm of UPCs, these are fairly high p_T jets and exactly the kind that we'd expect to be produced from our specific process.

Now that the jets are of sound quality, we can begin performing additional cuts to ensure that we get the types of events that we wish to study. The next property we will look at is the number of jets. As mentioned above, for our measurement we wish to have a dijet system in the final state. Looking at Figure 5.7, we can see that while the most dominant number of jets in a given collision is 2, there remains a sizable amount of events with greater than 2 jets. As such, we do not make a cut on the number of jets at the moment. While it might seem counterintuitive since we are looking for a dijet system, but theory and reality often can appear quite different. What might initially start as a dijet system has the potential to morph (into a trijet, quadjet, etc.) via gluon radiation. Therefore, we reserve this as a potential cut until further into the analysis in order to prevent any biasing of our data.

The next jet cut we wish to make has to do with the geometries of the jets themselves. In a dijet event, you typically expect the resulting system of jets to be back to back due to conservation of momentum. This means that if we look at the difference in ϕ for the jets, we expect them to be around 180°, or π radians. In Figure 5.8, we can see that indeed the

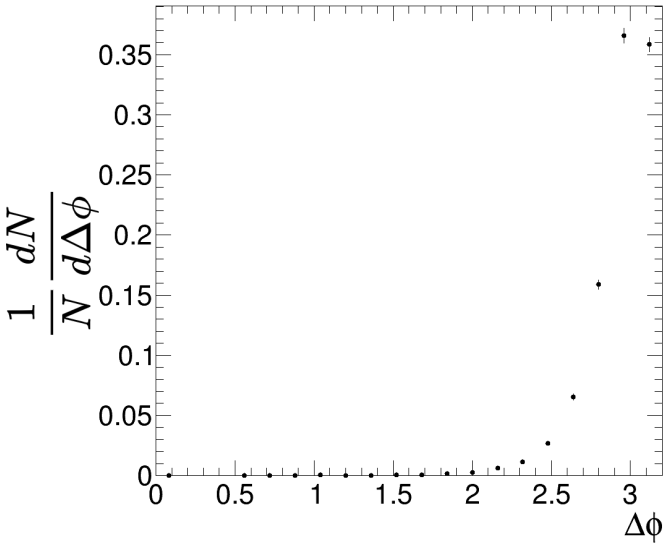

Figure 5.8: The difference in phi between the leading and subleading jets. Due to conservation of momentum, these jets tend to be back to back and have a angle of π between them. Therefore we make a cut on the data that $\Delta\phi > 2$

large majority of jet events do indeed fall around π as expected. Any deviations from π are indicative of some other activity within the detector such as another physics object other than a jet that we aren't looking for. In order to reduce any errant events, and following past analyses, we make a cut asking for $\Delta\phi > 2$. This allows for a slight amount of leeway with the back to back nature, while still reducing any strange physics occurrences or detector effects that might cause a $\Delta\phi$ smaller than 2.

Finally, while this isn't used in this analysis for cuts, we have a measurement of jet asymmetry which is an interesting measurement in its own right. In heavy ion collisions between lead ions, measuring the asymmetry between jet momenta in a dijet system can be used as a signal for jet quenching, with oftentimes very large asymmetries present. Jet asymmetry can be calculated in the following manner:

$$A_J = \frac{p_{T,1} - p_{T,2}}{p_{T,1} + p_{T,2}}, \tag{5.2}$$

where A_J is the asymmetry and $p_{T,i}$ is the ith jet's transverse momentum.

Interestingly, and somewhat expected, with collisions between protons and lead ions

we see a slight asymmetry in Figure 5.9. This asymmetry range falls almost exactly between the range of jet asymmetries from lead-lead collisions and proton-proton collisions, which typically don't have much asymmetry.

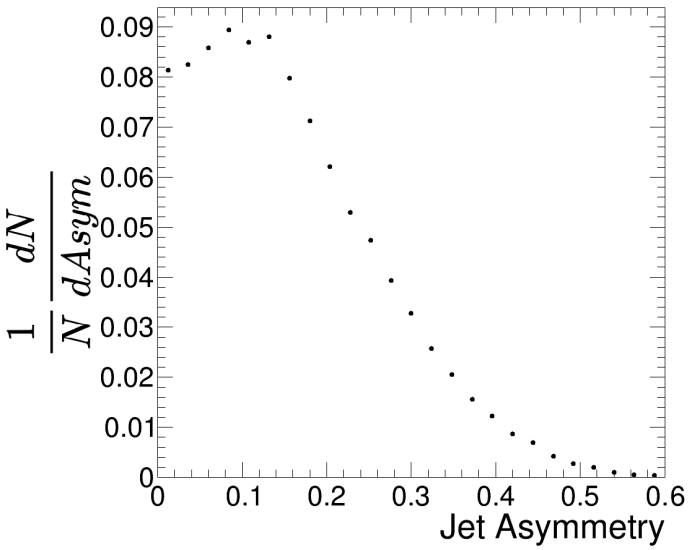

Figure 5.9: Measurement of the jet asymmetry in the dijet system. To see how jet asymmetry is calcualted refer to Equation 5.2. We can see a slight tending toward asymmetry, but not as much as is seen in collisions between lead ions.

5.4 Gap Selection

Now that we have covered cuts on the jet variables, the last thing we have to do in the final state is observe rapidity gaps. As a reminder, a rapidity gap is a region in space at a detector where there simply are no particles detected in a given division in rapidity. In this analysis, we employ 3 separate measures to attempt to ensure all events passing do actually have a rapidity gap. The first measure has already been covered and it is the loosest definition of the 3. This is the trigger that was previously discussed whose goal is to pare down the enormous amount of events coming in to get the events that are likely to be UPCs.

The second manner of determining gaps is the Hadronic Forward (HF) calorimeters. As mentioned in Section 2.4, these detectors are positioned on the very front of the CMS barrel. This positioning allows them to be the ideal spot for determinations of rapidity

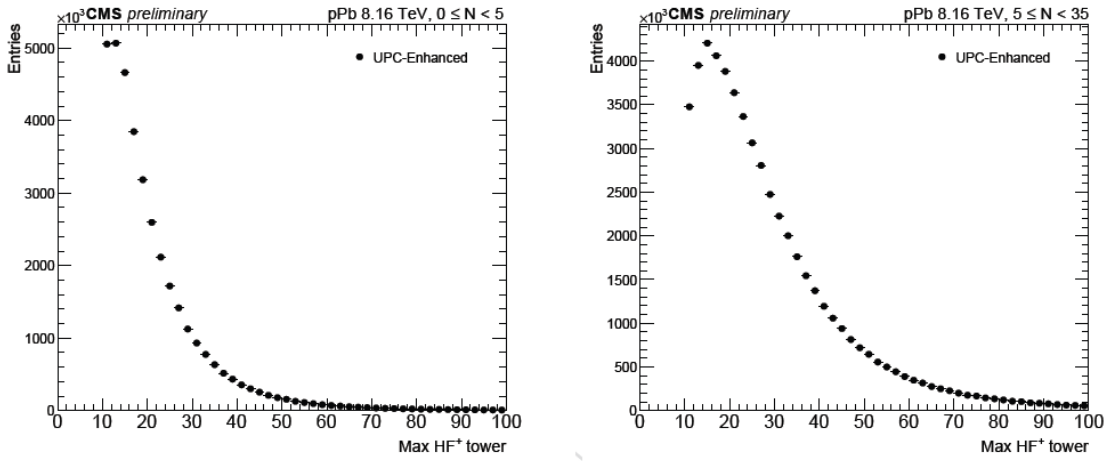

Figure 5.10: Here we have the HF+ tower distributions for the Minimum Bias pPb sample illustrating the highest tower energy in HF. From this distribution, it is possible to obtain the noise threshold for HF which separates actual physics events from random machine noise. The left hand graph corresponds to events with the number of offline tracks less than 5, while the right hand plot corresponds to events with between 5 and 35 tracks. This study was conducted using the same dataset as used in this analysis and so we will utilize their results as well.

gaps in the forward region. A rapidity gap, generally defined, is a region in phasespace within the detector where there is no activity. Activity meaning no particles are present and so it quite literally is a gap in space where nothing exists. As we don't have the ability to directly see particles flying through space like the aftermath of dropping a crate of bouncy balls, we are left with more indirect ways of defining a rapidity gap.

With the HF calorimeters, the methodology for determining gaps is through the use of towers. A tower is defined as a deposition of energy into a detector in a localized region. When a particle passes through different layers of a detector, the materials composing the detector produce a rapid light pulse. This light is then amplified, fed up into a readout box, and then summed up with other rapid light pulses within the vicinity of the first. The sum total of these light pulses are what make up a "tower," and the amount of light directly corresponds to the energy of the original particle passing through.

For this analysis, we wished to find events in which there were these very forward rapidity gaps, as that would be indicative of these diffractive photoproduced dijets. One of the largest concerns when considering this methodology is the presence of detector noise. If one were to look at the activity in any given detector in the absence of collisions

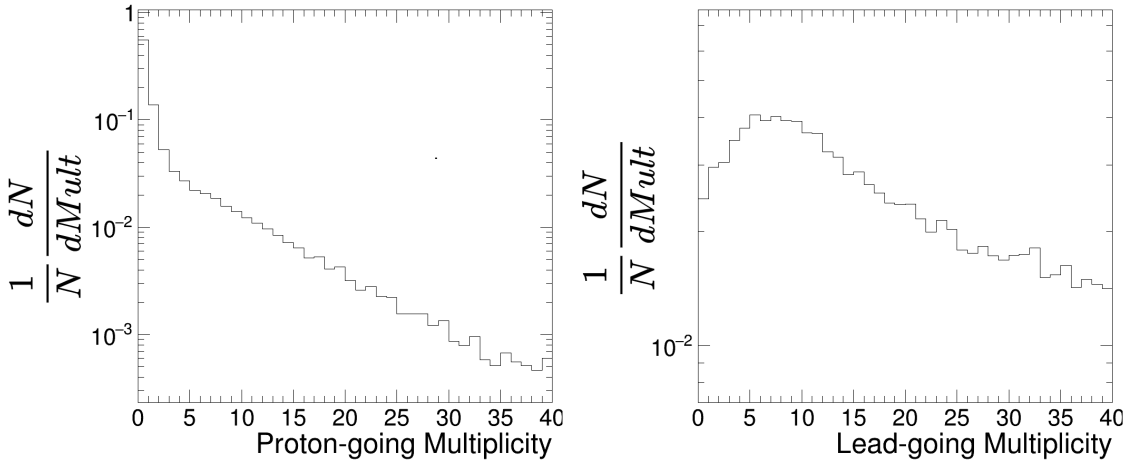

Figure 5.11: Multiplicities, or just raw number, of both the proton-going and lead-going Hadronic Forward detectors. For the purposes of these plots, we count the number of towers with energy > 10 GeV or 3 GeV for the proton-going HF and lead-going HF, respectively. These detectors are the primary manner in which the rapidity gap is defined in this analysis, with a cut being made on the number of towers to ensure that there is no activity in the forward regions.

happening, one would still be able to get "data" out of it which really corresponds to electronic noise. Therefore, in an analysis such as this one where the presence of a rapidity gap is vital, it becomes critically important to know the difference between detector noises and energy actually being deposited within the calorimeters.

We are able to rely upon past analyses which were able to calculate the noise threshold in either HF. These analyses were also conducted in pPb at 8.16 TeV and the summary of their HF noise threshold study can be seen in 5.10. The manner in which this was done was by examining the maximum tower energy seen in the proton-going HF in order to make a cut on where the towers being seen correspond to actual energy depositions. It was found that for the proton-going side, this corresponds to an energy of 10 GeV. So the number of towers in the proton-going HF side can be determined by looking at the number of towers with energy > 10 GeV. A similar study was conducted in the lead-going HF and the cut for that detector corresponds to energy > 3 GeV.

Now that the noise definitions have been established, it's possible to look at the distribution of towers in either HF in order to make our second cut on gaps in the data. A view of the distributions can be seen in Figure 5.11. Interestingly, the tower multiplicity in either side is very different from the opposite side. Multiplicity is another words for the

raw number count of towers we see in either HF. At first, this might seem strange and cause for alarm, but there are a variety of reasons to explain this discrepancy. First and foremost, we are dealing with an asymmetric collisions between protons and lead ions. This will inherently create a division between the distributions in either HF because of the simple fact that we have different particles which have different signatures. Lead ions, in general, are going to have many more particles being emitted from them purely by merit of the increased photon flux and the fact that a lead ion is 200 particles bound together. While this is the main source of the discrepancy, another more subtle reason is the fact that the noise thresholds for either side are drastically different. As lead ions are less energetic than their proton counterpoints, a lower energy threshold is going to be needed. An additional effect to this lowering is an overall increase to the number of towers that are passing this threshold. Therefore, it's entirely within reason, and quite frankly expected, for the lead-going HF to present with higher tower multiplicities on average.

The third, and final, method of determining gaps for this analysis is through the use of the Zero Degree Calorimeter (ZDC). While the ZDC is present on both sides of CMS, it is primarily utilized in heavy ion collisions. As such, for the purposes of this analysis it will only be used on the lead-going side as a crosscheck for the gap. A more comprehensive description of the ZDC can be seen in Section 2.4. Similarly to the HF, we will be utilizing the expertise of past analyses to determine the best manner in which to use the ZDC for gap determination [54].

While we were looking at towers in HF, the ZDC operates in a slightly different manner. It isn't segmented into individual towers, but rather totals up the energy deposited into the ZDC. Past analyses have examined this total energy deposition and have determined the thresholds for saying if the lead ion was intact or not. For our analysis, we wish the lead ion to be intact because its only role will be emitting a photon. This photon emission has a gap as a signature which we can utilize HF to identify, but by adding in the ZDC information on the lead-going side this means we are able to be doubly sure of gap definitions. Asking for HF to be empty is almost enough to purify our sample to an almost background-free state, but we have the ZDC and so utilize it as a failsafe.

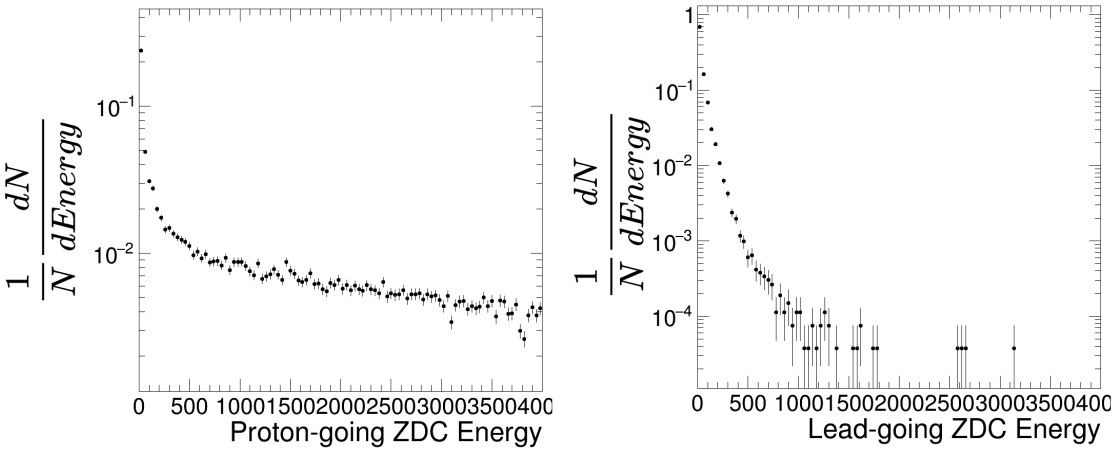

Figure 5.12: The Zero Degree Calorimeter is the other instrument in which we are able to look for UPC events. The energy deposited into the ZDCs can be indicative of number of neutrons that have been deposited which can then be used as a measure of if the lead ion is intact or not. For ZDCs, energy deposited that is below 1000 GeV is consistent with no neutrons being deposited, or that the lead ion is intact Working together withe HFs, this ensures that events we are seeing are in fact both photoproduced dijets. The proton-going ZDC is ill defined and therefore for this analysis it will not be used, but is shown here for completeness.

The total energy deposited into either ZDC can be seen in Figure 5.12. While both sides are listed, the primary utilization of the ZDCs will be purely for the lead-going side. The distribution here is quite interesting because as mentioned above, the cutoff energy for an intact lead ion is 1 TeV (or 1000 GeV). Almost all of the events gathered for this analysis satisfy this condition already. This is because of the fact that we have already made a critical selection in the form of the UPC dijet trigger as talked about in Section 5.2. By using data that has passed this UPC trigger, it is unsurprising then to see that the large majority of events that we can see are UPCs. This very comforting result once again reaffirms the purity of our sample and allows us to move forward with the knowledge that the hidden physics we hope to be observing is actually happening in the collision we're examining.

A potential cut that was touched upon in the jet section and is ready to be revisited is the number of jets in the collision as can be seen in Figure 5.13. In a perfect, nonrandom world, if we had an interaction which yielded 2 jets, they'd remain 2 jets. However, it appears there is a sizable contribution to the sample of 3 and even some 4 jet events. These types of events have several potential explanations and we will discuss them in

order of likelihood.

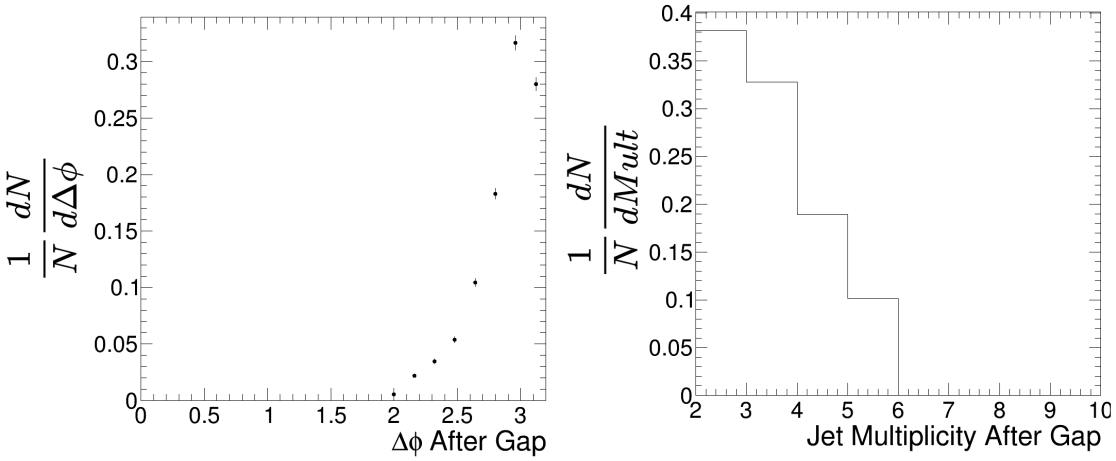

Figure 5.13: Distribution of jet multiplicity after gaps have been established as well as the $\Delta\phi$ between the leading jets. We can see that the multiplicity has decreased as well as the $\Delta\phi$ coming closer to fully back to back. This result is expected by merit of asking for gaps in the forward regions.

The first, and most likely event, is that the 3rd and 4th jets arise from quarks splitting in the early stages of after the collision during fragmentation. At that point in time, quarks have a propensity to split, and any split quarks will result in a new jet in the final state. The fact that we have fewer 4 jet events also lends credence to this theory as it would need to occur twice for us to get a 4 jet system. Another explanation is misidentification. As discussed previously, jets are identified via the anti-k_t algorithm and it's possible that a particularly messy event could lead to troubles with jet identification and cause a single jet to be mislabeled as 2 distinct jets. The final potential explanation is simply that these events are not truly the kind of events we are searching for. This is the least likely scenario as we have implemented several strict cuts to ensure we have a high purity, but it is possible for events to mimic each other so the possibility cannot be thrown out. In a perfect world with more integrated luminosity, we could throw out the 3 and 4 jet events to be entirely certain, but in our current reality, we will be choosing to keep these events in the sample as it seems unlikely that any sizable portion of events is due to misidentification.

A comprehensive summary of the different gap definitions can be seen below in Figure 5.14. In order to truly get the events we wish to study, we will be combining myriad differ-

ent aspects together. The particular properties of proton-lead collisions, when combined with specific detectors such as HF and ZDC, allow for an unambiguously pure sample to study. Therefore, with the pure sample in hand, we can begin our examination for the first time ever at the LHC of diffractive dijet photoproduced events in pPb.

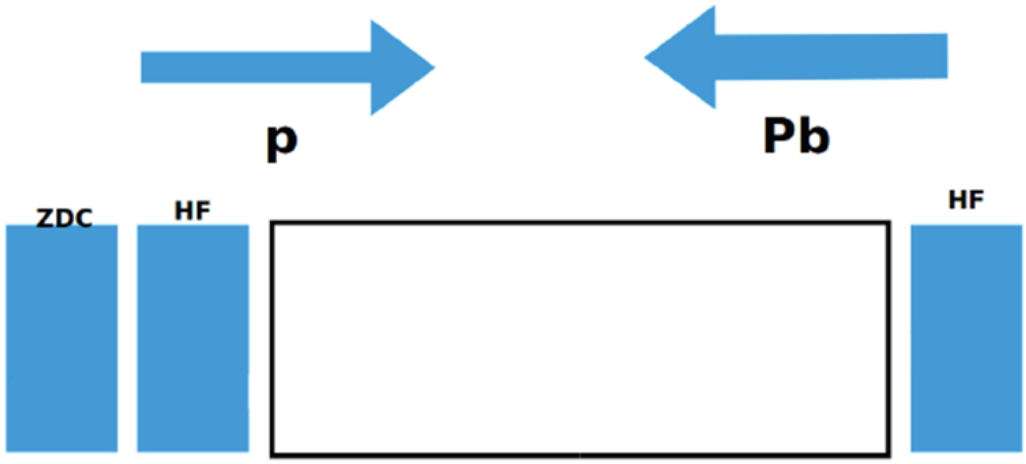

Figure 5.14: A summary of the gap selection criteria used on this analysis. For the proton-going side, we have only the HF detector to determine gaps, but on the lead-going side we have both HF as well as the ZDC to determine gaps. This cross check allows us to be doubly sure that any events with gaps truly do present that way. This is in addition to the initial trigger used for this data sample which already had a high likelihood of containing UPC dijet events to begin with.

5.5 Z_{IP} and x_γ

To summarize the work done thus far, we have ensured that we have UPCs by looking for events with rapidity gaps and also ensured that the dijet system in the final state is also consistent with photoproduced diffractive events. Additionally, we have carefully selected the dataset that is most suitable for looking for these kinds of events by exploiting properties of lead ions in these asymmetric collisions. Now, with all that in order, we can look at the main observable for this analysis. The two main observables, as shown in Section 3.3.2, that we will be looking at for the first time at the LHC are z_{IP} and x_γ:

$$x_\gamma = \frac{\sum_{i \in jets}(E_i - P_{z,i})}{\sum_{i \in X}(E_i - P_{z,i})} \tag{5.3}$$

and

$$z_{IP} = \frac{\sum_{i \in jets}(E_i + P_{z,i})}{\sum_{i \in X}(E_i + P_{z,i})}, \tag{5.4}$$

where z_{IP} is the momentum fraction of the parton relative to the pomeron and x_γ is the momentum fraction of the parton relative to the lead ion. The top sum in these variables runs over all the jets in the event, while the bottom sum is over all of the hadronic final state particles that were detected. E_i is the ith particle's or jet's energy and $P_{z,i}$ is the ith particle's or jet's momentum in the z-direction. This type of measurement has been conducted before at previous colliders, but never before has there been observations of diffractively photoproduced dijets at the LHC in pPb. The reason why we wish to look at these particular variables is that these variables can be used by theorists as descriptors of the quark and gluon content of the pomeron itself. These kinds of probes are invaluable for theorists wishing to refine their models of pomeron structure. As mentioned previously, this structure is a large unknown and so probes of this kind are instrumental in fleshing out our understanding by allowing direct comparisons to be made between empirical data and the models put forth by theorists.

Events such as these arise from the interactions between the pomeron and a photon. In this specific case, we can be extremely certain that the resultant dijet system is produced from the interactions between a photon from the lead ion and a pomeron from the proton. Therefore this measurement can allow us to use the extremely high energy photons which are emitted as a perfect probe into the pomeron itself.

The next step for this analysis would be unfolding these results in order to obtain the true distribution, however at this time this cannot be done. At the time of this writing, there exists an issue outside the author's control within the CMS software that prevents the needed Monte Carlo from being produced. Without the simulation of the detector effects, we cannot attempt to remove the detector effects from our measurement. Therefore, the goal for this analysis is the first observation and measurements of diffractively photoproduced dijets at the LHC.

With the first observation of these types of events at the LHC, future analyses in pPb will be able to build upon these foundations and work towards getting results directly comparable to theory and previous colliders. As mentioned in Section 3.3.2, there have been recent results published from HERA looking at the cross sections of photoproduced dijets. Taking this analysis to the next step by calculating the differential cross sections in these variables would be extremely useful for direct comparisons between the colliders.

Measurement such as this and potential future analyses building off of this one are instrumental for unlocking the secrets left in QCD and helping us finally understand exactly what this mysterious object is that is present in so many kinds of collisions. Pomeron mediated processes are present at every collider, but there remains the question of if all these different "pomerons" are the same physics object each time. It's entirely possible that the "pomeron" we see everywhere is actually a collection of similar, yet distinct, "pomerons." Despite its ubiquity, it still remains a mystery and therefore a fascinating object of study in the world of QCD. With measurements such as this one at our backs, we take one step closer to helping unravel the secrets of this strange mystery of QCD.

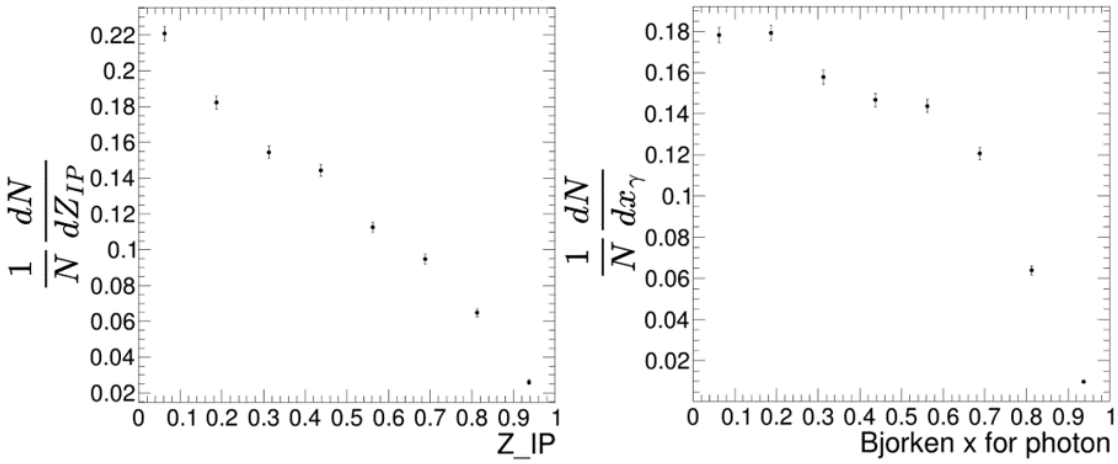

Figure 5.15: For the first time at the LHC, we have measurements of Z_{IP} and x_γ in photoproduced dijets in proton-lead collisions. Such events have been seen at HERA in the past and will be examined at some future electron-ion detector, but before now they haven't been looked at in the LHC. Z_{IP} is a characteristic that defines pomeron behavior. By examining Z_{IP} at different energies, theorists will be able to shed more light on the pomeron and hopefully learn exactly what it is.

Chapter 6: Systematic Uncertainties

Contents

This chapter will discuss in detail the calculation of systematic uncertainties in the main observables for this thesis, Z_{IP} and x_γ. The main methodology for calculating these uncertainties will be in varying each of the main cuts for the analysis and then measuring the effect this has on the final observable's value. Each section will focus on one of the main properties that was used as a selection cut to find the effect its uncertainty will have. To begin with, in Section 6.1 we shall discuss the error analysis methods used in the rest of this chapter. In Section 6.2, we will focus on an aspect that has heretofore been swept under the rug for ease of presentation. The data used in this thesis is both pPb and Pbp (see Section 5.1 for the difference) and in order to present a final measurement these two datasets had to be symmetricized. The effect of that shall be seen in this section. Next, in Section 6.3 we study the effect of jet uncertainty on the final measurement. Afterwards, in Section 6.4 we shall see the effect the gap definition from the Hadronic Forward detectors has. Similarly, in Section 6.5 we will examine how the Zero Degree Calorimeter's effect on gap influenced our observables. Finally, we end with a presentation of the total systematic findings in Section 6.6.

6.1 Systematic Background

This goal of this chapter is to outline the systematic checks in order to test the strength of our measurements presented at the end of Chapter 5, namely the measurements of Z_{IP} and x_γ. Their robustness will be tested by varying the cuts used in the selection of the events and determining the associated effect on the primary observables for this analysis. These measurements, alongside their associated uncertainties, will allow us to conduct a χ^2 test. We will be conducting a χ^2 test because of the fact that we have a sufficiently small dataset that the random fluctuations could easily be comparable to potential systematics. Therefore, we will classify whether the difference due to altering the cuts is statistically significant via the χ^2 method.

The effect of the variation of the cut on the final measurement of Z_{IP} and x_γ can be seen via calculation in the following manner:

$$x_{\gamma,systematic} = x_{\gamma,normal} - x_{\gamma,varied}, \tag{6.1}$$

where $x_{\gamma,normal}$ is the baseline value of x_γ that was measured in Chapter 5 and $x_{\gamma,varied}$ is the value of x_γ that is obtained by varying the different cuts used in this analysis. A similar measurement can be obtained for z_{IP} in the following way:

$$z_{IP,systematic} = z_{IP,normal} - z_{IP,varied}, \tag{6.2}$$

where $z_{IP,normal}$ is the baseline value of z_{IP} that was measured in Chapter 5 and $z_{IP,varied}$ is the value of z_{IP} that is obtained by varying the different cuts used in this analysis. In order to calculate χ^2 for each of systematic checks, we must also know the uncertainty for both $x_{\gamma,systematic}$ and $z_{IP,systematic}$. We are able to obtain these values from the known uncertainties of the variables used to calculate them. From $x_{\gamma,normal}$ and $x_{\gamma,varied}$ we can obtain $x_{\gamma,systematic}$, while from $z_{IP,normal}$ and $z_{IP,varied}$ we can obtain $z_{IP,systematic}$. The manner

in which we are able to calculate $x_{\gamma,systematic}$ or $z_{IP,systematic}$ depends on the relationship between the original dataset and the dataset that is obtained from varying the cuts. In the event that the change to the parameters results in a sample of data that is completely independent of the original dataset, then the uncertainty can be calculated by

$$\sigma_{systematic} = \sqrt{|\sigma^2_{normal} + \sigma^2_{varied}|}, \tag{6.3}$$

where σ_{normal} is the uncertainty of the original dataset and σ_{varied} is the uncertainty of the varied, and in this case independent, dataset. The other situation that can arise is if the dataset produced via the slight variation is completely contained within the original dataset. In such a case, the uncertainty can be calculated by

$$\sigma_{systematic} = \sqrt{|\sigma^2_{normal} - \sigma^2_{varied}|}, \tag{6.4}$$

where the variables have the same definitions as before.

Once we have the values for the systematic deviation and the uncertainty for that value, we can then look to measure the significance of this deviation via a χ^2 test. In order to statistically determine the significance of the effect of varying the cut, if χ^2 is greater than 8, we call the deviation as statistically significant. χ^2 can be calculated in following way:

$$\chi^2 = \sum_{i=1}^{8} \frac{(z_{IP,systematic,i})^2}{\sigma_i^2}, \tag{6.5}$$

where $z_{IP,systematic,i}$ is the ith bin of Z_{IP} and σ_i^2 is the associated uncertainty of that bin. The sum ranges from 1 to 8 because we have 8 bins in which the events are grouped. As stated above, if the χ^2 value is less than 8, we state that the results are statistically consistent. If they are statistically consistent, we can say the systematic uncertainty due

to that variable would be negligible. In the case, however, that χ^2 is greater than 8, we can determine that this is due to some systematic uncertainty. The magnitude of the systematic uncertainty can be calculated via the solution to the following equation:

$$\chi^2 = 8 = \sum_{i=1}^{8} \frac{(z_{IP,systematic,i})^2}{\sigma_i^2 + \sigma_{Syst}^2}, \tag{6.6}$$

where σ_{Syst} is the systematic uncertainty. In these scenarios, we can then solve for σ_{Syst} in order to determine the magnitude of this systematic uncertainty. Once all the associated systematic uncertainties are compiled, they can then be combined in the following way:

$$\sigma_{TotalSystematic} = \sqrt{\sigma_{Syst1}^2 + \sigma_{Syst2}^2 + \sigma_{Syst3}^2 + ...} \tag{6.7}$$

The remainder of this chapter will comprise of looking at the effects of the individual cuts used in this analysis. In each section we will calculate the variables discussed above to see the effect it has on our measurement.

6.2 Comparing pPb vs Pbp

The first instance we will examine isn't a variable upon which we cut, but rather a look into the specifics of the hardware itself. While being referred to as pPb collisions, the large majority of the run was actually done in a Pbp configuration. For a refresher on the difference, one can either refer to Figure 5.4 or just note that pPb references to the situation when the proton is going in the positive z direction. During the analysis, this difference was eliminated via symmetrizing the datasets into one complete whole. However, there remains the question of whether these two dataset are actually valid to be symmetrized. While it may easy to just brush under the rug, there remains the fact that with any machinery, let alone something so complex as CMS, there will be performance differences between pieces that were designed exactly the same. Therefore, the goal for this section is to explore the level of symmetry that exists and whether it is valid to combine

the two datasets. For all plots in this chapter, we will be plotting the original dataset, the changed dataset, and then below these the difference between the two datasets.

The manner upon which this will be determined will be through the use of a χ^2 test comparing the two. In Figure 6.1, we can see the results of plotting our two main observables with the dataset split into pPb and Pbp elements as well as the difference present for each bin. When comparing pPb vs Pbp, we have two independent dataset and therefore uncertainty will be combined in the manner outlined in Equation 6.3 With this check, a χ^2 of 321.4 and 322.2 was found for Z_{IP} and x_γ, respectively. This indicates that there is some sort of systematic uncertainty that needs to be included in order to account for this difference. Following the method prescribed in Equation 6.6, it was found that there is a systematic error of 0.0123 and 0.0125 for Z_{IP} and x_γ, respectively. We can attribute this systematic uncertainty to the the asymmetry between forwards and backwards configurations of collisions during the 2016 pPb run.

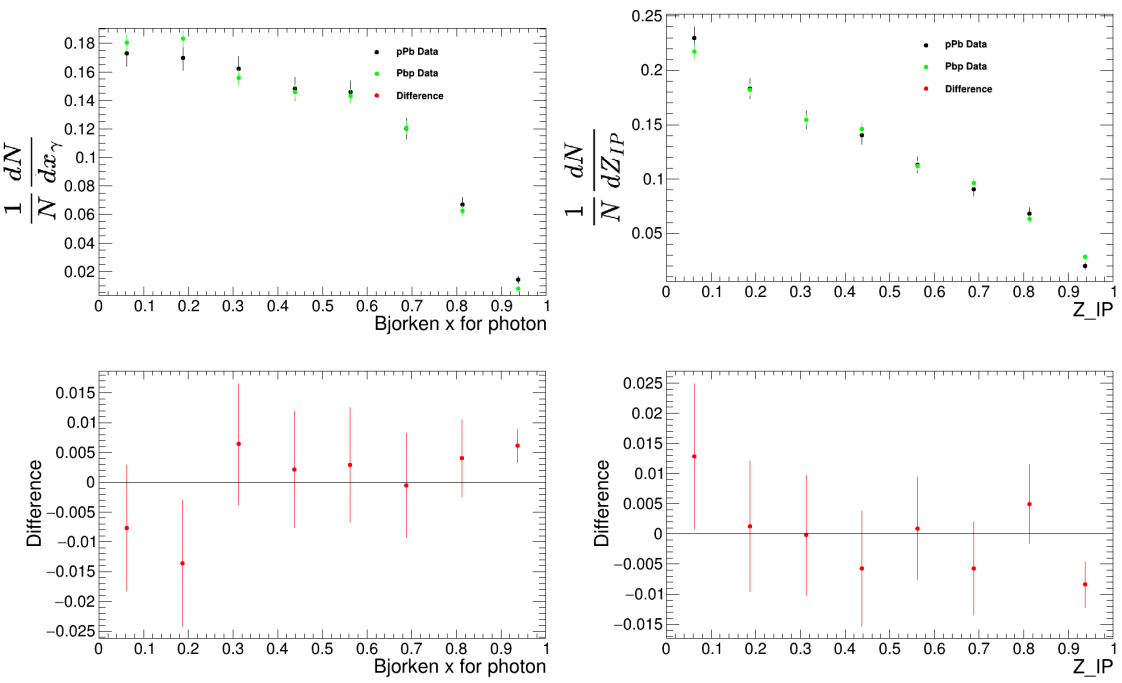

Figure 6.1: The results of comparing pPb and Pbp datasets. In this case, the two datasets were not statistically consistent and therefore we can say there is some effect due to collision direction.

6.3 Varying Jet Properties

The next cross check will be in the central dijet system for our analysis. There were various cuts undertaken in order to purify our sample and ensure we get the types of events we want, but the primary cuts we will be examining are the cuts on the $\Delta\phi$ variable as well as the pT of the dijet system. To begin with, we will examine the role of asking for back to back jets in our system. The primary cut for this was asking for $|\Delta\phi| > 2.0$, but in order to test the strength we will instead ask for $|\Delta\phi| > 2.5$ to see what effect that has on the final result. The χ^2 value for this test was 1.3 and 1.44 was found for Z_{IP} and x_γ, respectively, which indicates a successful crosscheck of the dataset. This result isn't too surprising when one looks at Figure 5.8. Its distribution is already extremely predisposed to give us back to back events and so the difference between 2.0 and 2.5 in $\Delta\phi$ doesn't produce dramatic differences.

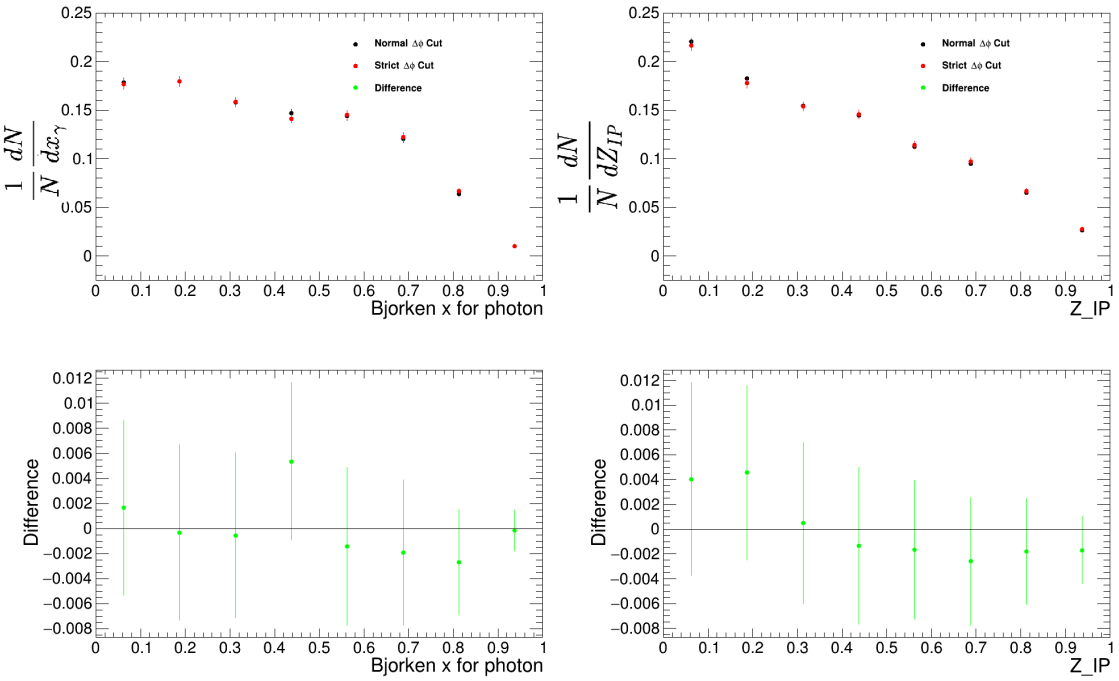

Figure 6.2: The results of changing the $\Delta\phi$ cut. In this case, the two datasets were statistically consistent and therefore we can count this as a successful crosscheck and contributing negligible uncertainty.

The other most important variable to consider when looking at the dijet system in the final state is the pT of these jets. Transverse momentum is an important variable

for many reasons in QCD and can be used as a marker for the regime of QCD in which one event falls. Therefore, the requirement for pT can be a very important one, and any adjustments to it have the potential to push you from one physics regime into the other. For our purposes, we will can identify the effect of a more strict pT requirement by increasing the thresholds by 2.5 GeV. This more strict pT requirement allows us to be confident that we are in the physics regime in which we wish to study. However, it seems that there may be some systematic uncertainty as the χ^2 value for this test was 91.8 and 88.1 was found for Z_{IP} and x_γ, respectively. Following the method prescribed in Equation 6.6, it was found that there is a systematic error of 0.0143 and 0.0128 for Z_{IP} and x_γ, respectively.

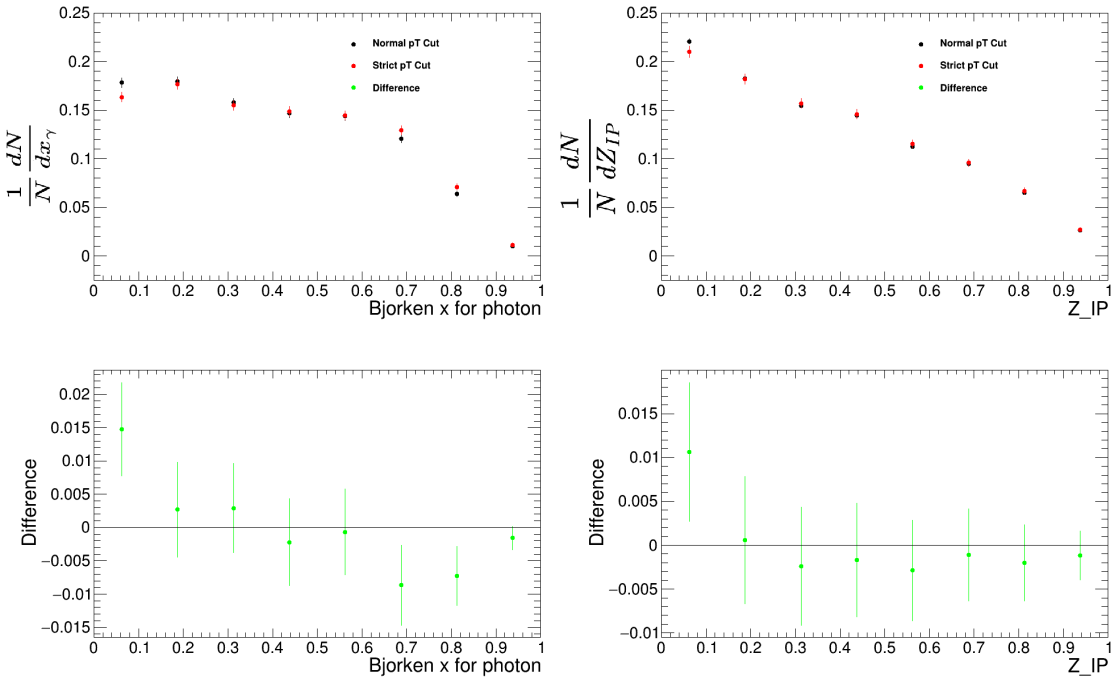

Figure 6.3: The results of changing the dijet system pT cut. In this case, the two datasets were not statistically consistent and therefore this contributes some additional systematic uncertainty.

6.4 Varying Gap Definitions in HF

The gap definitions for this analysis are twofold, and we will be checking the influence of each one independently in order to see the effect they have. To begin with, we will look at the gaps as defined through the use of the HF detectors, which are located in the

very forward region as a reminder. Gap definition for this case was done via counting the number of towers that surpassed the noise threshold. In the actual analysis, we asked for events with 0 towers in order to ensure the rapidity gap was present. For a systematic check, we will loosen this definition to allow the number of towers in either HF to be < 5 in order to see the effect it has on the primary observables. When loosening the HF gap definition, we have two datasets that are not independent and therefore uncertainty will be combined in the manner outlined in Equation 6.4. While it might be expected that the loosening of this important gap definition would yield significantly different results, our methodology ensures that the difference between strict and loose isn't as significant as one might think of a first glance. The χ^2 value for this test was 7.06 and 6.06 was found for Z_{IP} and x_γ, respectively, which indicates a successful crosscheck of the dataset.

It's worth discussing, however, the reasons why this might be the case. The events we are looking for are ones in which there should be no activity in the forward region which is the definition of a gap. So, by allowing events in which there is distinctly forward activity, one might expect serious deviations from the pure sample, but instead we are observing consistency. The manner in which we can reconcile this fact comes from the fact that we have several methods of determining rapidity gaps and when we loosen one, the other can metaphorically pick up the slack. In more precise terms, many of the events in which there are up to 5 towers in the HF may have been events in which > 1 TeV of energy was deposited into the ZDC on the Pb-going side. This results in those events being rejected, and therefore we end up with a difference from the measured that is statistically consistent with the pure sample.

6.5 Varying Gap Definitions in ZDC

The other gap definition used throughout this analysis was through the use of the ZDC. Its primary method of determining gap was the sum total of energy deposited into the ZDC. While the analysis used a measure of < 1 TeV to be consistent with the lead ion staying intact, for this systemic check we will as for a much more strict measurement of < 500 GeV to be consistent with our UPCs. When tightening the ZDC gap definition, we

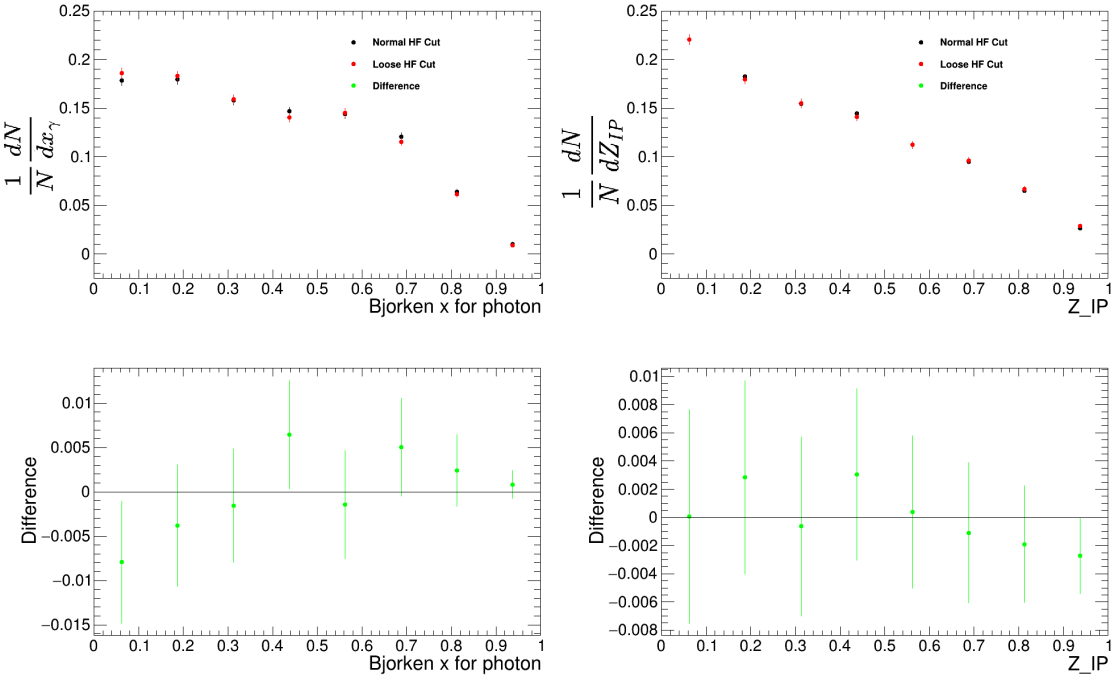

Figure 6.4: The results of changing the HF tower cut. In this case, the two datasets were statistically consistent and therefore we can count this as a successful crosscheck and contributing negligible uncertainty.

have two datasets that are not independent and therefore uncertainty will be combined in the manner outlined in Equation 6.4. Similarly to the previous case in HF, the ZDC systematic check gave a χ^2 value of 0.00795 and 0.01213 was found for Z_{IP} and x_γ, respectively, which indicates a successful crosscheck of the dataset This again indicates the importance of having a double cross check for UPC events in the analysis as it lends a robustness to the measurement. Any sort of deviation in the gap definition in one instance will likely be "caught" by the independent check which lends confidence as to the strength and purity of our sample.

6.6 Systematic Uncertainty Results

The results of the systematic studies on this analysis can be seen below in Table 6.1. In the end, the total systematic uncertainties for Z_{IP} and x_γ are respectively 0.01886 and 0.01789. Their main sources of uncertainty were primarily due to uncertainties in the dijet pair's transverse momentum as well as the difference between forward and backwards events in this asymmetric collision.

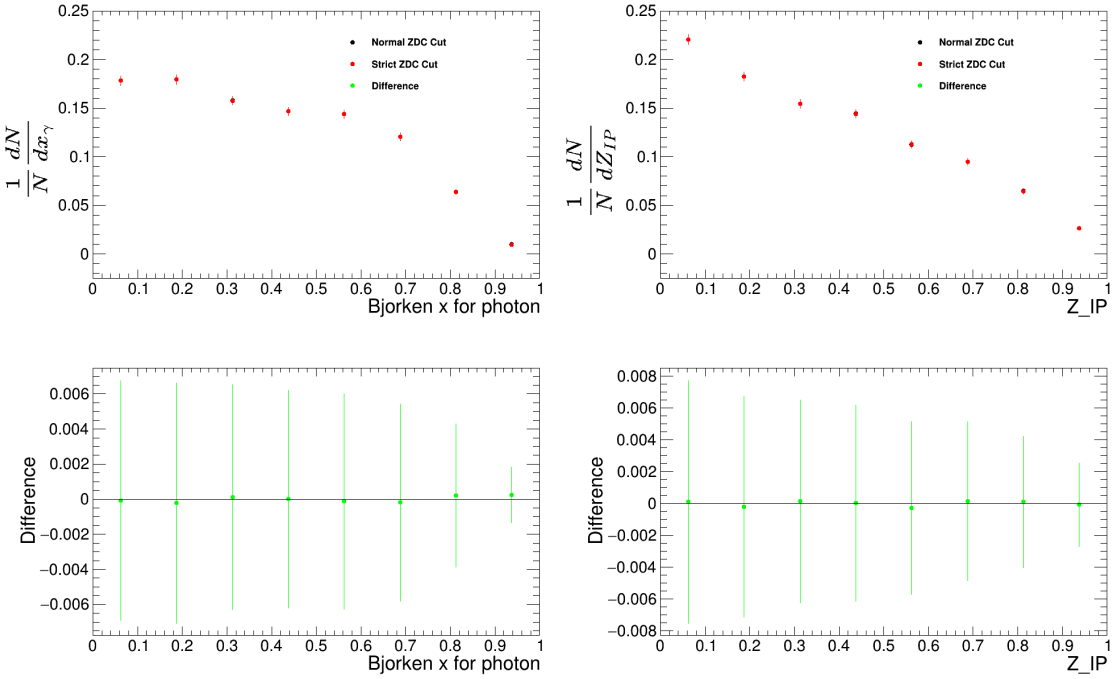

Figure 6.5: The results of changing the ZDC energy cut. In this case, the two datasets were statistically consistent and therefore we can count this as a successful crosscheck and contributing negligible uncertainty.

The fact that one of our dominating uncertainties is due to the differences in particle collisions direction bears discussion. For our analysis, it was worth the added systematic uncertainty by combining datasets because we received a smaller overall uncertainty, but it could easily be the case in certain analyses that using the full combined dataset would actually negatively impact your results. This would obviously vary based on measurement and statistics, but it's an interesting case that should be noted by any analyses following this one that are dealing with the same dataset. While typically adding more data is always a good thing, it could very easily be the case that one hurts their results by doing so and caution is advised for anyone reading this and conducting a study on the 2016 pPb dataset. It would be extremely beneficial to conduct a similar study with your observable before delving too deep in order to determine if combination is the right call.

Systematic Uncertainties				
Cut	χ^2 Z_{IP}	χ^2 x_γ	$\sigma_{Syst,z}$	$\sigma_{Syst,x}$
pPb vs Pbp	321.4	322.2	0.0123	0.0125
Jet pT	91.8	88.1	0.0143	0.0128
$\Delta\phi$	1.3	1.44	-	-
HF Cut	7.06	6.06	-	-
ZDC Cut	.00795	.01213	-	-
Total Uncertainty			0.01886	.01789

Table 6.1: Here we have the full summary of the systematic studies conducted for the observables Z_{IP} and x_γ. These represent a modest increase to the overall uncertainty in our variables. However, due to the fact that no measurement had been made at the LHC previously, our measurement represents a massive increase in the data available about the pomeron.

Chapter 7: Results and Conclusions

This dissertation presents the first observation of photoproduced diffractive dijets in ultra-peripheral proton-lead collisions at $\sqrt{S_{NN}}$ = 8.16 TeV at the Large Hadron Collider. The full summary of the events can be seen in Figure 7.1 where we include the systematic uncertainties that were found in the previous chapter. These types of events have not been observed before at the LHC and thus represent a major leap forward for the study of photoproduction. In the past, studies have been conducted at other colliders at lower energies and these studies have presented many questions about the pomeron. Over all the orders of magnitude of energy, we talk about the pomeron and its role in these collisions, but at the moment we don't even know if the pomeron we see at HERA is the same at the LHC. Questions such as these need to be answered for us to truly have an understanding of QCD going forward. In the future, an electron-ion collider will be constructed and photoproduction will be a dominant force in the types of interactions that occur there and so it would be extremely irresponsible to not get as much information as possible before continuing on to a new collider. Therefore, this measurement represents a much needed filling of the gaps in our understanding of QCD as a whole. The hope being that some future student will be able to utilize the work done throughout this dissertation in order to achieve results that can be directly compared to previous colliders and help us understand what exactly this pomeron is and if it is indeed even the same object between experiments.

This first observation of these types of events at the LHC represents the first step in utilizing the highest energies available to us in order to gain a better understanding of the pomeron. This was accomplished due to the asymmetric collisions we studied because we were able to exploit properties of the interacting particles. Lead ions have a high likelihood to emit photons due to the extreme electric fields coming from the highly charged nucleus which results in an enhancement in that photon flux equal to Z^2 (where Z = 82 for Pb). By having such a large enhancement when compared to a proton, this means that whenever

we observe a rapidity gap on the lead-going side, we can be certain it is due to photon emission and not any other processes that might have that rapidity gap as a signature. Similarly, protons are much more likely to have rapidity gaps due to pomeron exchange rather than photon emission. The combination of these two properties in an asymmetric collision allows us the rather unique benefit of being certain of the initial states of our collision.

Therefore, this allows us to present the first observation of photoproduced diffractive dijets in ultra-peripheral proton-lead collisions at $\sqrt{S_{NN}}$ = 8.16 TeV at the Large Hadron Collider as can be seen in Figure 7.1. These results include the systematic uncertainties found in the previous chapter and represent an excellent foundation for future studies to explore the relationship between the pomeron seen in previous colliders and pomeron exchange as we see it at the LHC. Additionally, this measurement with the extreme energies available to us at the LHC act as excellent tools for theorist to hone their models and incorporate the results found in order to have the best possible models going forward with the future electron-ion collider where events such as these will be plentiful [55].

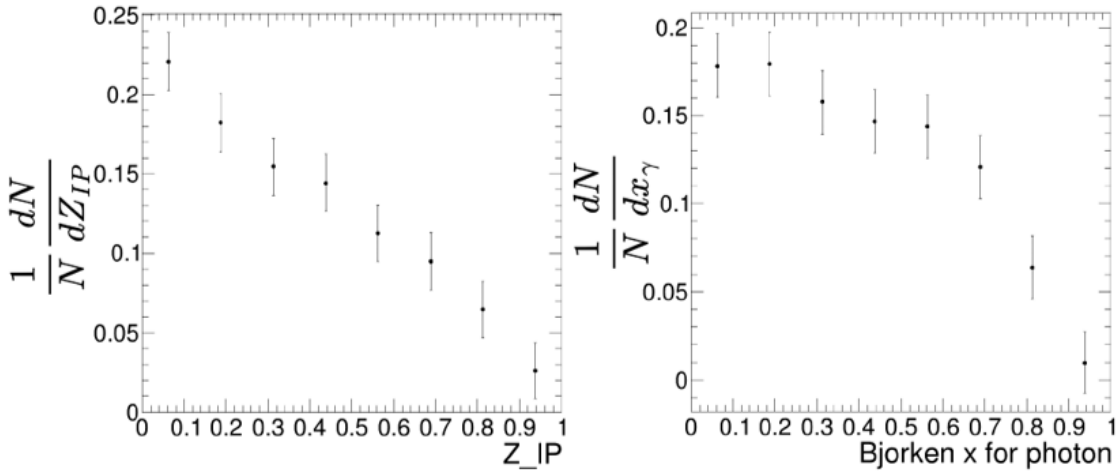

Figure 7.1: For the first time at the LHC, we have measurements of Z_{IP} and x_γ in photoproduced dijets in proton-lead collisions. Such events have been seen at HERA in the past and will be examined at some future electron-ion detector, but before now they haven't been looked at in the LHC. This plot includes the systematic uncertainties outlined in the previous chapter as well.

While our measurement does represent a large step forward into demystifying the pomeron, as a measurement of this kind had not been conducted at the LHC, there is

still places to go and ways to improve our results. As mentioned before, we did not have the ability to have direct theory comparisons due to CMS software running into errors with our MC generator. Despite this, we can attempt to characterize our results in the context of previous measurements at lower energies. When compared to what is seen in Section 3.3.2, we are able to see a somewhat consistent trend of z_{IP} when compared to past colliders. By this, we mean we see a similar dependence with z_{IP}, but any further comparisons or conclusions based on our results must be disentangled from detector effects and calculated differentially in order to minimize biases we have from our measurements being conducted at different machines. We take the optimistic stance that this sort of general consistency seems to indicate that perhaps further refinement of this data will yield a result that shows consistent behavior between these experiments. Such a result would indicate that the pomeron behavior that we saw at lower center of mass energies is also consistent with what we saw in this experiment. If this happened, then it's possible that our measurements would allow theorists to make claims on if the pomeron we see at lower energies remains constant throughout the higher energy ranges. It is the hopes of this author that the ability to produce MC for this analysis will happen in the near future. With that knowledge in hand, we could begin the process to characterize the behavior of the pomeron over a wide range of energies. A study such as this would allow us to begin to break apart the mystery of the pomeron. Answering the question finally of if all pomerons are the same, or even just the simple question that I find myself asking repeatedly, "what the heck is a pomeron?"

Bibliography

[1] H. Georgi and S. L. Glashow, "Unity of All Elementary Particle Forces," *Phys. Rev. Lett.*, vol. 32, pp. 438–441, 1974 doi:10.1103/PhysRevLett.32.438

[2] L. Olson, "Nuts and bolts."

[3] E. Rutherford, "The scattering of alpha and beta particles by matter and the structure of the atom," *Philosophical Magazine*, 1911.

[4] J. Beringer *et al.* (Particle Data Group Collaboration), "Review of Particle Physics (RPP)," *Phys. Rev. D*, vol. 86, p. 010001, 2012 doi:10.1103/PhysRevD.86.010001

[5] M. Spira, A. Djouadi, D. Graudenz, and P. M. Zerwas, "Higgs boson production at the LHC," *Nucl. Phys. B*, vol. 453, pp. 17–82, 1995 doi:10.1016/0550-3213(95)00379-7

[6] K. G. Wilson, "Confinement of Quarks," *Phys. Rev. D*, vol. 10, pp. 2445–2459, 1974 doi:10.1103/PhysRevD.10.2445

[7] S. Weinberg, "A Model of Leptons," *Phys. Rev. Lett.*, vol. 19, pp. 1264–1266, 1967 doi:10.1103/PhysRevLett.19.1264

[8] M. Peskin and D. Schroeder, "An introduction to quantum field theory," *Westview Press*, 1995.

[9] P. Skands, "Introduction to QCD," pp. 341–420. 80 p, Jul 2012 doi:10.1142/9789814525220$_0$008 Comments: Lecture notes from a course given at TASI 2012. Last update: January 2015. 79 pages, including a hyperlinked index at the back. [Available Online]: https://cds.cern.ch/record/1461470

[10] M. Gell-Mann and F. E. Low, "Quantum electrodynamics at small distances," *Phys. Rev.*, vol. 95, pp. 1300–1312, 1954 doi:10.1103/PhysRev.95.1300

[11] H. D. Politzer, "Asymptotic Freedom: An Approach to Strong Interactions," *Phys. Rept.*, vol. 14, pp. 129–180, 1974 doi:10.1016/0370-1573(74)90014-3

[12] R. D. Ball *et al.*, "Parton distributions with LHC data," *Nucl. Phys. B*, vol. 867, pp. 244–289, 2013 doi:10.1016/j.nuclphysb.2012.10.003

[13] G. Altarelli and G. Parisi, "Asymptotic Freedom in Parton Language," *Nucl. Phys. B*, vol. 126, pp. 298–318, 1977 doi:10.1016/0550-3213(77)90384-4

[14] E. Witten, "Strong coupling expansion of Calabi-Yau compactification," *Nucl. Phys. B*, vol. 471, pp. 135–158, 1996 doi:10.1016/0550-3213(96)00190-3

[15] V. Mathieu, J. Nys, C. Fernández-Ramírez, A. Hiller Blin, A. Jackura, A. Pilloni, A. Szczepaniak, and G. Fox, "Structure of pion photoproduction amplitudes," 06 2018.

[16] Q.-D. Zhou, Y. Itow, H. Menjo, and T. Sako, "Monte carlo study of particle production in diffractive proton–proton collisions at

$$\sqrt{s} = 13$$

s = 13 tev with the very forward detector combined with central information," *The European Physical Journal C*, vol. 77, no. 4, Apr 2017 doi:10.1140/epjc/s10052-017-4788-7. [Available Online]: http://dx.doi.org/10.1140/epjc/s10052-017-4788-7

[17] O. S. Brüning, P. Collier, P. Lebrun, S. Myers, R. Ostojic, J. Poole, and P. Proudlock, *LHC Design Report*, ser. CERN Yellow Reports: Monographs. Geneva: CERN, 2004 doi:10.5170/CERN-2004-003-V-1. [Available Online]: https://cds.cern.ch/record/782076

[18] "LHC Guide," Mar 2017. [Available Online]: https://cds.cern.ch/record/2255762

[19] E. Mobs, "The CERN accelerator complex - 2019. Complexe des accélérateurs du CERN - 2019," Jul 2019, general Photo. [Available Online]: https://cds.cern.ch/record/2684277

[20] M. Campanelli, *Inside Cern's Large Hadron Collider: From The Proton To The Higgs Boson*. World Scientific Publishing, 2015.

[21] G. Aad *et al.* (ATLAS Collaboration), "The ATLAS Experiment at the CERN Large Hadron Collider," *JINST*, vol. 3, p. S08003, 2008 doi:10.1088/1748-0221/3/08/S08003

[22] K. Aamodt *et al.* (ALICE Collaboration), "The ALICE experiment at the CERN LHC," *JINST*, vol. 3, p. S08002, 2008 doi:10.1088/1748-0221/3/08/S08002

[23] A. A. Alves, Jr. *et al.* (LHCb Collaboration), "The LHCb Detector at the LHC," *JINST*, vol. 3, p. S08005, 2008 doi:10.1088/1748-0221/3/08/S08005

[24] S. Chatrchyan *et al.* (CMS Collaboration), "The CMS Experiment at the CERN LHC," *JINST*, vol. 3, p. S08004, 2008 doi:10.1088/1748-0221/3/08/S08004

[25] T. Sakuma (CMS Collaboration), "Cutaway diagrams of CMS detector," May 2019. [Available Online]: http://cds.cern.ch/record/2665537

[26] S. Chatrchyan *et al.* (CMS Collaboration), "Precise mapping of the magnetic field in the cms barrel yoke using cosmic rays," *Journal of Instrumentation*, vol. 5, no. 03, p. T03021–T03021, Mar 2010 doi:10.1088/1748-0221/5/03/t03021. [Available Online]: http://dx.doi.org/10.1088/1748-0221/5/03/T03021

[27] S. Chatrchyan and others (CMS Collaboration), "Alignment of the cms tracker with lhc and cosmic ray data," *Journal of Instrumentation*, vol. 9, no. 06, p. P06009–P06009, Jun 2014 doi:10.1088/1748-0221/9/06/p06009. [Available Online]: http://dx.doi.org/10.1088/1748-0221/9/06/P06009

[28] S. Chatrchyan *et al.* (CMS Collaboration), "Performance and Operation of the CMS Electromagnetic Calorimeter," *JINST*, vol. 5, p. T03010, 2010 doi:10.1088/1748-0221/5/03/T03010

[29] *The CMS hadron calorimeter project: Technical Design Report*, ser. Technical design report. CMS. Geneva: CERN, 1997. [Available Online]: https://cds.cern.ch/record/357153

[30] V. Khachatryan *et al.* (CMS Collaboration), "The very forward CASTOR calorimeter of the CMS experiment," *JINST*, vol. 16, no. 02, p. P02010, 2021 doi:10.1088/1748-0221/16/02/P02010

[31] O. A. Grachov, M. J. Murray, A. S. Ayan, P. Debbins, E. Norbeck, Y. Onel, and D. G. d'Enterria (CMS Collaboration), "Status of zero degree calorimeter for CMS experiment," *AIP Conf. Proc.*, vol. 867, no. 1, pp. 258–265, 2006 doi:10.1063/1.2396962

[32] R. K. Ellis, W. J. Stirling, and B. R. Webber, *QCD and collider physics*. Cambridge University Press, 2 2011, vol. 8. ISBN 978-0-511-82328-2, 978-0-521-54589-1

[33] I. I. Balitsky and L. N. Lipatov, "The Pomeranchuk Singularity in Quantum Chromodynamics," *Sov. J. Nucl. Phys.*, vol. 28, pp. 822–829, 1978.

[34] B. Andersson, G. Gustafson, G. Ingelman, and T. Sjostrand, "Parton Fragmentation and String Dynamics," *Phys. Rept.*, vol. 97, pp. 31–145, 1983 doi:10.1016/0370-1573(83)90080-7

[35] R. J. Fries, B. Muller, C. Nonaka, and S. A. Bass, "Hadronization in heavy ion collisions: Recombination and fragmentation of partons," *Phys. Rev. Lett.*, vol. 90, p. 202303, 2003 doi:10.1103/PhysRevLett.90.202303

[36] V. Khachatryan *et al.* (CMS Collaboration), "The CMS trigger system," *JINST*, vol. 12, no. 01, p. P01020, 2017 doi:10.1088/1748-0221/12/01/P01020

[37] S. Chatrchyan *et al.* (CMS Collaboration), "CMS, the Compact Muon Solenoid. Muon technical design report," 12 1997.

[38] F. Beaudette (CMS Collaboration), "The CMS Particle Flow Algorithm," in *International Conference on Calorimetry for the High Energy Frontier*, pp. 295–304, 2013.

[39] M. Cacciari, G. P. Salam, and G. Soyez, "The anti-k_t jet clustering algorithm," *JHEP*, vol. 04, p. 063, 2008 doi:10.1088/1126-6708/2008/04/063

[40] C. A. Bertulani, S. R. Klein, and J. Nystrand, "Physics of ultra-peripheral nuclear collisions," *Ann. Rev. Nucl. Part. Sci.*, vol. 55, pp. 271–310, 2005 doi:10.1146/annurev.nucl.55.090704.151526

[41] A. J. Baltz, "The Physics of Ultraperipheral Collisions at the LHC," *Phys. Rept.*, vol. 458, pp. 1–171, 2008 doi:10.1016/j.physrep.2007.12.001

[42] J. G. Contreras and J. D. Tapia Takaki, "Ultra-peripheral heavy-ion collisions at the LHC," *Int. J. Mod. Phys. A*, vol. 30, p. 1542012, 2015 doi:10.1142/S0217751X15420129

[43] V. Andreev *et al.* (H1 Collaboration), "Diffractive Dijet Production with a Leading Proton in *ep* Collisions at HERA," *JHEP*, vol. 05, p. 056, 2015 doi:10.1007/JHEP05(2015)056

[44] H. Abramowicz *et al.* (H1, ZEUS Collaboration), "Combination of measurements of inclusive deep inelastic $e^{\pm}p$ scattering cross sections and QCD analysis of HERA data," *Eur. Phys. J. C*, vol. 75, no. 12, p. 580, 2015 doi:10.1140/epjc/s10052-015-3710-4

[45] B. R. Webber, "A QCD Model for Jet Fragmentation Including Soft Gluon Interference," *Nucl. Phys. B*, vol. 238, pp. 492–528, 1984 doi:10.1016/0550-3213(84)90333-X

[46] S. Abdullin, P. Azzi, F. Beaudette, P. Janot, and A. Perrotta (CMS Collaboration), "The fast simulation of the CMS detector at LHC," *J. Phys. Conf. Ser.*, vol. 331, p. 032049, 2011 doi:10.1088/1742-6596/331/3/032049

[47] S. Agostinelli *et al.* (GEANT4 Collaboration), "GEANT4–a simulation toolkit," *Nucl. Instrum. Meth. A*, vol. 506, pp. 250–303, 2003 doi:10.1016/S0168-9002(03)01368-8

[48] M. Albrow, A. De Roeck, V. Khoze, J. Lamsa, E. Norbeck, Y. Onel, R. Orava, and M. G. Ryskin (CMS Collaboration), "Forward Physics with Rapidity Gaps at the LHC," *JINST*, vol. 4, p. P10001, 2009 doi:10.1088/1748-0221/4/10/P10001

[49] F. D. Aaron, C. Alexa, V. Andreev, S. Backovic, A. Baghdasaryan, E. Barrelet, W. Bartel, K. Begzsuren, A. Belousov, and et al., "Diffractive dijet photoproduction

in ep collisions at hera," *The European Physical Journal C*, vol. 70, no. 1-2, p. 15–37, Oct 2010 doi:10.1140/epjc/s10052-010-1448-6. [Available Online]: http://dx.doi.org/10.1140/epjc/s10052-010-1448-6

[50] G. Ingelman and P. E. Schlein, "Jet Structure in High Mass Diffractive Scattering," *Phys. Lett. B*, vol. 152, pp. 256–260, 1985 doi:10.1016/0370-2693(85)91181-5

[51] V. Guzey and M. Klasen, "Diffractive dijet photoproduction in ultraperipheral collisions at the lhc in next-to-leading order qcd," *Journal of High Energy Physics*, vol. 2016, 04 2016 doi:10.1007/JHEP04(2016)158

[52] V. Khachatryan *et al.* (CMS Collaboration), "Jet energy scale and resolution in the CMS experiment in pp collisions at 8 TeV," *JINST*, vol. 12, no. 02, p. P02014, 2017 doi:10.1088/1748-0221/12/02/P02014

[53] A. M. Sirunyan *et al.* (CMS Collaboration), "Calibration of the CMS hadron calorimeters using proton-proton collision data at $\sqrt{s}$ = 13 TeV," *JINST*, vol. 15, no. 05, p. P05002, 2020 doi:10.1088/1748-0221/15/05/P05002

[54] O. Surányi, A. Al-Bataineh, J. Bowen, S. Cooper, M. Csanád, V. Hagopian, D. Ingram, C. Ferraioli, T. Grassi, R. Kellogg, and et al., "Performance of the cms zero degree calorimeters in ppb collisions at the lhc," *Journal of Instrumentation*, vol. 16, no. 05, p. P05008, May 2021 doi:10.1088/1748-0221/16/05/p05008. [Available Online]: http://dx.doi.org/10.1088/1748-0221/16/05/P05008

[55] A. Accardi *et al.*, "Electron Ion Collider: The Next QCD Frontier: Understanding the glue that binds us all," *Eur. Phys. J. A*, vol. 52, no. 9, p. 268, 2016 doi:10.1140/epja/i2016-16268-9